UNIVERSITA' DEGLI STUDI DI MILANO
BICOCCA

Spectroscopy of Advanced Semiconducting Nanostructures with the establishment of Single Particle characterization.

Doctoral Dissertation of:
Andrea Pianetti

Department: Materials Science
PhD Course: Materials Science and Nanotechnology
Registration number: 860296
Tutor: Prof. Sergio Brovelli
Academic year: 2021/2022
Cycle: XXXV
Coordinator: Prof. Marco Bernasconi

Abstract

This thesis focuses on experimental work in the field of fundamental spectroscopy of advanced luminescent nanocrystals for optoelectronic applications, in the wider context of new materials for energy. First, I will describe the development of a powerful tool for the advanced analysis of such nanoparticles, namely Single Particle Spectroscopy (SPS). This technique has the potential to analyze optical properties at the single nanocrystal level to better understand the influence of the multitude of nano-differences that are lost in ensemble spectroscopy measurements; in fact, this information becomes increasingly relevant as synthetic strategies become more sophisticated and state-of-the-art. In addition, it is possible to study the antibunching process in a potential single-emitter source, a key element in the development of quantum technologies. This type of measurement has never been performed in our laboratory, so I started from scratch to design and put together the whole system. The experimental implementation of this set-up is quite complex for several reasons including the extremely low light intensity level, the criticality of the alignment below the diffraction limit and the time resolution requirements for correlation measurements. The first chapter will be devoted to the study of an effective design and optimization of an SPS set-up, going through the trials and errors that led to the final geometry. We were able to measure the optical properties of core-shell colloidal nanoplatels at the single-particle level, obtaining peculiar results and demonstrating the effectiveness of the constructed set-up. Parallel to the construction of this set-up, my research work focused on the fundamental study of some nanostructures with novel designs to be measured prospectively with the SPS system. These new materials have been described in Chapter 2 and Chapter 3; in particular, Chapter 2 focuses on the cutting-edge progress of the already well-known lead halide perovskite nanocrystals, starting from the fabrication of extremely confined crystals to observe quantum confinement effects to the formation of heterostructures for tuning and enhancement of optical properties. Such heterostructures can also be used to produce thermodynamically inaccessible phases by exploiting direct epitaxial interaction between lattices. Finally, in Chapter 3, a new class of nanomaterials will be discussed, whose peculiarity is that they are free of Pb atoms and thus have low toxicity and environmental impact, but excellent optical properties as downshifters.

Keywords: Luminescent Nanoparticles, Single Particle Spetroscopy, Advanced Perovskites Nanocrystals, Pb-free emitters

Contents

1 | Single Particle Spectroscopy: set-up design, realization and first applications

1.1. State of Art and Introduction

The last decades of research on nanoscience has proved what Feynmann foresaw in his famous lecture "there's plenty room in the bottom". Experimental methods on fabrication and manipulation of nanostructures have been developed to such an advanced level that nowadays new techniques are needed to be able to study those nanostructures individually in order to be able to evaluate more and more effectively the nanometric structural differences which affect the physical properties.

One of the most outstanding discoveries in the nanoscale world are luminescent nanoparticles [1]; ther optical properties is in fact strongly affected by their dimension due to the fact the electron and hole's wavefunction is not fully delocalized as in bulk system but instead is confined within a box whose dimension is comparable to its wavelength; the dimension of the nanoparticle becomes the key factor in determining the energy levels of the system because of the role played by spatial confinement energy on the Hamiltonian of the system; the result is that quantum confinement effects have unveiled a completely new photo-physics compared to bulk crystals emitters known so far, where the relationship structure-property is crucial in the nanometric and sub-nanometric scale.

The only experimental investigation tools which have the required nanometric resolution are Atomic Force Microscopy and Electron Microscopy, but they almost completely lack on the possibility of measuring the optical properties; on the other hands, Conventional ensemble Spettroscopy is able to study the optical properties of nanoparticles, but for this technique samples are generally either solutions, continuous films or powders which are exited with an optical source (for example, a laser spot) that probes an area in which a very high number of particles are located.

Luminescent nanoparticles are mainly produced by wet chemistry methods, which consist in growth in solution from seeds that are thermally activated to generate a kinetically favoured growth; as a result, even in the same batch, nanoparticles can have differences in terms of size, shape, surface morphology, ligands attachment, defectuality and so on and all of those parameters can affect directly the optical properties; all those small differences between each individual nanocrystal (NC) cannot be evaluated in ensemble spectroscopy as the optical signal recorded will be the sum of a huge number of nanocristals, and the single's contribution will be lost among the ensemble as it will be averaged out statistically in the gigantic number of particles excited. The result is that it is not possible to understand the real contribution of these key parameters when they are all averaged out in a standard spectroscopic measurement. In order to decouple the heterogeneity of the products of reaction and evaluate how each parameter effects the optical properties directly, the most effective method is Single Particle Spectroscopy (SPS) [2].

This techniques is focused on overcoming limitations of ensemble spectroscopy by being able to directly optically excite one single luminescent nanoparticle and measure only its fluorescence; this allows to correlate directly the effect of those parameters (size, shape etc) to the optical properties; in order to realize this experimentally, some essential conditions are required:

- To adequately isolate a single fluorescent particles from other particles; this is generally achieved by drying a highly dilute solution on a solid substrate
- To design an optical system that is able to create the smallest possible excitation spot, i.e the exited area has to be pushed to the lowest possible limit.
- To spatially move with sufficient sensitivity the excitation spot to find the single particle's position along the substrate and finely focus upon it;

When those conditions are met, it is possible to measure single particle fluorescence and analyze the optical response being sure that it is ascribable only to that specific nanocrystal. In the experimental section of this chapter, I will go in details on how this can be realized and the scientific challenge behind it.

The importance and power of SPS as an analytic tool will become more and more useful with the increasing level of accuracy required in synthetic strategies in the nanoscience field; the more sophisticated and complex those systems are expected to become, the more important this technique will become in fundamental and applied material science; the next-generation SPS systems hold the great potential to guide the explorative researches in the field of nanoparticle design.

Moreover, some optical phenomenon are only visible at single particle level, but they strongly affect the macroscopic properties of the system. The most important example of such phenomenon is blinking, which can strongly affect the total Photoluminescence Quantum Yield (PLQY) of the nanocrystal (this phenomenon will be discussed in detail in the theoretical background section).

Another very useful application of a SPS set up is to measure and characterize single photon emitters. This topic became extremely important in the last decade due to the exponential growth of the field of quantum comunication and quantum computing. Quantum mechanics offers original and powerful schemes for processing information, which could never be achieved in classical devices. In the broad field of quantum computing, teleportation and networking, the storage of quantum information in the states of individual photons would present a lot of advantages: single photons emitted from an ideally perfect single photon source are indistinguishable propagating particles which can carry information at the speed of light, the have a very low interaction with the environment for long distances, resulting in communication with low noise, low loss and low distortion [3, 4]. Moreover, it is possible to store an impressive quantity of information in the form of quantum-bits by exploiting they're tunable quantum properties such as momentum, energy, polarization etc. The number of information encodable in a photon's quantum state is enormously bigger than what is achievable with modern computer's bit based memory; furthermore, quantum bits as the base for computational tasks would allow to perform . Finally, in the field of cryptography, using single photons would allow to immediately discover if an information has been ears-dropped due to the collapse of their wavefunction [5].

The need for the ideal single photon emitter has become one of the main challenges for the development of quantum technology; even though a lot of different systems have been studied in the last 20 years, each of them presents their individual challenges and limitations and a material which can satisfy all of the technologies requirements is yet to be found. The best performances so far have been achieved with III-V semiconductors, but their fabrication in complex and hardly scalable while requiring cryogenic temperatures to work [6, 7]. On the other hand, colloiodal nanocrystals are emerging in this field as they can operate well also at room temperature and can be electrically driven; these advantages come with the well known strong points of this class of material such as low cost fabrication, solution processability and easy scaling-up processes. Moreover they match some of the most important optical requirements for a quantum emitter, such as high PLQY, fast radiative lifetimes and narrow emission peaks [8]. Yet there is still need for a systematic work on most materials mainly due to their poor optical stability when isolated, which prevent a lot of experimental work on understanding in depth their properties as quantum emitters. Moreover, only a short quantity of colloidal luminescent nanocrystal has actually been investigated; lately, due to a lot of experimental work on sample preparation and stability [9], colloidally synthetized perovskites, have been fondly studied and started to show great potential as single photon emitters [10]

We considered to build a single particle set up also to be able to characterize the optical purity of both well known good photon emitters and most importantly to be able to study a plethora of new materials that open new routes in quantum material science.

In this chapter i will outline first the theoretical background the design strategies and realization of a SPS set up stating from scratch and how we obtained

1.2. Fundamentals of Single Particle Spectroscopy

1.2.1. Theoretical Background

In the field of SPS it is very important to have a powerful tool to discriminate between measuring a single particle emission or a multiple particle emission, because their size (few nanometers) is far below diffraction limit so the spatial discrimination is not achievable: a 5 nm luminescent single NP or a cluster as big as 1 μm with decades of aggregated nanoparticles will both be seen with a optical microscope as a round luminescent spot 1 μ big, with no significant and appreciable differences. Luckily, to solve this issue, we have second Order Correlation Function $g^{(2)}$.

Second order Correlation Function

Second Order Correlation function $g^{(2)}$ of an optical field with a temporal dependent intensity I(t) is mathematically defined as

$$g^{(2)}(\tau) = \frac{\langle I(t)I(t+\tau)\rangle}{\langle I(t)\rangle^2} \tag{1.1}$$

where t is time and τ is a given delay. In an optical experiment, I(t) and I(t + τ) are simply the number of photons detected at a certain time t and a certain time t + τ. The physical meaning of $g^{(2)}$ (whose independent variable is the delay τ not absolute time t) can be interpreted as follows: when a detector measures a certain number n of photons, what is the possibility of detecting the same number of photons during a certain interval of time t + τ? In such expression, what really matters is not the absolute time of arrival of photons but the time lag τ between the two events. When photons arrive, the time lag between the detection of the second group of same number of photons gives us powerful information on the way those photons are emitted. In particular, the $g^{(2)}$ function at 0 lag ($g^{(2)}(\tau)$, with $\tau = 0$) is the crucial information to speculate about coincidence of events. It tells us how often we detect two photons at times very close to each other (we imagine here to always detect one or zero photons at a time).

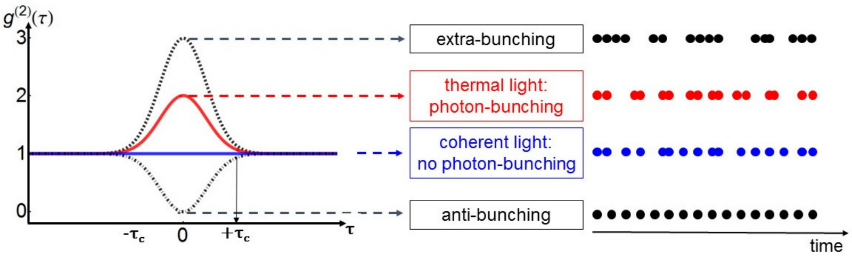

Figure 1.1: Second Order Correlation Function and its physical meaning in optics: Extra Bunching, Bunching and Antibunching

If photons always travel together in packets with a random distribution, the possibility of detecting other photons at 0 delay from the previous one not only is extremely high, but the highest. This is the case of Thermal Light, which is called bunched light (the name refers to the fact that photons are emitted and travel in packets, also called bunches). The reason behind it is the photon statistics of thermal light, which follows a Bose-Einstein distribution. When the first photon is detected, a higher number of photon are going to be detected shortly after, so that the number of photon events right after the first one can be statistically even higher than the first number. Thermal light, which is full of intensity oscillations due to the nature of the light emission itself, falls perfectly into this case. In terms of $g^{(2)}$ this means

$$g^{(2)}(\tau) > 1 \qquad for\ bunched\ light \tag{1.2}$$

In the case of perfectly coherent light, such as lasers, by definition light is emitted with constant intensity i.e when a certain number of photons is detected at a time t, almost the same number of photons can be detected for any arbitrary delays including at $\tau = 0$. It follows that:

$$g^{(2)}(0) = 1 \qquad for\ coherent\ light \tag{1.3}$$

In the case of quantum light, a photon is generated by the recombination of electron and a hole occupying their respective energy level, following the quantum mechanics rules. When this happens, a photon of a given energy is emitted. In this case, the possibility of detecting another photon at zero delay is 0, because of the origin of the emission: another photon cannot be emitted until that electron-hole pair is formed again and it is impossible to generate it until another excitation process occurs. So in general $g^{(2)}(0) < 1$.

$$g^{(2)}(0) < 1 \qquad for\ antibunched\ light \tag{1.4}$$

Anti-bunching is a direct consequence of quantum theory of light and is a condition for all sources of light that can be explained with quantum theory. It is in fact due to the sub-Poissonian nature of the emitted light (see figure 1.2 right panel).

In the case where those conditions are met:

- The excitation source is a pulsed laser.
- Each pulse can generate not more than one exciton.
- Pulses are enough temporally spaced so that the excited state has the time to fully relax back into ground before the next pulse arrives.

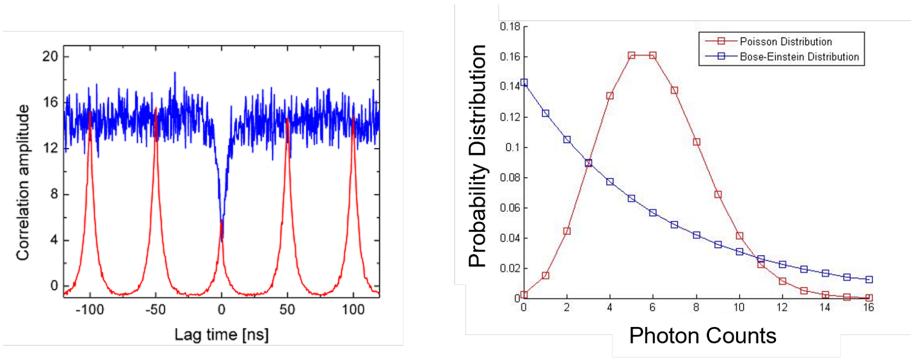

Figure 1.2: Left: Antibunching measured with a pulsed (red curve) or continuum source (blue curve, Right: Typical Poisson Distribution of Quantum light vs Bose-Einstein distribution typical of Thermal light)

It is impossible to generate more than one photon per pulse, and consequently the possibility to have two photons events with zero lag is impossible ($g^{(2)}(0) = 0$)

If we reverse this argumentation, we can use a measurement of $g^{(2)}$ as a discrimination tool for single photon emitters. If we are able to measure the second order correlation function measure $g^{(2)}$ and at zero lag $g^{(2)}(0) = 0$ we are in the presence of a single photon emitter.

$$g^{(2)}(0) = 0 \qquad for\ single\ photon\ emitters \tag{1.5}$$

Experiments probing for photon antibunching are generally performed in a Hanbury Brown-Twiss interferometer set-up, in which the emitted light is split with a 50/50 beam-splitter onto two single photon sensitive detectors. The detector outputs are then connected to a TCSPC (Time-Correlated Single Photon Counting) unit and the time difference between the two signals originating from two emitted photons is repeatedly measured and histogrammed with picosecond resolution.

Antibunching experiments can essentially be performed with pulsed or continuous-wave excitation (figure 1.2, left panel). With continuous-wave excitation, antibunching is manifested with a flat line with a notable "intensity dip" at zero time difference τ whose steepness is correlated with the lifetime. With pulsed excitation, the result shows the individual laser pulses spaced by the pulse period with a reduced or missing pulse at the correlation time difference of zero..

An even more correct way to measure antibunching is to write on a binary file, for each detected photon, its absolute arrival time and on which detector it has been recorded; then use a dedicated correlation algorithm to reconstruct the correlation function.

Blinking

Another distinct spectroscopic fingerprint of single photon emitters, specially colloidal nanocrystals, is Blinking.

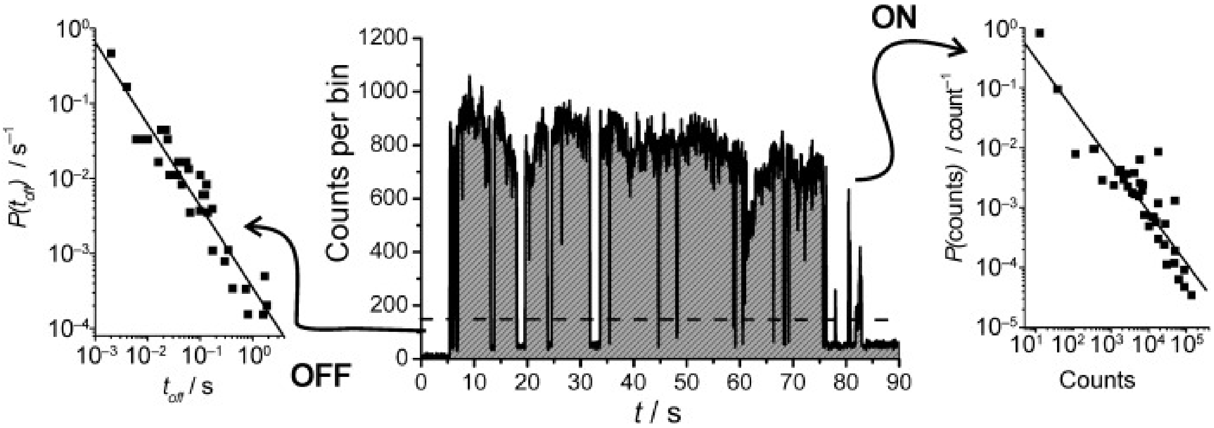

Figure 1.3: A typical Blinking trace recorded for a single particle. The latral graph report the P_{on} and P_{off} distribution

Blinking is a phenomenon for which the intensity of luminescence is not constant over time but it fluctuates. This intermittency has been observed for dyes, molecules, nanostructures and so on but only when those objects were observed below the micrometer range, close to or at single particle regime. The abrupt change of the emission intensity from an ON state to an OFF state has been first attributed to the charging of nanocrystal by the presence of an extra charge; in this picture, non-radiative pathways such as Auger recombination have a high probability to take place, leading to the quenching of the radiative pathways and consequently PL detection.

Many models have been studied in order to explain such complex mechanism, but all of them converge in ascribing the off state with a form of ionization of the particle; a lot of experimental effort has been put into understanding the ON/OFF statistics to find a mathematical model that could explain such behaviour. Assuming a charging/discharging model, the theoretical probability distribution of ON and OFF periods would have had to follow an exponential behaviour with given constrains due to charging and discharging rate; however, experiments showed that the data follow an inverse power-law; that means that the distribution of ON OFF events is not reproducible but can randomly vary during every PL experiment. The OFF coefficient α_{OFF} is generally around 1.5, is insensitive to common experimental parameters such as environment, incident power, temperature etc. and mostly, follows over 5 orders of magnifude the trend.

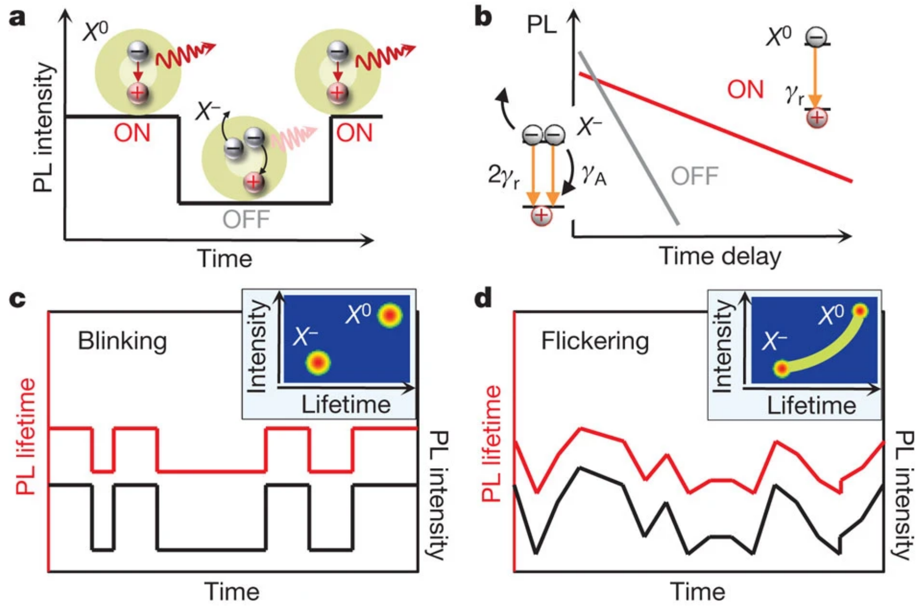

Figure 1.4: The two Models for Blinking: TYPE A vs TYPE B as explained by Galland et al.[11]

The ON coefficient α_{ON} is also around 1.5 but is much more sensititve to the listed parameters and generally is not enough to mathematically describe data: a cutt off function has to be added to follow the experimental distribution for higher times. Based on experimental observations, several modifications have been proposed to the charging/discharging model mostly focusing on the mechanisms for ionization and re-neutralization of the QD to explain the power law statistics of the ON and OFF time probabilities.

At phenomenological level, there are two main types of blinking that have been observed and studied; in this explanation both lifetimes and PL intenisity are correlated in a measurement called Fluorescence-Lifetime Intensity Distribution (FLID) (see figure 1.4):

- TYPE A blinking: for this type of blinking, traditional charging/discharging model is applied; when the dot is charged, it is not emitting because Auger mechanism dominates, so lifetime during off times strongly accelerates respect to neutral. When dot is neutral again, PL emission is measured with given lifetime
- TYPE B blinking: in this model, hot carriers can be trapped in the defect surface states; as a result, the PL intensity fluctuates as a response of the probability of the electron to detrap and end-up in the band edge state where it recombines. For this reason, the dynamics of recombination is the same and so the lifetime is not affected.

A lot of strategies have been studied to suppress blinking in nanocsystals; among them, the most common approach has been reduce the defectuality with certain ligands [11] or by growing a gigant shell around the core to better isolate the emitting core, suppress Auger and tunneling of the charges due to increased distance to the trap. For such system, another interesting effect has been observed called "lifetime blinking": PL trajectory is almost blinking free, instead charge fluctuations would result in changes of the decay [12].

We are still far from understanding completely the phenomenon of blinking in quantum particles and a combined experimental and theoretical approach is fundamental in material science and design

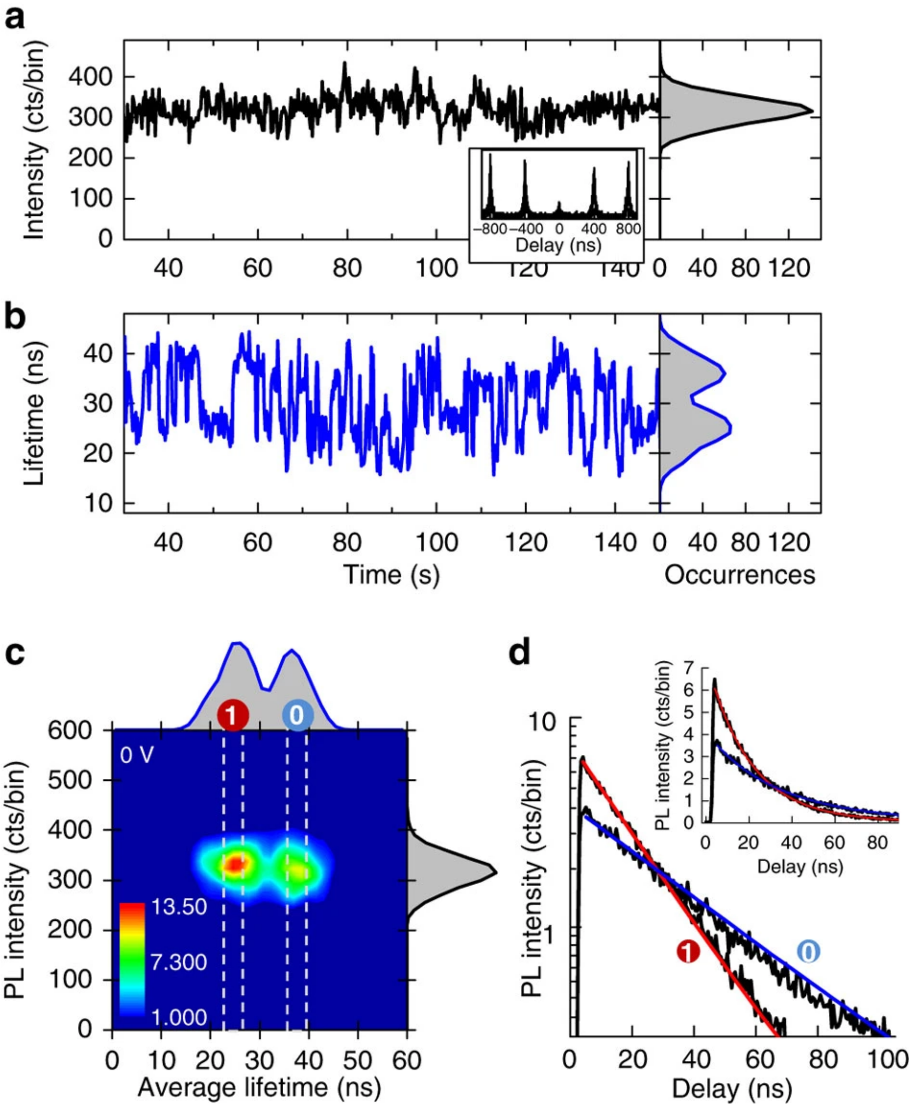

Figure 1.5: Lifetime blinking by Galland et al. [12]

1.2.2. Experimental requirements

Microscope and Resolution

The first requirement to build a SPS setup is to have a home-build microscope, meaning in first approximation, an optical system able to magnify very small areas. As a starting point of this work, we want to adapt an already existing microscope in our laboratory, the Nikon Ti-U Inverted Microscope. In order to do so, we need to verify whether its optics and optomechanics (translational stage, focus knob) are suitable for our project.

In order to fulfill the requirements illustrated in section 1.1, first we need to focus excitation light in the smallest spot possible; the limitation on the dimension of the spot depends first on the dimension of the collimated beam before being focused and secondary on the power of the optics that focus the light. The dimension of the spot can not be infinitely small because it is limited by light diffraction when it reaches the condition for which its diameter becomes comparable with the wavelength; the lateral dimension of the spot is limited by the so called Abbe Resolution limit, which defines the diameter of the maximum point function (called Airy Disk) before diffraction fringes start occurring (figure 1.6, left panel); the resolution can be calculated by the equation:

$$Abbe\ Resolution_{x-y\ plane} = \frac{\lambda}{2 * NA} \tag{1.6}$$

where λ is the wavelength used as excitation, NA is is the Numerical Aperture of the lens.

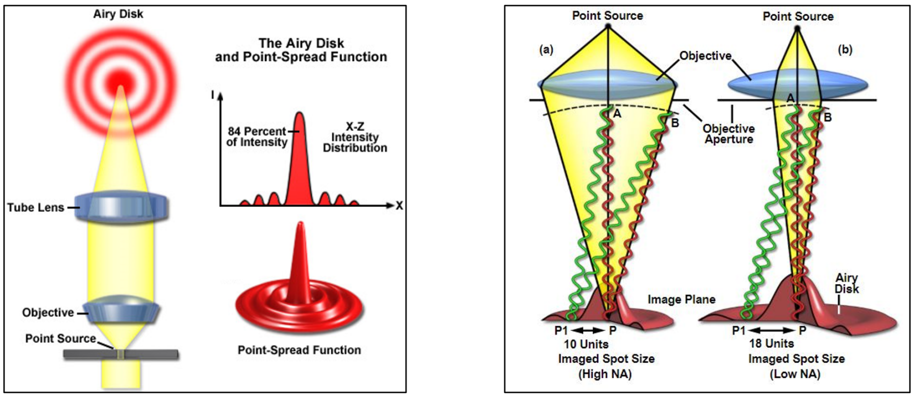

Figure 1.6: Left: The shape of a Airy Disk with first orders diffraction fringes. Right: Influence of NA on the Airy Disk diameter and shape

The Numerical Aperture of an optical element is the defined as the product of the refractive index of the medium where light is propagating and the sine of the angle of aperture ($NA = n * sin(\theta)$). It can be seen as the capability of a lens to curve strongly the light: the highest the NA, the more light can be curved in a smaller angle and so focused into a smaller point and closer to the lens plane.

From equation 1.6 we derive that the smaller dimension of the spot we can obtain is directly proportional to the wavelength of excitation and inversely proportional to the NA of the objective.

To give a practical example, using a green laser with wavelength 500 nm, and an objective with NA of 1.4 the Airy Disk diameter will be 200 nm; For our application, we want to have the smallest point excitation achievable, so we want to get as close as possible to the theoretical limit of Airy Disk. To achieve this, we have to play at the best of our capability with the elements in equation 1.6 to optimize it experimentally:

- λ has to be as small as possible; the choice of excitation wavelength λ though is limited by a lot of different factors such as the absorption profile of the samples and the availability of specific wavelength of commercial lasers. Moreover, below 400 nm, optical glass' transmittance performance start to decrease significantly. This means that by varying the excitation wavelength from 500 nm to 400 nm we can shorten the spot dimension by 20% maximum.

- NA is a much critical parameter on Abbe resolution (see figure 1.6, right panel) as it spans from 0.04 to 1.4 (maximum value achieved nowadays by optics design) and is intrinsically limited by physical costrains. Because it is on the denominator of the equation, it follows that using different objective can drastically change orders of magnitude the spot size. For our means, the highest NA is recommended.

For these reasons, we decided to use a 100x Objective with NA=1.4 from Olympus already installed within the Nikon microscope for our experiments. For this objective, we can also evaluate the Axial resolution along the focus, which is described by the equation:

$$AbbeResolution = \frac{2\lambda}{(NA)^2} \tag{1.7}$$

Putting together the axial and lateral resolution with a 500 nm source, we have a theoretical spot size of 200 nm whose focus sensitivity is roughly 500 nm.

In real experiments, this means that our in plane and axial mechanics has to be in the micrometer range sensitivity. For Nikon Ti-u the fine coarse focus knob can reach the 1 μm sensitivity, while the x-y knob can only reach 5 μm; this limitation is not completely restricting but it defiantly requires to be overcame in some way; it can be partially overcome with sample preparation, as it will be discussed in section 1.3.2.

Once we determined our microscope architecture posses the sufficiently accurate optomechanics elements to focus correctly light on sample into a diffraction-limited spot and move the sample with sufficient accuracy to shine the spot over a single particle to be found over a large area, we need to have the correct processing system to collect and analyze the out coming photons.

Imaging system

The first detector needed is an imaging system: a detector able to convert the spatial distribution of fluorescence light emitted from the sample into a digital image. The visualization of the surface For this means, two types of architectures are possibile:

- A Charge Coupled Device (CCD) or a Complementary Metal-Oxide Semiconductor (CMOS) coupled to the microscope; a CCD is a matrix made of pixels, each able to convert the number of incident photons into a bias value, that can be then processed into a digital image. For this systems, excitation light is shone over a given area and collimated beam of emitted light with the same shape has to be finely directed in free space to the sensor with the only help of mirrors to avid any distortion. Collimated photons will impact perpendicular to the CCD maintaining their reciprocal x-y spatial feature and the 2D image of the sample focus plane will be recreated by software elaboration
- A Point-Scanning Device with a laser source; this system reconstructs a 2D image of the focal plane by scanning the sample's area point by point, recording the intensity for each point and finally reconstructing the image putting together all the scanned points into a matrix. For this imaging system, a Photomultiplier tube (PMT) it is typically used to convert the light intensity collected per point into a bias that is then elaborated by software. In this case, light can be brought to sensor via fiber as reciprocal spatial features are reconstructed in a second stage depending on the scanning parameters.

In either case, collecting a good image of the sample fundamental step in a SPS measurement and in the set-up design. In fact, the image is a map of the sample surface and allows us to visualize micrometric area to be explored looking for single particles; for a 100x objective, easy calculation leads to the estimation that it is possible to visualize maximum a circular area of the sample with radius 180 μm (called Field of View, FOV) . This is a direct way to estimate of the distribution of particles on the sample surface and is the key information that guides the experimental preparation of the sample. With an optimized imaging system, it is immediate to see if we have enough luminescent points in the field of view, or if there are too few, if they're aggregating in microstructures, if the morphology of the film is homogeneous or not, if the luminescent points are separated enough to be measured and so on.

Depending on the chosen image system, light source for imaging can be different: for scanning system, a point source such as a laser is enough as it will be moved along the whole FOV to construct image. For a CCD sensor, the light source is not moving so we can see a portion of the sample as big as the illumination source; laser generally have a small spot compared to the total FOV, so they can image a very small fraction of it, while a lamp generally can be useful to illuminate a wider area.

Spectroscopic tools

After visualizing spatially the sample morphology and evaluating the presence of isolated luminescent points, we can move forward to the spectroscopic measurement on those points to characterize them.
This is the key step because those measurements are the most complex one to realize and optimize, and of course the core ones.

At this step, the laser spot is perfectly placed on the luminescent spot which is emitting photons that are all collected and collimated at infinity by the objective.

- A Spectrometer to measure PL spectrum: light is focused on slit, then dispersed by a diffracting grating and finally focused on a CCD/CMOS. The result is the spectrum of the luminescent point;
- A Hansbuty-Twiss Set up composed by Avalanche Photo Diodes (APD) for both Time Resolved Photoluminescence and Second order Correlation Function $g^{(2)}$

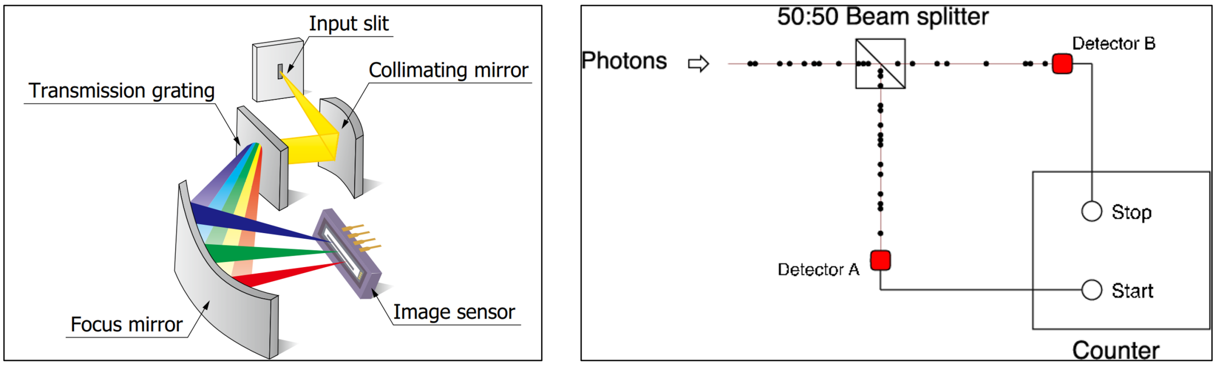

Figure 1.7: Left: Schematics of a Optical Spectrometer. Right: The basics of a Hansbury Twiss Set-up

A schematics of a Spectrometer is reported in figure 1.7; the number of lines in the grating and slit aperture together define the spectral resolution of the system, by defining respectively how strongly light is spatially dispersed and the size of the image. The combined effect of those two elements defines a bandwidth $\Delta\lambda$ which represent how much an ideally monochromatic light will be broadened by the measurement.

A schematics of a typical Hansbury-Twiss Set up is reported in figure 1.7 (right panel). Incoming photons go through a silver plate with a 45 degrees incidence angle, which splits them in two beams with the same number of photons (50:50). Each beam is then directed to a detector which registers each photon event and sends a electrical signal to the counter, who elaborates the correlation.

For this specific application, APD have been chosen as single photon detectors. APD belongs to the family of Silicon photodetectors: a p-i-n junction is used to detect a photon, as when this happens a hole-electron pair is formed, both inducing the flow of a current and a voltage that is measured in the circuit. Differently from a "normal" diode, at the junction in APD a bias voltage is applied to expand the depletion layer. This is called operating in "Geiger Mode", meaning the photodiode is kept at voltages slightly above avalanche breakdown, so that even one incident photons can move the APD into breakdown, generating a flood of electrons with extremely high effective gain. Geiger-mode measurements employ quenching electronics that turn immediately the generated current a series of digital pulses. After the quenching, the voltage has to be restored back to the higher initial potential so the sensor is ready to detect another photon.

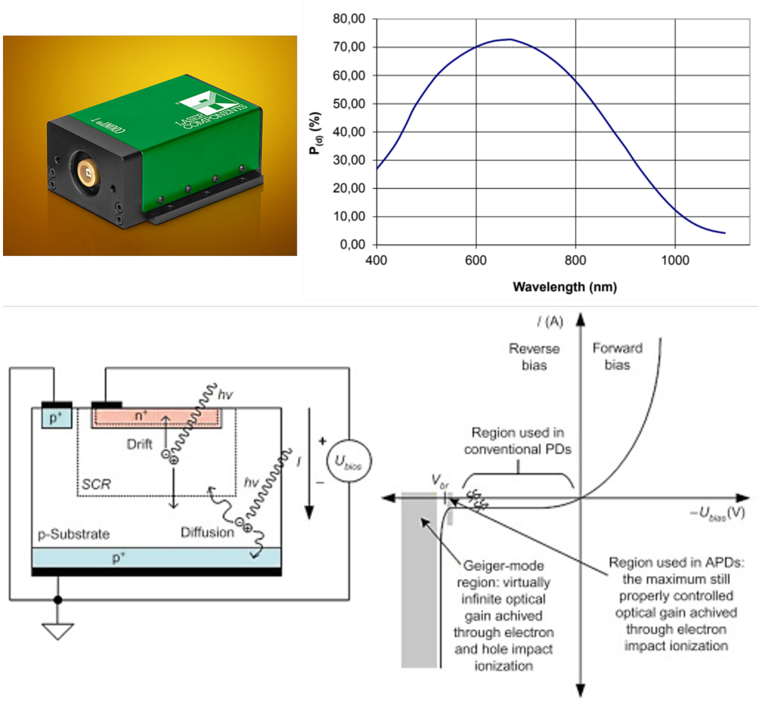

Figure 1.8: Upper panel:An image of a APD detector box and its spectral response, Lower panel: Schematics of the bias-current characteristics of the Geiger Mode of a Si diode

Their performance is the best among all the photodetectors due to their very high sensitivity to ultra low optical signal and highest quantum efficiency (maximum quantum efficiencies reported are about 80%) [13]; a single photon event can generate an avalanche of circa 100 carriers, which is able to determine with high precision the time arrival of the photon. Further more, it has extremely low dark counts, meaning electrical signals measured from other than photon events is very low. These high performance come at some costs: first, the active area of the sensor is very small compared to other photodetectors

(100 μm vs millimeter sensors for most PMTs), making the alignment extremely critical; for our SPS set up, this dimension is still much bigger than the actual dimension of our emissive spot we want to measure, and for this reason the size of the detector is not a limitation, rather it works pretty well if we keep the ratio object vs signal dimension 1:1. Another issue peculiar of an APD detector is dead time: this is the time after the detection of a single photon when the sensor has to restore itself to its working voltage after the avalanche started; during this period of time, the detector is effectively blind as no other photon can be recorded in this period. Because we work in a single photon regime, we do not expect more than one photon event per laser pulse; actually, the expected number of stop pules respect to the start pulses to reasonably keep the single photon statistics is 5%. Moreover, we work with a double detector set up so we can overcome the dead time in the interferometry geometry.

Laser diodes and/or APDs generate an electric pulse everytime a optical event occurs, it is needed to have a Photon Counting Module to be able to correlate these information and reconstruct the temporal dynamics: this is performed by a Time-Correlated Single Photon Counting (TCSPC) system.

When the module reads a start signal due to arrival of a NIM bias, the photon counting starts its analogic timing record by charging a condenser; when a stop bias arrives, the charging stops and the bias value is converted to a time value. All of this tasks are performed by a Time to Digital Circuit (TDC). A point is then added to a histogram reporting time versus number of events, which gives rise to the typical decay curves of TRPL.

Modern TCSPC devices are fundamentally different in design. Instead of operating like a stopwatch, they have independent TDCs for each input channel. The important detail is that the individual TDCs are running off the same crystal clock. If a timing difference is needed, like in classical histogramming, it can be obtained by simple arithmetic in hardware

For our scope, together with the normal TSPC tasks it is fundamental to perform advanded analysis to be able to reconstruct the Second Order Correlation function $g^{(2)}$. We need a more robust tool to be able to collect all of those information. For this reason we picked the Picoquant Module who is able to work in an advanced mode called Time-Tagged Time-Resolved (TTTR) mode. In this mode, the TSPC has the capability to record the arrival times of all photons relative to the beginning of the experiment (time tag), into which chanel it has been recorded in case of double detectors or the picosecond TCSPC timing relative to the excitation pulses when using one channel for laser. This

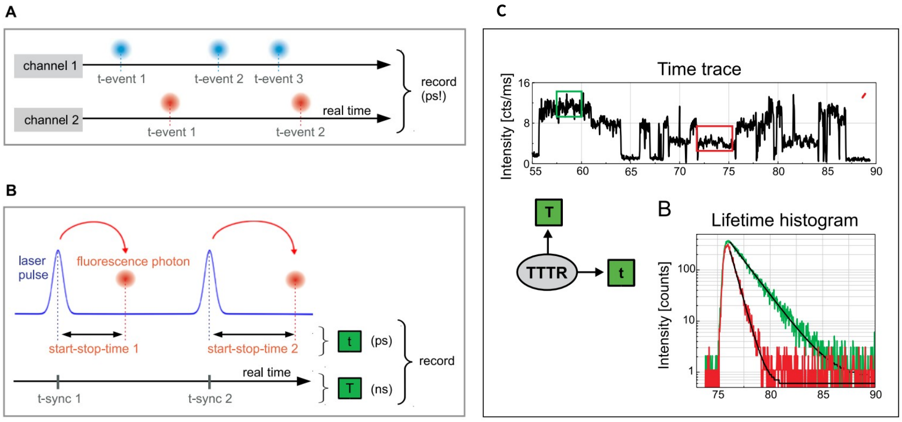

Figure 1.9: Schematics of TTTR working principle. Panel A shows how T2 mode records event, Panel B shows how records are saved in T3 mode, Panel C shows how the T3 data stream can be elaborated to obtain time trace and lifetime histogram

mode is extremely complex but allows extremely delicate measurement. The 32 bit event records are queued in a FIFO (First In First Out) buffer capable of holding several millions of event records. Those records are written in a binary files where all this information is stored.

We can perform two modes of TTTR measurement, depending on the information to obtain:

1. T2 MODE: the two TSPC inputs are the APDs. The events from all channels are recorded independently and treated equally. In each case an event record is generated that contains information about the channel it came from and the arrival time of the event with respect to the overall measurement start. The time tags are recorded with the highest resolution the hardware supports. Dead times exist only within each channel but not across the channels. Therefore, cross correlations can be calculated down to zero lag time. This allows powerful applications such as coincidence correlation

2. T3 MODE: one input of the TSPC is the pulsed laser while the other is the APD. In this case it is possible to record both absolute time and relative time respect to the laser pulse.

The stream of data both T2 or T3 are elaborated by a custom software written by Dr. PhD Matteo Zaffalon. By analyzing the different markers on each photon event it is possible to:

- Associate each photon event to corresponding laser pulse to build the Histogram for lifetime evaluation

- Report the total intensity over time recorded by the APD for PL trajectory
- Evaluate the correlation with an algorithm that for each photon event checks for the closest photon event on the other channel and calculates the time lag between them. All the lags calculated are then stored in memory and summed in histogram mode to obtain total.
- Plot a 3D plot with lifetime as a function of intensity in the so called Fluorescence lifetime-intensity distribution (FLID). This measure is fundamental to understand what type of Blinking is observed.

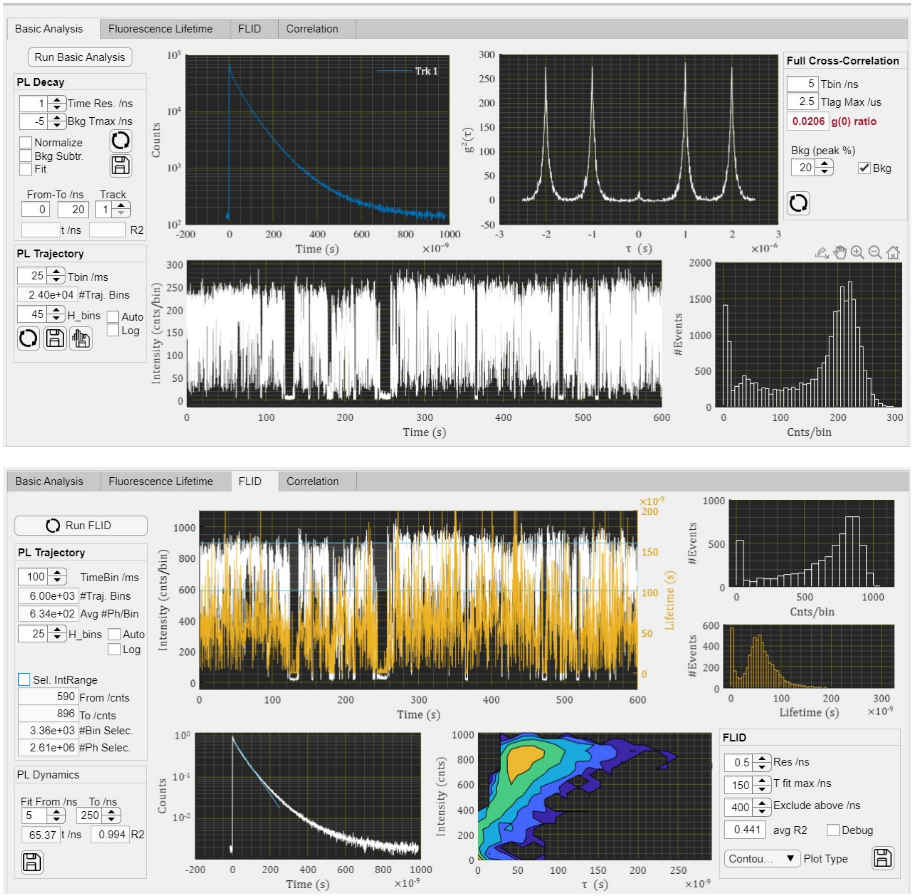

PL Decay
1 Time Res. /ns
-5 Bkg Tmax /ns
☐ Normalize
☐ Bkg Subtr.
☐ Fit
From-To /ns 0 20
Track 1
t /ns
R2

PL Trajectory
25 Tbin /ms
2.40e+04 #Traj. Bins
45 H_bins
☐ Auto
☐ Log

Full Cross-Correlation
5 Tbin /ns
2.5 Tlag Max /us
0.0206 g(0) ratio
Bkg (peak %) 20
☑ Bkg

PL Trajectory
100 TimeBin /ms
6.00e+03 #Traj. Bins
6.34e+02 Avg #Ph/Bin
25 H_bins
☐ Auto
☐ Log
☐ Sel. IntRange
590 From /cnts
896 To /cnts
3.36e+03 #Bin Selec.
2.61e+06 #Ph Selec.

PL Dynamics
Fit From /ns 5
To /ns 250
65.37 t /ns
0.994 R2

FLID
0.5 Res /ns
150 T fit max /ns
400 Exclude above /ns
0.441 avg R2
☐ Debug
Contou... Plot Type

Figure 1.10: Schematics of Photon Correlator software. Upper panel shows the basic Analysis it is possible to perform on T2 and T3 files: Lifetime, $g^{(2)}$, PL trajectory, Histogram of On Off evens. Lower panel shows the FLID analysis to perform on T3 files.

1.3. First Experimental Approaches and Preliminary results

In this section I will illustrate the starting points of the SPS experimental efforts, which samples we selected to start from and how our first trials lead us to understand the main issues of such technique.

1.3.1. Choice of samples of interest

Among one of the first scientific question to address, we first selected a number of colloidal nanocrystal for which SPS spectroscopy could actually address some of the open questions:

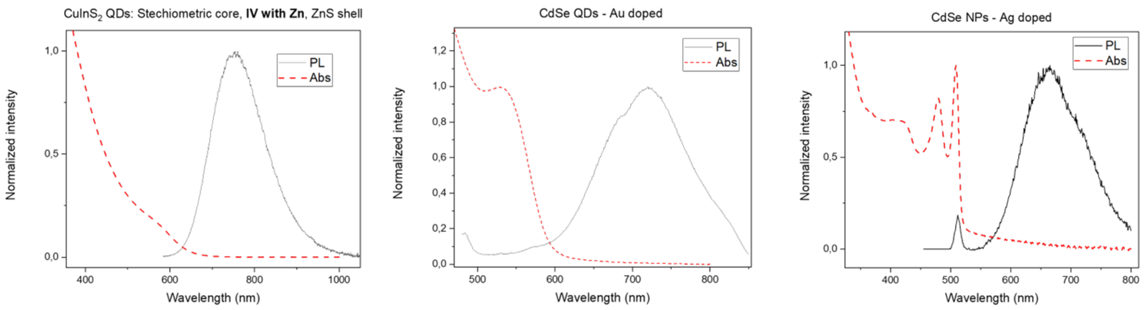

Figure 1.11: PL and Absorption profiles of chosen samples; from left to right CuInS, Au doped CdSe QDs, and Ag doped CdSe NPs

- CuInS. This ternary nanocrystal has been fondly studied due to its very stokes shifted emission and high photo-luminescence quantum yield for applications in luminescent solar concentrators, Bio-imaging [14]. Nevertheless, the origin of their optical properties has been discussed and to this date there is not a definitive answer to such question. Even at single particle levels, only two works have been published and show very different models to explain the experimental data [15, 16]. For these reasons, we decided to tackle this problem by selecting this ternary nanocrystal as one of the candidates for our SPS study.
- Au: CdSe QDs. The synthesis of this QD has been pioneered by our group and it sits in the still-going broad field of doped nanocrystals [17]. The reason behind such broad PL can be understood at single particle and the effect of number of dopands on the optical properties can be investigated by a single particle
- Ag doped Nanoplatlets (NPs). For this NPs, it is possible to observe both the Band Edge emission of the nanoplatlets at 500 nm and the dopant PL [18]; with SPS it

is possible to investigate what is the real ratio between those emission in a single crystal or if it is due by sub-populations of undoped and doped nanocrystal. This information is completely lost in the ensemble spectroscopy and could serve as a tool to improve the chemistry of such systems.

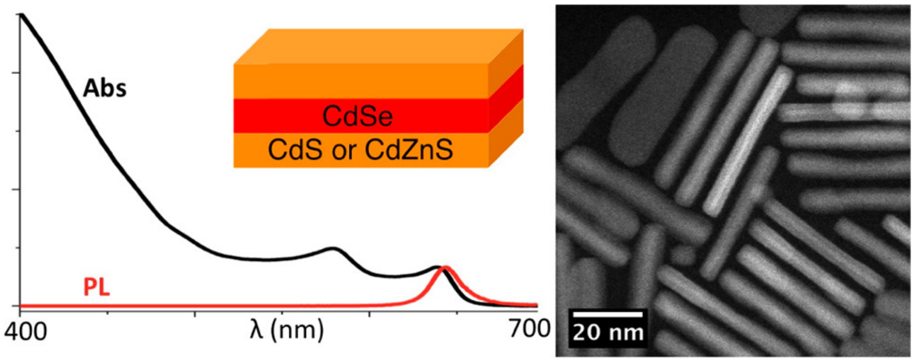

Figure 1.12: Schematics of optical and structural properties of Nanoplatles CdSe/CdZnS Core-Shell (from [19])

All of these samples have in common an emission in the red region of the visible spectrum, above 600 nm. For this reason, to selected a good emitter which can serve as a reference for the set-up alignment and optimization. Among the available ones in out lab, we selected Colloidal CdSe/ZnS Nanoplatelets (NPs) (figure 1.12) Colloidal NPs are quasi-2D semiconducting nanocrystals in which the quantum confinement regime is reached in one direction a few nanometers thick, in the other two directions the NCs is some tens of nanometers wide.

The synthesis of colloidal NPs requires an high degree of control in the topological growth of NCs in colloidal condition, this makes the relative synthesis more complicated then the one for CdSe QDs.

The main feature that distinguish the optical properties of CdSe NPs from QDs ones is the sharp distribution in the confinement size of the nanoparticles. Despite the overall synthesis results more complicated then the QDs one, requiring high topological control in the growth phase, the control in the quantum confinement size results much more precise for CdSe NPs then for QDs. Due to the planar shape of NPs, quantum confinement can be controlled by changing the number of atomic layers constituting the NCs, this can be done manipulating reactants concentration during the synthesis.

Since the dimension distribution in the quantum confinement direction approaches a delta, the emission spectrum of CdSe NPs results to be very narrow (around 7 nm, FWHM) [20] this makes such material one of the most promising system for the production of LEDs.

The spectral tunability of CdSe NPTs is lower then the one seen for QDs because it is related to the discrete number of atomic mono-layers (MLs) constituting the NCs thickness. The E_g can assume values of 2.68 eV for 3 MLs, 2.42 eV for 4 MLs and 2.25 eV for 5 ML, incrementing the ML number it is possible to reach the Bulk E_g of 1.74 eV[21].

Those crystal are very well known in literature and have a high quantum yield and stability [19, 22, 23] ; in our case, PLQY measured is around 65%. for this reason we selected those samples as our starting particles to test the working efficiency of our set-up.

1.3.2. Samples fabrication's methods

Sample Fabrication is a crucial step in single particle experiments. In our experiments, samples are solid films deposited on a transparent substrate.

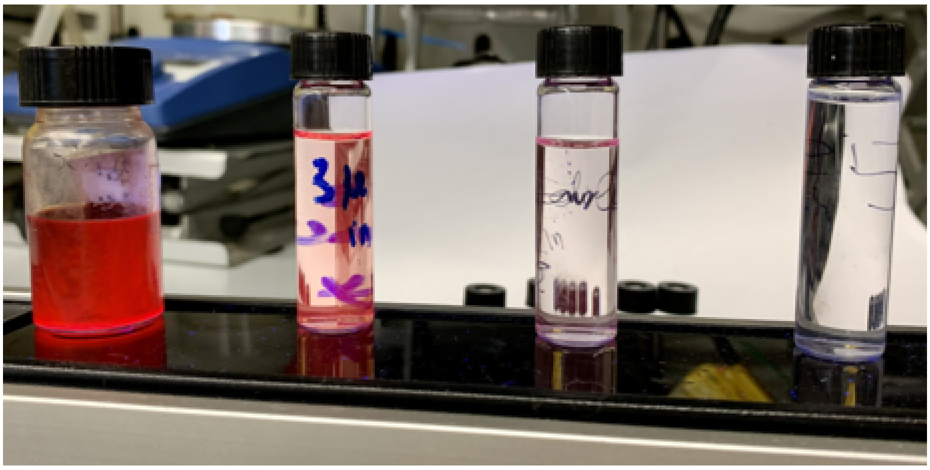

Figure 1.13: A typical dilution process to reach the desired concentration. We can qualitatively monitor the quantity of NCs by seeing the color of the solution and its emission under a UV lamp

First of all, when working with colloidal solutions where nanoparticles are dispersed, the first step is to dilute starting solutions by a factor of at least 10^4. They generally have to become fully transparent (see figure 1.13). This process is easy to realize practically but is not always something that keeps the colloidal crystals stable: in fact strong dilution can result in detachment of ligands from the surface, leading to suppression of PLQY or even etching of the crystal structure.

The adequately diluted solutions are then evaporated on a clean glass coverslip with thickness 170 μm (the focal length of our immersion oil microscope). Coverslip is then turned upside down and glued to a glass substrate to be placed on the microscope mount.

Another key factor is the film deposition: in fact when particle are deposited in a solid film their stability can be strongly effected. Some nanoparticles are completely quenched when dryed in film as already known for a lot of single molecule studies [24], some of them just drop their PLQY due to physical-chemistry processes induced during the fast evaporation of solvent and adhesion to substrates.

In SPS, film preparation is even more complex because, adding to the complexity of dilution and phase change solution to solid, particles do not have to form any agglomerate such as dimers, trimers or any other type of arrangement. For some nanocrystal, this condition is not easy if not impossible to obtain without turning the emission off. When you experimentally try to separate them forcing them against the most thermodinamically favourite aggregation process, their stability can drop and their emission completely quench.

Deposition techniques can be different, based mainly on the volatility of the solvent where the nanocrystals are dispersed or on the viscosity of the medium in case of polymer embedding. The most important thing is to deposit a film made of one single layer of material with ideal atomic thickness; this is because we need to be sure that, once aligned on the particle, that particle has the least probability of having another one deposited on top of it: this means that our deposition system has to aim to a single atomic layer thickness.

Two main techniques have been used in our experiments:

- Drop Slip: this technique is used with highly volatile solvents such as hexane. The coverslip is placed at a 45-degree angle to the work surface and leaning against a wall. From one of the two top corners, a 30 μm drop is dropped, which will slide along the surface of the coverslip, depositing the nanocrystals as it evaporates; then the pipette is moved sideways and another drop is dropped and the movement continues until it reaches the opposite vertex. This method ensures that multiple layers cannot be deposited because the drop flows over each point once

- Spin Cast: this technique is used with either less volatile solvents or more viscous solutions e.g. toluene, or polystyrene in toluene. For these solutions, evaporation needs to be enhanced by fast spinning of the sample during the deposition and this process is realised with a spin coater. A spin coater is fundamentally a disk with a vacuum line in the middle that keeps a solid substrate strongly attached to it while it spins at very high rotations per seconds. This allows the deposition to be much faster and more uniform; in case of solid films in polystyrene, it is possible to regulate the thickness and uniformity of the solid film by regulating the spinning velocity, time, and acceleration via software control of the Spincoater fig . The faster the spin velocity, the higher the spread of the drop and so the thickness of the film; nevertheless, a lot of material will be spun out and wasted, making the film less rich in nanoparticles. A specific mix of all parameters has to be optimized for each solution.

The deposition has to be finely optimized to obtain a sufficient dispersion of nanoparticles in the film; this is a product of how much solution can be diluted without damaging the sample and how well the films can be deposited. A trade-off has to be found between having particles too dispersed on the film, because it will make it hard to find them with the microscope, and having them too concentrated so that they are not enough distanced to measure real single particles with given spatial resolution;

A key question during this process is: what is the ideal distance between particles to achieve when preparing a sample? That is dictated by the magnitude of the laser spot. In microscopy, the minimum distance in order to be able to distinguish two objects is called the Rayleigh criterion: it states "two images are just resolvable when the centre of the diffraction pattern of one is directly over the first minimum of the diffraction pattern of the other". In our case though, the width of the beam diameter is so much bigger than the size of our objects so it will never be possible to resolve them in a 1 μm spot, as there can be up to 100 particles completely unsolvable in a typical laser spot. For this reason we really need to make sure that the single luminescent spots are very far from each other.

By taking in account the knob sensitivity, the resolution of microscope and the spot size, we consider a good dispersion if nanoparticles are mat least 5 μm away. Our method to optimize deposition is going to be driven by this goal.

1.3.3. Readaptation of Confocal C1 Microscope

Our first idea in designing the SPS set up was trying to convert and adapt the Confocal Head Nikon C1, typically used for traditional confocal fluorescence microscopy, to an efficient SPS system. In this section there it will be illustrated how we modified the optics and basic function of such system to adapt it to our application.

Description of Confocal C1 Head

This idea came with consideration that building a system from scratch compared was much harder compared to using an already established technology as a starting point. Confocal C1 presented an already aligned system and a reliable technology, so as a first try it seemed like a reasonable try to see if it could match the requirements of SPS

In figure 1.14 it is reported the basics opto-mechanical elements of Confocal C1, the confocal head has an already aligned opics which works to create an image of the sample

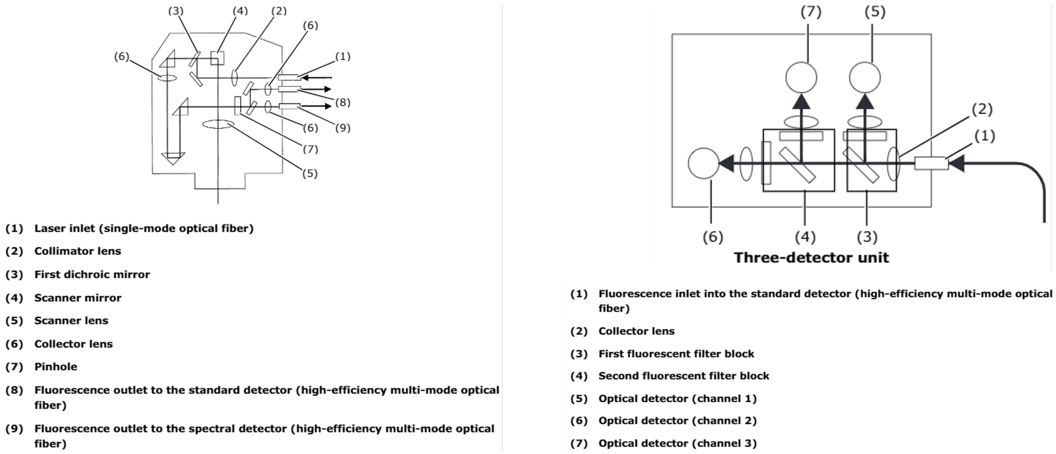

Figure 1.14: Left: Schematics of the optics within Confocal head C1. Right: PMT detector system where light is split in three channels for Blue, Red and Green signals..

by line (raster) laser scanning. Laser light enters the confocal head via single mode fiber and is collimated by lens (2) before being deflected by the scanning mirror and lens; those optical elements are finely controlled by galvanometers in order to achieved a very high spatial resolution. This process is called raster scan: the interest area is divided into lines, and each line is divided into a certain number of points: the galavano-elements are electrically driven to perform this scan automatically with the indication of the time dwell per point, the number of points per line and the number of lines. For each position of the galvano-mirrors i.e for each selected point of the sample, laser light is then directed out of the confocal head to a specific point of the FOV through the objective; light collected from each point is then collected by the objective and brought back into the confocal head following the same path as before. Then, once passed the final elements in the head, it is deviated to a different path: it passes through the dichroic mirror, which is designed to spectrally cut the residual excitation wavelength, and finally it is collected by the collector lens. This is the only movable element, because it is designed to finely compensate all the deviation and drifting of the optics from the ideal position and finely optimize the alignment. Light beam is then directed to an adjustable size pinhole and finally focused into a 1 mm multimode core fiber. Fiber brings all the collected light directly into a standard imaging detector which is composed by three PMTs (blue, green and red): depending on the wavelength, light is either reflected or transmitted until it reaches one of the three PMTs (figure 1.14, right panel). The intensity recorded on each channel is stored into memory of a RGB pixel by the EZ software. Once saved, the galvanometer moves to the next point and the procedure is repeated, until all points have been scanned and measured. The final digital image is then reconstructed by creating a matrix of pixels whose individual intensity is the sum of the intensities recorded by PMTs.

The number of pixels is determined by the number of points scanned by the galvanomirror and lens.

Our method of measurement

Our initial try was using this system as it follows:

1. Scan the entire FOV as standard use of the confocal imaging system, optimize the focus and then move around the sample with the x-y translational stage looking for a good area of the sample where luminescent particles are well enough dispersed
2. Reduce the scanned area to a micrometer area where the luminescent point is located; this is performed with the help of the software which allows fine control of the galvanomirrors: it is possible to select with submicrometer precision the starting and ending point of the scan in order to perfectly align over the point of interest
3. Once scanning parameters are set-up in loop over the area where the intensity of PMT is maximum, we are sure to be aligned and to continuously excite and collect light from the same point; the fiber outgoing from the confocal head is now brought to the spectrometer and to the APDs to perform spectroscopy.

This experimental approach was fondly optimized over several weeks in order to be able to take good measurements. Several limitations emerged and I reported a short list of the main issues.

- PROBLEM: Presence of auto-fluorescence of immersion oil and of glass defects dirts and defects. When going towards low density particle films, the contribution coming from the background became more and more significative over the sample signal, to the point where the it could become dominant over the nanoparticle luminescence.

  SOLUTION strategy: I studied the avaiable Oil immersions for microscopy and selected the one with the lowest auto-fluorescence with UV or near UV excitation source available in the market (Leica Type B immersion Oil). Furthermore, we moved to a lower excitation energy within the available ones (488 mm). The result was a strong decrease of autofluorescence covering the signal. Regarding microscopic glass dirt and defects, their presence would insert a parasitic fluorescence and a centers where particles accumulate more easly avoiding desired dispersion; I optimized a new cleaning procedure based on successive acid baths with different molarity in order to find a trade-off between etching the surface but not to the point of increasing the roughness

- PROBLEM: Spectral cuts deriving from the optical characteristics of dichroic mir-

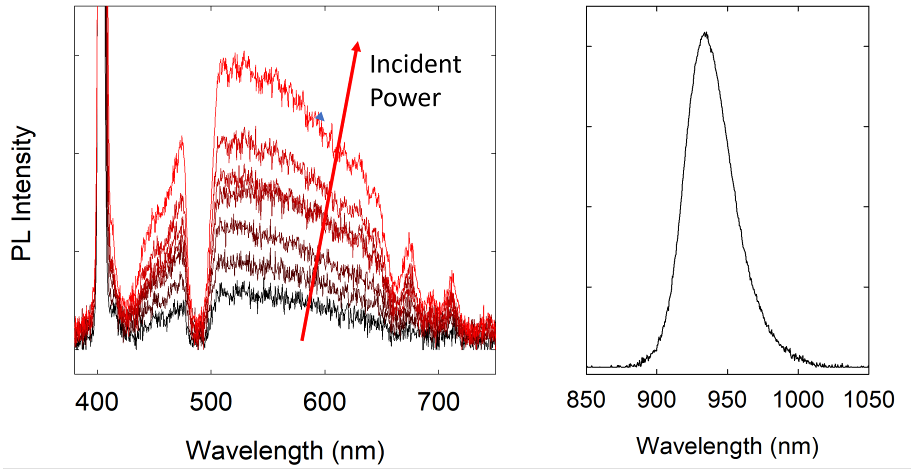

Figure 1.15: Left panel: Typical spectrum of the Background (Oil + internal fluorescence of the microscope optics). Spectral features are due to dichroic measure. Right panel: Spectrum of the photocell measured with spectrometer, giving rise to high background on APDs

rors compatible with C1 Head.

SOLUTION: Due to the nature of the confocal head optics, C1 comes with a customed set of dichroic mirrors that could not be replaced with any other available optics in the spectroscopy lab because of geometric constrains. Knowing this effect on the emission spectrum, the idea was to work in a region of interest where the optical response of the filter was as flat as possible and to convolve in future the spectra with the shape of transmission.

- PROBLEM: In order to have the best alignment, for the whole time of spectroscopic measurement, the scan head has to work somehow opposite to what is designed for i.e it has to be as still as possible on one specific point.

  SOLUTION: A lot of test have been done to control the head scan movements in order to minimize it but also keeping the rest of the optics working perfectly; with some hardware modification on the piezos and a combination of advanced software knowledge, we managed to do an "apparent" scan by keeping the head on the same pixel and to keep the scan for the longest time and with the highest number of repetition. The maximum achievable for this mode is a 5 minute consecutive measurement, which is quite limiting.

- PROBLEM: APDs both record a high number of stops only when the fiber from confocal is connected to Hansbury-Twiss set-up.

SOLUTION: We tried to understand where this source of photons was coming from and concluded that it was a very narrow NIR emission (see figure 1.15, right panel) peaked at 940 nm. This was ascribed to the presence of a photocell within the head that was needed to control the galvanomirror movements. Because it is not switchable off, we filtered it out with a specific filter on the APD box.

- PROBLEM: Laser scanning comes with the problem of photo bleaching and damaging of the sample: high power can alter the the surface of the quantum dots and make ligands detach and crystal structure damage, leading to loss or complete quench of photoluminescence.

  SOLUTION: I studied how to embed efficiently nanocrystal inside a polymer matrix, in order to protect them from damaging, oxidation and any other form of contamination (see section. For CdSe/ZnS NPs, the best choice was using a 5% weight Polystyrene in toluene solution.

Following the optimization of the measurement, we were a able to get to some interesting results which will be discussed in the next section.

1.3.4. First Results and Conclusions

After optimizing the sample preparation and nanoparticles dispersion of our reference samples i.e collioidal NPs CdSe/ZnS described in section 1.3.1, here we report the most important results we obtained with such set-up.

I reported three significative particles which sum up the statistically most frequently found results.

For all particles, we excited with a 488 nm modulable laser; the repetition rate is externally modulated with the use of a Wavefunction Generator that can control both shape, frequency and duty cycle of the electronics; the frequency was chosen to be 450kHz because it is the one at which the fluence was comparable with the one required for such systems. The cube used had a 550 nm dichroic cut and a emission filter with edge at 600 nm.

The data reported for each of these particles are Correlation Function $g^{(2)}$, PL trajectory and the Histogram distribution derived from the latter; this particular graph is mathematically derived from the PL trajectory as it is the sum of number of PL events (y events) with a defined intensity (x axis). A peak in such histogram for positive counts values reflects the existence of an emissive ON State with a given intensity (depending on the PLQY of such emission and incident excitation power). More than one emissive state is possible: in literature, the state with the highest intensity is called the bright state while the others (if present) are called grey states (as their intensity is half way between bright and dark). A peak of events at dark-level counts intensity is called an OFF (dark) state. The intensity of such peaks represent the probability of the particle to either be on the off or on the on state; at single particle is related to the Auger probability and so is a measurement to the total quantum efficiency of the system.

For any of those particles, it was not possible to detect PL. All measurement where just too noisy to be able to clearly distinguish the signal over the background. The reason was attributed to the fact that the signal is too weak and cannot be discriminated from the electrical noise even at the maximum integration time and averaging. The calculation was performed by evaluating the number of photons per pixel per second incident on the sensor in the approximation in which all photons on the APD are directed to the CCD. This calculation was possible only at this stage of the set-up design because we could not predict the number of photons expected from such a complex system. Now, with the help of the APD, we extracted the Photons/Pixel/second to be maximum 10^4 photons/second/pixels (APD is considered a single pixel element).

With the APD counts value, we can predict how many electrons are flowing per pixel after the arrival of such number of photons during the integration time. Then we compared this number of electrons to the ones that are generated in the circuit and contribute to the total noise; the typical sources of noise in a CCD/CMOS sensor are:

1. Photon noise results from the inherent statistical variation in the arrival rate of photons incident on the CCD. Photoelectrons generated within the semiconductor device constitute the signal, the magnitude of which fluctuates randomly with photon incidence at each measuring location (pixel) on the CCD. The interval between photon arrivals is governed by Poisson statistics, and therefore, the photon noise is equivalent to the square-root of the signal. In general, the term shot noise is applied to any noise component reflecting a similar statistical variation, or uncertainty, in measurements of the number of photons collected during a given time interval, and some references use that term in place of photon noise in discussions of CCD noise sources.

2. Dark noise arises from statistical variation in the number of electrons thermally generated within the silicon structure of the CCD, which is independent of photon-induced signal, but highly dependent on device temperature. The generation rate

of thermal electrons at a given CCD temperature is referred to as dark current. In similarity to photon noise, dark noise follows a Poisson relationship to dark current, and is equivalent to the square-root of the number of thermal electrons generated within the image exposure time. Cooling the CCD reduces the dark current dramatically, and in practice, high-performance cameras are usually cooled to a temperature at which dark current is negligible over a typical exposure interval.

3. Read noise is a combination of system noise components inherent to the process of converting CCD charge carriers into a voltage signal for quantification, and the subsequent processing and analog-to-digital (A/D) conversion. The major contribution to read noise usually originates with the on-chip preamplifier, and this noise is added uniformly to every image pixel. High-performance camera systems utilize design enhancements that dramatically reduce the significance of read noise.

The following equation is commonly used to calculate CCD camera system signal-to-noise ratio, considering all forms of noise listed above.

$$SNR = \frac{PQet}{\sqrt{PQet + Dt + Nr^2}} \tag{1.8}$$

where P is the incident photon flux (photons/pixel/second), Q(e) represents the CCD quantum efficiency, t is the integration time (seconds), D is the dark current value (electrons/pixel/second), and N(r) represents read noise (electrons rms/pixel).

Using such equation to compute the SNR of our Hamamatsu CCD with maximum integration (10s) and reasonable number of averages (200) to have a measure as long as the lifetime of a single particle, the value obtained is still below 10dB meaning that the signal is completely undetectable with such system; a new Spectrometer system with higher overall sensitivity is definitely needed to measure emission spectra. Nevertheless, I reported the correlation, blinking and statistics measurements for three subsequent measurements.

First particles looked like Particle A, whose measurement are reported in figure 1.16

The first and easiest to get information to understand if the luminescent spot could possibly be single particle is seeing them blink; with our imaging system being a raster scan, it means that they would appear, disappear then reappear again when performing repetitive consecutive scans over the area of interest. When this would actually happen, we could select that point and measure. $g^{(2)}(0)$ is substantially identical from the adjacent $g^{(2)}$ peaks, proving that we are not on a single particle; PL trace shows a clear blinking behaviour for the first 40 seconds of the measurement, leading to a complete switch off of

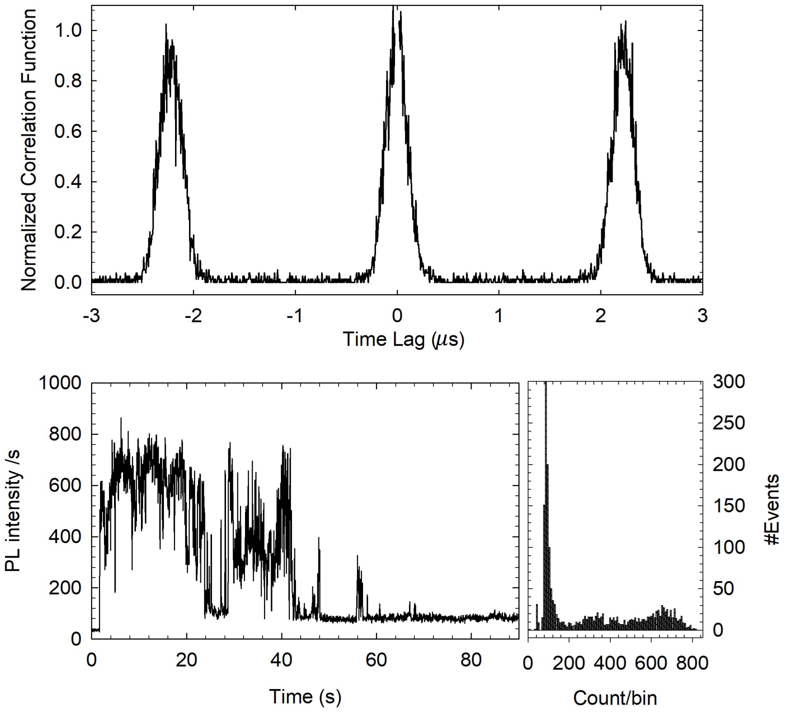

Figure 1.16: $g^{(2)}$, PL intensity trace in time and histogram of events for a Particle A.

the PL. By looking more in details to the histogram, we can observe there are multiple levels of intensity almost continuous, progressively going to 0. We concluded that those are blinking cluster with a low number of particles which progressively stop emitting. Photo-bleaching is very rapid as the maximum of intensity is high and decreases very rapidly towards 0.

For the sample production, I studied strategies to reduce aggregation and make them more distributed and less subject to photo-bleaching. The first strategy already fondly studied in literature [9] is embed the particles in a polymer matrix; After optimizing both the chemical recipe and the spin coating procedure, I re-performed the same measurements.

In figure 1.17 and 1.18, we reported the most important results. Most particles were not single, but the photo-stability resulted much increased. As a descriptive example of most data, in Figure 1.17 we clearly see a 3 level intensity distinguishable and ascribable to the sum of three particles progressively shutting down, each of them remaining stable on their emitting state. As a result, the histogram has more defined aspect, with more discreet and defined peaks compared with the almost-contunuum distribution of figure 1.16 The total average lifetime before bleaching resulted increased, from below a minute to more than two minutes in most cases. Still the, $g^{(2)}(0)$, is also very much similar to the $g^{(2)}$ at

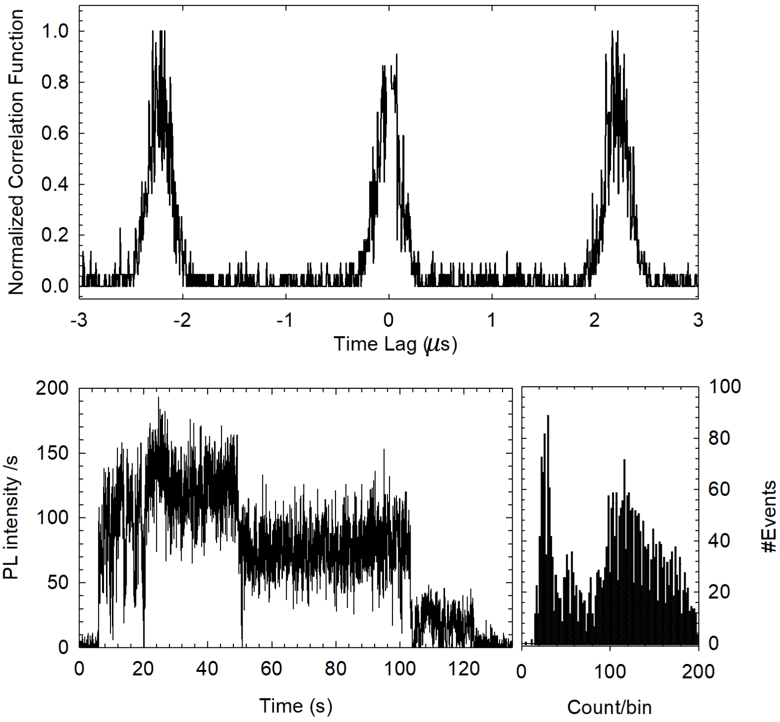

Figure 1.17: $g^{(2)}$, PL intensity trace in time and histogram of evens for a Particle B.

different time delay which further proofs that single particle regime is not achieved.

We kept on this strategy by going into a much more drastic dilution of the starting solution This would come with the price of having to look for a particle for a much longer time due to high spatial dispersion.

After several weeks of sample preparation and optimization, results were very poor; most emissive points visible with roster scanner + PMT imaging system where always multiple particles as proofed by the measurement of $g^{(2)}$.

Nevertheless, I focused my attention to the fact that the luminescent points were almost in the noise of the PMT at the maximum of their amplification and integration, meaning that their presence was barely detected over the background when doing a total area scan. In such points, the typical result is reported in figure 1.18. In this case $g^{(2)}(0)$ is slightly lower than the adjacent peaks (integral between second and peak at 0 is 0.78) but still far from the 0.2 goal; the signal thought was extremely weak and counts per second were merely above the electronic noise at best performance possible, making it hard even to finely adjust focus: average noise is 15 counts/bin and maximum signal is 60 counts/bin. With such signal to noise ratio it was difficult to analyze them. And mostly, the single particle is expected to have much lower signal.

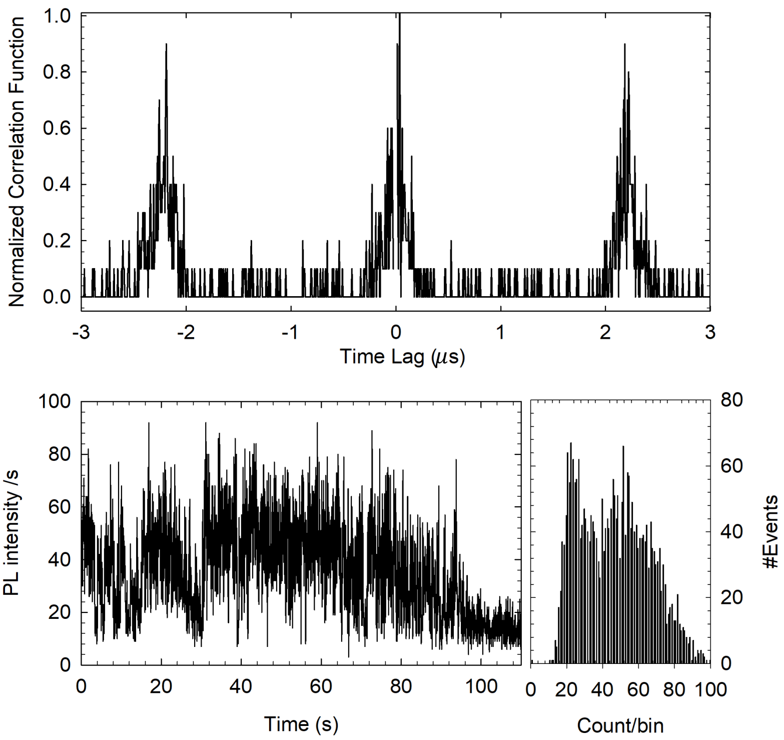

Figure 1.18: $g^{(2)}$, PL intensity trace in time and Histogram of evens for a Particle C

This first ever-approach to Single Particle Measurement lead to these results which were the closest to a single particle ever recorded in our lab. Nevertheless, some of the unsolvable limitations of such method are key points to achieve the desired goal. Most of them are related to the excitation path and are summarized as follows:

1. Only with external software control it is not possible to have sufficient fine control over the power and beam goes directly in fiber.
2. The choice of source laser wavelength becomes extremely poor as it will have to both be a fiber laser in order to be compatible with Scan Head entrance and match the dichroic of Nikon.
3. The limitation of laser source not only requires good wavelength but also good time response when modulated: most of our temporally resolved data were actually not accurate, because the Instrument Response Function (IRF) was much slower than the sample optical signal.
4. PMT exposition cannot be changed more than a certain value which depends on the software control and the maximum value accessible via software is not enough to get a good Signal to Noise Ratio

As a last try to use this set–up and overcome such limitations, related mostly to the excitation source, we tried to have another excitation path decoupled from the scan head fiber system. I designed and upright excitation architecture to freely be able to choose the laser beam excitation in free space and collect light from the confocal head as before; the result is showed in figure 1.19: a metallic breadboard was held on top of the microscope by four metallic poles held to the optical table , a hole has been carved in the breadboard in order to let the objective 20x (NA=0.5) down to the sample; laser is then placed into the breadboard and directed with a highly precision controlled mirror into the middle plane of the objective which foccus the light into the sample. The objective is mounted over a traslational stage with all the micrometers control to match the required sensitivity.

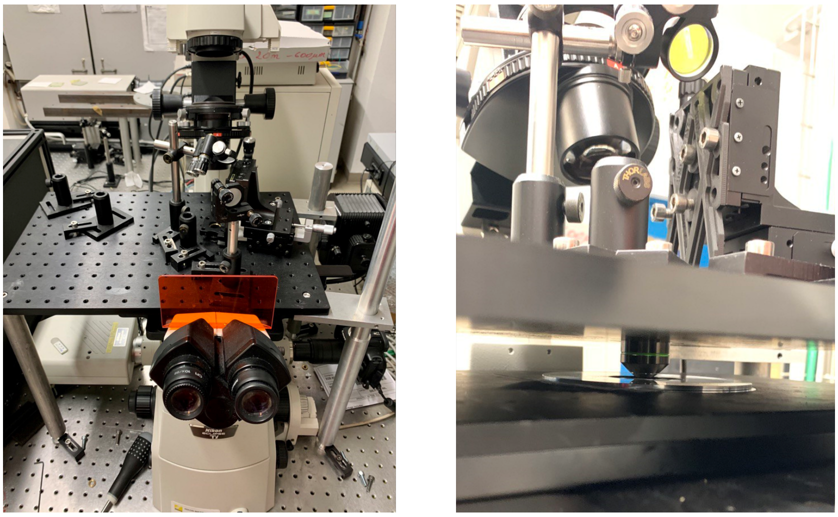

Figure 1.19: Geometry with upright excitation

The result was good, but having such difference between the numerical aperture of the excitation and the collection lead to a great number of aberrations and made the alignment even more complex because of the matching of those two optical systems. Moreover, vibrations are not in phase because the two objects were moving differently respect to the ground and a lot of straylight is added because of loss of confocality.

In conclusion, our first set-up idea, with all due improvements, did not alow us to measure proper single particle measurements, Those blinking multi particles are in fact barely visible above noise with PMT and with APDs and its PL spectrum was not detected. The excitation path of such set-up had some unsolvable issues but also collection of light is not actually the best. If we consider that these measurements have been performed on highly emitting dots as proofs, we can conclude that this type of set up at its highest potential has to an overall low efficiency and low customization possibility, In fact, optics within the head are not to be modified and increasing the light collection efficiency is simply not possible.

For this reason, with the acquired knowledge and familiarity with the microscope and its optics, we decided to build a more flexible system with a different light paths of both excitation and emission lines. In the next paragraph, I will describe a different approach developed in EPFL as a visiting student in Prof. Galland Group to learn about new geometries for such experiments.

1.3.5. Visiting EPFL: a new approach to the problem

During this phase of research, I have been invited to Professor Galland's in Ecole Polytechnique of Lausanne. He has been performing SPS on colloidal quantum dots for many years so we could use its expertise and facilities to learn better how to improve my knowledge on the set-up.

For this reason, I brought the solutions of our samples of interest to Lausanne and prepared the films in loco following the optimization process studied in Milan. The substrate of choice was patterned Silicon, properly cleaned with HF before deposition in order to remove the native oxide. The deposition technique chosen was Spin Coating of dried solutions.

The strategy for characterization was using a Raman-μPL spectrometer. This system, in its very simple architecture, is composed of a 60x Air Objective, a translational sample stage completely motorized in and out of plane with piezo-control and a spectrometer with a nitrogen cooled CCD.

The result is reported in figure 1.20 and 1.21: with the software is possible to select maps mode, meaning we can expand the beam to cover the entire FOV, move the spectrometer grating on 0 order, and make light shine directly on the sensor in order to visualize the spatial distribution of light. i.e the imaging mode. Then it is possible to remove the beam expander and go back to focused laser, move the grating to First Order, select a specific central wavelength with a specific band width and scan point by point the intensity of that spectral component Finally, once the interest points' position have been saved, it is possible to collect the full spectrum of those points by driving the piezo to move the sample where the laser spot is focused.

This method allowed us to optimize both the dilution of the solution as well as the spinning parameter in order to make a good quality film with luminescent points enough spaced. We started with a patterned silicon substrate to accumulate the dots on area to optimize the signal (fig 1.20) and then move to a flat simple silicon substrate once the measurement has been optimized (fig.1.21).

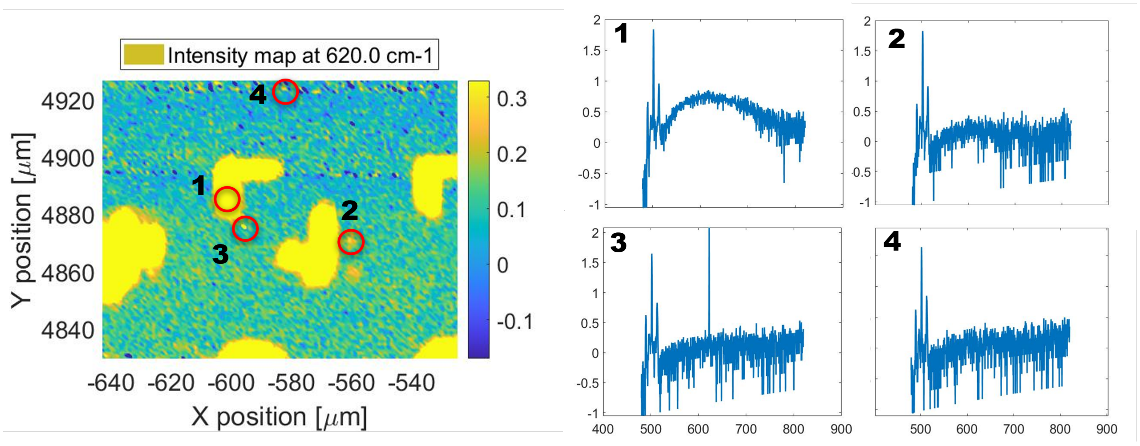

Figure 1.20: Imaging Map of Au: CdSe QDs dispersed on a patterned silicon substrate; pattern is made of L shaped island, where the dots accumulated (strong yellow intensity). The four spectra reported are the PL measured in different points indicated on the Map

Imaging and PL has been possible with ease, but unfortunately within the Raman set-up there was no possibility of Time Resolved Measurement and Correlation function; the films deposited and mapped are then moved to the Hansbury-Twiss Set-up where those measured are performed completely "blind", by moving the excitation spot randomly over the surface looking for signal spikes. Also, incident power on the sample was very low because the optics (mirrors and lenses) of their set-up was optimized for Near Infrared light while our excitation was Visible to UV: the total intensity on the sample was damped by a factor of 100 by not spectrally optimized coating. Every measurement of Correlation would last more than 20 minutes to have a total signal barley distinguishable from noise level. For this reason, in the limited amount of time available in the facilities, we were not able to perform good single particle measurement

Ultimately, even though it was not possible to obtain a good single particle measurement, this experience was extremely useful for me to understand an alternative design for our home-built set up. The knowledge acquired together with the expertise on C1 confocal head adaptation, lead to the design of the final geometry which will be discussed in the next section (1.4).

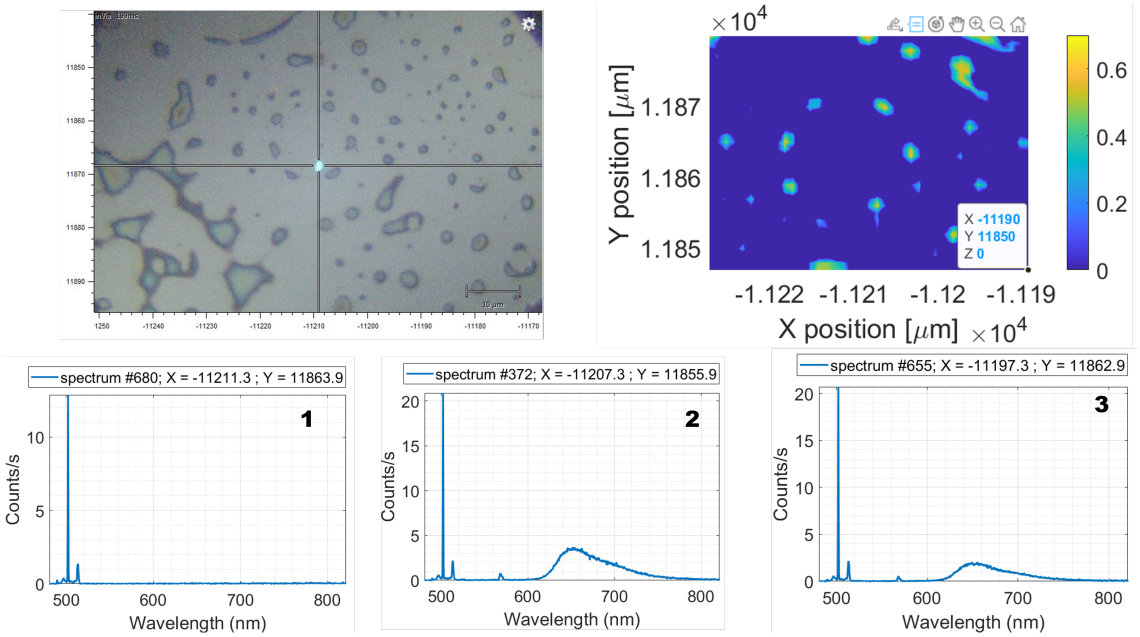

Figure 1.21: A combined effect of widefield and confocal mapping of Au:CdSe QDs spin-coated on a clean Si substrate

1.4. The optimized set-up realization and final results

The SPS set up has been completely re-designed in order to be able to have complete freedom over the excitation line (beam dimension, output power, time resolution, spectral purity) and the emission light (spectral filtering, image dimension, detector choice),

For this reason, I studied all the possible ways to couple light within the microscope: the demand is to have an easy coupling, a facile alignment procedure when switching from one source to the other and, mostly, highly reproducible and finely correctable.

The key idea was to use the epifluorescecence arm installed on the back of the microscope to bring light to the sample; epifluorescence is a type of fluorescence geometry where the excitation and emission light go through the same lens (i.e the objective) which serves both as focusing element and collecting optics. For samples where the fluorophore can be excited with a wavelength with a good stokes shift from the emission, it is possible to bring the maximum of light to the sample and cut it out completely without distorting and/or cutting the shape of the emissive spectrum. Luckly, this is exactly the case for most semiconductuive nanoparticles;

A typical epifluorescence optical path is described in picture (1.22); white light is emitted

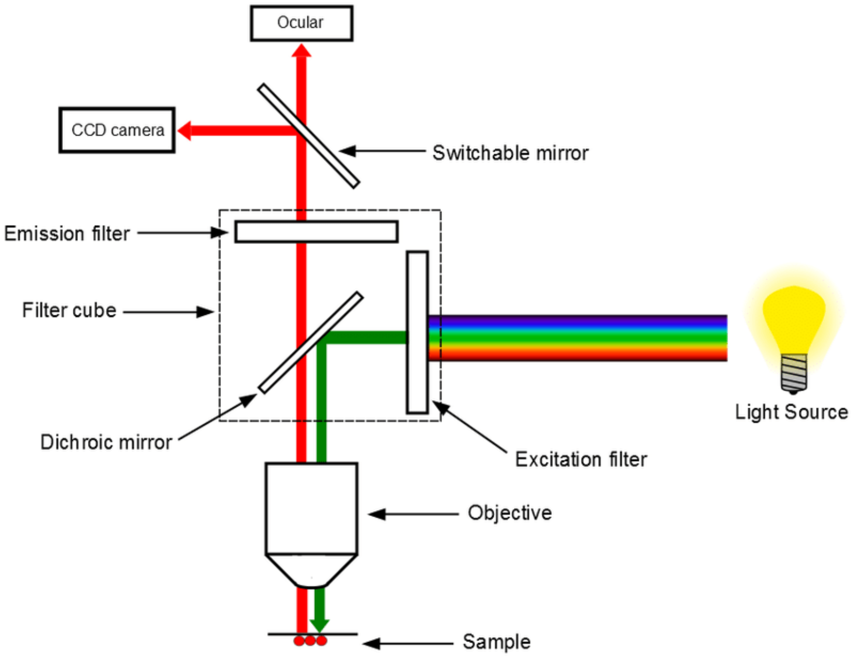

Figure 1.22: Scheme of the epifluorescence geometry inside a confocal micrsocope

by a high pressure lamp (in our case, a 130 $\frac{W}{2}$ Mercury Lamp) through a mechanical arm: through this path, light is collimated, it can be reduced in power via Neutral Density, goes through a pinhole and a diaphragm to improve respectively the dimension of the intermediate field on plane and out of plane selection. Then white light goes through the key optical element of the epifluorescence which is the fluorescence cube: the cube first selects a band of shorter wavelengths the whole white spectrum (excitation filter), then a dichroic filter placed at 45 degrees reflects the same band of wavelengths up to the sample. This band of short wavelengths excites fluorescence of the sample (longer wavelength) which is collected by the objective and again through the cube and meets the dichroic: shorter wavelengths are reflected back into the excitation path while longer excitation wavelengths are transmitted through the dichroic towards the so called emission path. Only longer wavelengths photons (sample's fluorescence) are transmitted by the dichroic, nevertheless a part of shorter excitation photons can pass through the dichroic and needs to be further cleaned by a bandpass filter which further cuts off any residual excitation and only selects the fluorescence emission.

Standard Epifluorescence with white lamp is designed to work with broad excitation and narrow emission profiles, being traditionally based on molecular fluorophores for traditional confocal microscopy; by using a laser as excitation source instead, the key optics can be slightly modified:

- First of all, there is no need for a excitation filter inside the cube because the excitation is already emitted from the diode laser and does not need to be cut out from a white lamp
- Dichroic mirror is still fundamental to bring laser up to the sample
- Emission filter can be placed outside the microscope and does not need to be a band filter, rather a longpass which simply cuts the single wavelength of the laser. This allows to measure also broader emissions and multiple emissions

Emission beam which still contains the spatial information of the surface and is corrected at infinity (ideally it means the light is perfectly collimated with no divergence until infinite). This means that we have the possibility to direct the beam to a CCD and convert the photonic spatial distribution (which preserves the reciprocal distances) and convert it into a digital photo. Because the magnification factor of the objective is 100x, the maximum and minimum achievable diameter of the beam (with lamp diaphram) can be calculated. When working in full confocal, i.e with laser spot

$$Minimum\ Spot\ Size = 1\ \mu m * 100 = 100\ \mu m \tag{1.9}$$

When using the lamp source, it is possible to cover the whole FOV of the objective so:

$$Maximum\ Spot\ Size = 180\ \mu m * 100 = 18\ mm \tag{1.10}$$

This beam contains effectively the whole information and those photons carry the whole spectroscopy.

The key idea was to send the out-coming light from the sample to the same exit; once out, send it to different detectors with filp-flop mirrors.

1. Imaging system: CCD/CMOS camera in free space, perpendicular to the beam. The focus'plane image is simply recorded by taking a picture.
2. Photo-luminescence: minispectrometer with fiber; a focusing lens is needed to couple the beam into the fiber going to the spectrometer
3. Time Resolved PL and Second order Correlation: a focusing lens is needed to couple the beam into the fiber going to the Hansbury-Twiss set up.

T-i Eclipse gives the possibility to pick different exits where to direct emitted light beam once it has passed by the last dichroic: it can either be directed to the ocular, to the left side or to the right side of the main body. Since, left exit is where the Confocal head C1 is aligned I decided to use the right exit and mount all the optics to the right.

In figure 1.23, it is illustrated the first basic geometry of this set-up. The epifluorescent arm with the lamp case (black) mounted serves are excitation path, the signal comes out from the right low exit and is directed either to a lens that focus light to a orange fiber to bring to chosen detector line or to a digital camera by the means of a flip flop mirror.

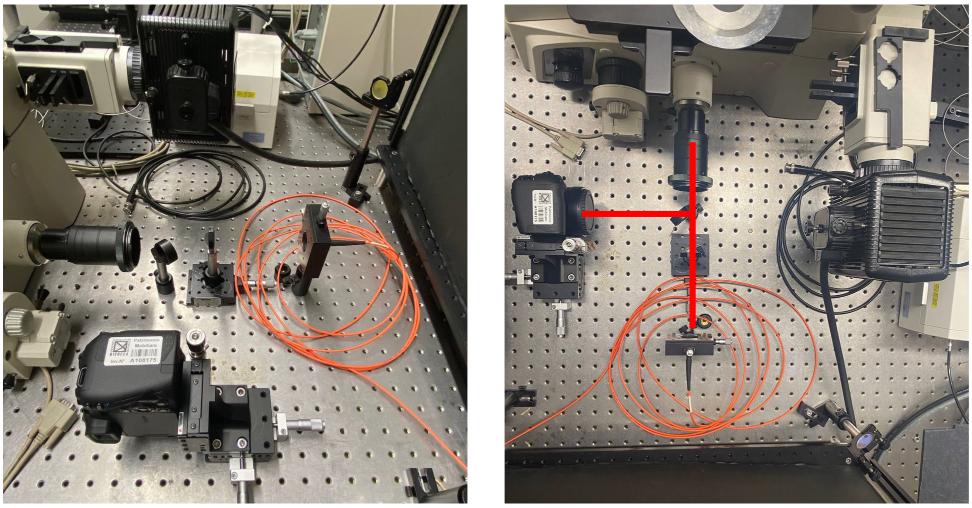

Figure 1.23: Side and upright vision of the first elementary geometry of the new set-up geometry. In red, the simulation of the exit beam, deviated by the flip flop mirror

For imaging, as CCD camera, we chose an EOS RP Canon Camera; this type of camera is very compact (Mirrorless technology) and has the possibility to work in very low illumination levels. This specific model of camera has been chosen because of its very high ISO value, which represent the electrical gain that can be applied to each pixel to amplify the signal; for this kind of sensor, it is one of the highest available. This feature is a key for our application because of such low signal regime. Moreover, for this model it is possible to overcome the limit of 30 second exposition, which is the maximum exposure value for common digital cameras. Finally, digital camera has its own processing software and remote control to directly communicate via Wifi.

It is important to note that with this new geometry, we cannot raster scan the area of the sample anymore but only collect an area as large as the dimension of the excitation source. For lasers, this means we can only collect the image of the spot which is generally 10 x 2μm for a typical picosecond diode laser available in our labs; this area is very small and makes it hard to have a good evaluation of the particle distribution on the surface.

Lasers generally do not have a beam as big as the FOV of a 100x objective (200 μm circa), this is way raster scan are used with such source to cover a wide area; but, for this geometry, laser goes through the same path as the epifluorescent lamp, and a lamp can cover a much bigger area because it is designed to work filling the whole field area of the objective.

To compensate the loss of the raster scan, we can then use the huge FOV accessible with the lamp illuminator to visualize a wide fluorescence area (up to 180 μm) on the camera and have a good estimation of the sample's distribution on particles. Then, once a good exploration of the sample is made, it is possible to dismount the lamp from the epilluminator and just use the laser spot to excite the particles.

Due to geometrical reasons it is not possible to do the complete imaging and the laser confocal at the same time, as they use the same optical path. We can switch from one to the other buy mounting or dismounting the lamp box depending on which information we want to collect.

1.4.1. Optimization of new set-up: challenges and limitations

The new system also presented some challenges to overcome in order to take good quality measurements.

First of all, the whole light processing is now in open space. Compared to Confocal C1 which was sealed in a box for maximum dark, now that external ambient light can end up on the detectors and severely increase the white noise. The most critical sensor to isolate is the CMOS sensor which is very big (35,9 x 24 mm) and whose solid angle can capture stray-light from the room. I designed a optical box to isolate the system and avoid any light leak but with the possibility of easly mount-dismount to access any optic.

The reduced image size

Another important change of this set up is the size of the image sent to the APDs. In fact, with the use of confocal head, the optics would work best coupling the light in a fiber with 1 mm core. This would lead to a beam diameter of 1 mm to go within the Hansbury Set-up and the beam would have to be reduce to a 100 μm spot to use the active area of the APD in the best possible way. With a magnification ratio 1:10, a substantial amount of spherical aberrations are introduced in the system due to spherical lenses having to be chosen with a big curvature radius to achieve such strong focusing. With this new geometry, we have no limitation to the fiber core selection as we can focus light in the fiber which works best.

The guiding principle is: the smaller the fiber core, the smaller the final spot we can focus on the detectors without modifying the magnification factor and so introducing the least amount of aberrations. Because the total active area of APDs is 100μm, the perfect choice is a fiber with such core's diameter. Being designed with a image size 10 times smaller and a completely different NA of the fiber, the whole optics within the APD box has to be re adapted to fully couple with the new fiber optics. To achieve a 1:1 ratio between object and image size, the optical requirement is NA of all lenses and fiber have to match. NA's value is determined by the initial point source, which is the fiber in our case. The 100 μm core fiber used has a 0.22 NA, and this requirement is going to be applied in the choice of the lenses. NA equation can be written as follows to express the direct dependence on the geometrical characteristics of the lens:

$$NA = \frac{D}{2 * \ f} \tag{1.11}$$

Where D is diameter pupil, f is the focal length.

Because the focus length is limited by geometric co-strains due to the dimensions of the detector box, diameter of all the lenses had to be divided by 2 to compensate and reach the goal. The whole set up has been adjusted to half inch diameters lens and properly realigned. The result was a finely focused spot in the central pixel of the APD, and the improvement of such alignment was seen by the steeper increase of counts from 0 to maximum when the precision micrometer screws where moved around the optimum.

Parasitic reflections of breakdown emission

Such improvement of alignment revealed an unexpected unwanted effect. We observed narrow intense peaks in the $g^{(2)}$ function at very low delay times; this strange signal was always present, both with the sample and without, its intensity was proportional to the total counts, it will always occur at the same time delay and with the same shape (see figure 1.24).

Initially, we guessed it was some kind of electrical cross talk correlation between the detectors or the BNC cables. Even when we moved all electronics as far as possible nothing changed. We concluded that this parasitic signal had to have an optical origin, but not related to light from the sample as it was also measured in condition of only ambient light. Every photon would trigger this start and stop process, two times so we concluded that it had to be somehow related to unwanted reflections. Moreover, we tested that the appearance of the second peak would be related to the length of the fiber.

Finally we concluded that those photons were emitted by the APD themselves; in fact,

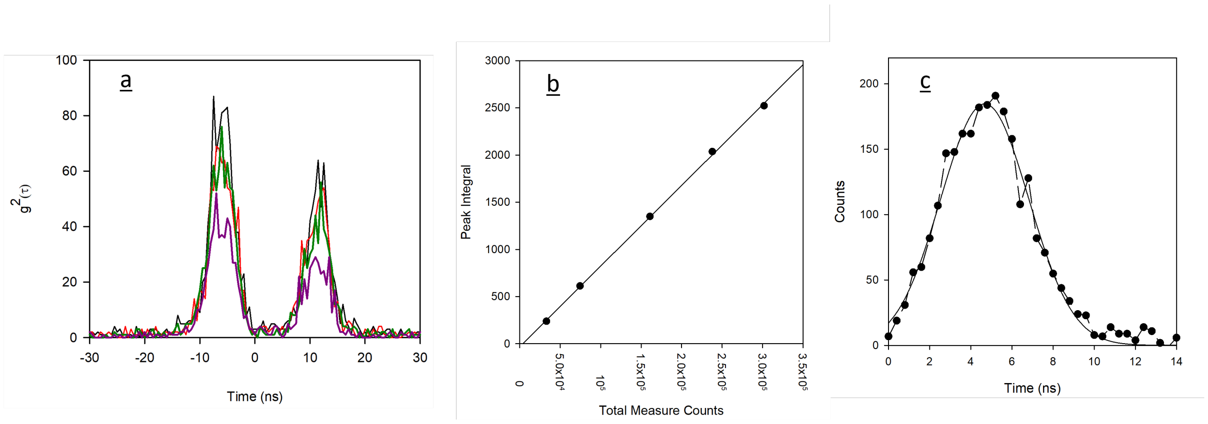

Figure 1.24: Parasitic reflections measured on APDs. a) g^2 measured several times in ambient light conditions and no samples. The effect measured is perfectly identical each time b) Perfect correlation between total intensity counts and integral of the peaks, showing how the effect simply scales with light intensity c) Poissonian fit of one of the peaks.

when working near the breakdown voltage, the avalanche process would result in the movement of a huge number of hot carriers diffusing through the junction and the movement of those charges resulted in emitted photons. This effect has been previously observed in literature and characterized [25, 26]. Their energy is spread over the visible range of the spectrum and some of the Near Infrared. Because of such fine alignment, those photons are collected by the focusing lens in front of the sensor and collimate them back to the beam splitter and all possible reflections can be brought to the other APD, which measures them as stop signal by the counter. Those photons are randomly polarized so when we put orthogonal polarizers on the respective lenses one detector would not receive photons of the other; this was the experimental proof of the origin of such signal. Even though this method allowed us to understand the nature of the process, it is overall very ineffective to use it permanently, because in an experiment it would constantly cut-off half of the sample signal.

To reduce such problem, we tried another strategy, which consisted in reducing to the minimum possible the reflection of those photons; this way, only parasitic signal is reduced without affecting in any way the reflection occurs on every optical glass plane perpendicular to the beam reflects 4% of incident light, this includes lenses which are piano convex and the fiber exit termination.

We changed then all the optics with suitable changes in order to minimize this effect.

1. All the lenses within the box have been substituted with the same optical power but with an anti-reflective coating over the largest range overlapping the breakdown

spectrum.

2. The Fiber has been changed with a cut surface in order to direct the reflected photons out of the solid angle in which the lens collect light. The 8° pre-angled ferrule reduces back reflections in low-NA fibers, which leads to an improvement in return loss.

This improvements overall reduced completely the second reflection and by one order of magnitude the first reflection. We concluded that in this geometry it is not possible to suppress this effect completely; nevertheless, this source of disturb is constant and easy to handle with post measurement analysis because it can be decoupled from the real signal (because the total counts per time bin are additive). We wrote a easy routine that subtracts the peaks to the signal by fitting it and correlating it intensity to the calibration curve reported in figure 1.24.

A new spectrometer system

As far as the spectrometer system, with the free space beam and not the forced use of the Confocal Fiber, we could also change the fiber to perfectly match the NA of the mini-spectrometer. Previous experiments already revealed that due to the sensitivity of the detector that the signal even with the maximum amount of exposition (10 s) would be comparable with noise. So a new mini-spectrometer would be needed to detect PL over background noise.

Before doing, so we evaluated the possibility to avoid the use of fiber-connected spectrometer and focus light directly onto the slit of a self-standing monochromator with a CCD connected to it. This would avoid the loss and distortion of signal due to fiber coupling, does not limit the use of a specific fiber, allows the user to change both grating and slit aperture to obtain the desired spectral resolution, to move from 0 order to 1st order to do both imaging and spectroscopy. Moreover, the system of a monochromator and a sensor as separate units gives us much more freedom with the choice of the latter to our desired performance.

In our lab, we had an unused Triax 190 monochromator with a basic controller that access only the step motors for slit aperture and the grating angle. The software cannot control the calibration because it does not put sensor and monochromator in communication, but we used it as a starting point to verify the efficiency of such arrangement. Calibration to convert pixel to wavelength has to be performed each time the position is changed; but for our means, the expected emission for each nanoparticle to be studied is very narrow and the possible shift is always in the order of magnitude of maximum tens of nanometers.

Once we fixed a central wavelength, the grating does not need to be moved. We pick a combination of grating + sensor size so that we can have a sufficient span on nanometers to measure enough.

With a new spectrometer in open space we have to focus the beam in the middle of the aperture slits; also in this case, to optimize the signal quality, we have to chose a lens that matches as much as possible the numerical aperture of the monochromator optics; the TRIAX 190 spectrometer has a numerical aperture equal to 0.128, and using equation 1.11, we can derive what are the geometrical characteristics of the lens.

In doing so, we need to consider the effective beam diameter, not the lens nominal pupil diameter value to have a valid calculation; we have to make the calculation on the highest possible beam diameter, as for smaller diameter beam we would have a certain magnification factor which will slightly reduce the signal. On our case the approximate value of the maximum spot size with the diaphram in is maximum 25 μn with the lamp imaging system; as a out coming beam diameter we have 25 * 100 = 25 mm; we take into consideration the divergence of the beam to approximate it to 30 μm. Using equation with NA of Triax and the effective beam size of 3 mm, we obtained a focus of 12 mm.

To achieve such small focus, the design becomes very critical as well because this focusing lens has to be placed almost in contact with the slit and this means:

1. It does not have to prevent movement of the step motor engines that push on the spring.
2. The cannot be placed below the lens because it is occupied by the mechanics, so it has to slide in the cover in a lens tube and the fine mechanical movement have to be controlled by a transnational mount where the tube is mounted.

For this reasons we mounted it on a tube lens which could be controlled by translation stages outside of the slit cage. Once optimized focus on the slit is achieved, we move to the choice of the sensor to image the spot.

The ideal spectrometer's sensor for SPS has to have the following requirments

1. The lowest thermal noise possible. This can be suppressed with a cooling system such as Peltier.
2. High sensitivity and high gain. This depends on the quality of the sensor itself and its electronics
3. The possibility to select the longest exposition time (possibly up to 30 minutes) without saturating the memory or crashing the elaboration.

4. A small Pixel dimension in order to have the best spatial resolution
5. Be programmable to perform routines that can be fully customized via software

The search for sensors with such performances lead us to Astronomic Cameras. Observation of Single particles and Far away stars are in fact very much similar in terms of intensity over background ratio. After understanding if these kind of cameras could fit into the exit ports of the Triax Monochromator, we selected a CMOS ZWO Camera 294MM with Peltier Cooling. This camera has much better performances compared to Hamamatsu in term of background noise and quantum efficiency.

The main improvement is in the geometry of the sensor, which for Zwo is a back illuminated CMOS: this image sensor improves the sensitivity and noise reduction - the key factors to enhancing image quality. It does this by radically realigning the fundamental pixel structure from front-illumination to back-illumination, while still retaining the advantages of CMOS image sensors such as low power consumption and high-speed operation.

With a conventional front-illumination structure, the metal wiring and transistors on the surface of the silicon substrate that form the sensor's light-sensitive area (photo-diode), impede photon-gathering carried out by the on-chip lens. A back-illuminated structure minimizes the degradation of sensitivity to the optical angle response, while also increasing the amount of light that enters each pixel due to the lack of obstacles such as metal wiring and transistors. These components have been moved to the back-side of the silicon substrate. Together with the cooling architecture, it increased the quantum efficiency by 20%.

The installation of such camera required the 3D Printing of a an auxiliary custom piece to embed the camera on the exit of Triax with the possibility to slightly move and tilt the sensor to find the optimum. This has to be done because Triax monochromators are designed to host specific sensor whose geometry is different from the astronomic cameras of our use.

Finally, the use of a monochromator becomes very useful because it is possible to select the wavelength range to send to the APDs. This opens the possibility to perform spectrally-resolved and time-resolved measurement if needed. Triax 190 has a double exit, so while one is used for spectrum, the other one can be used for Time-resolved. I used a doublet of lenses to couple the dispersed focus light again within a fiber, so that the it can be brought if needed into the Hansbury-Twiss.

Final geometry

Finally the whole set-up was put together as reported in schematics in figure 1.25 and in real space in figure 1.26.

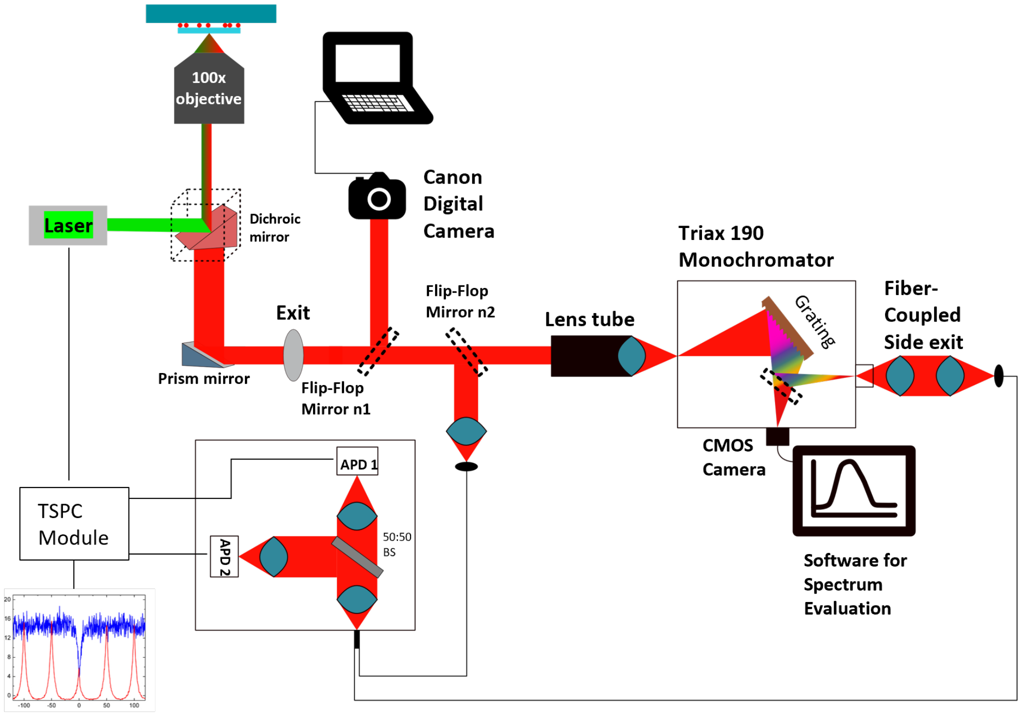

Figure 1.25: Schematics of the set-up total geometry, from Green Laser excitation to Red PL various analysis

The signal goes out from the microscope and two broadband dielectric mirrors are placed at 45 degrees on magnetic flip-flops mount.

1. When Imaging, Mirror 1 is down and beam goes to the Canon Camera
2. When TRPL, Blinking and correlation, Mirror 1 is up and Mirror 2 is down and beam goes to focusing lens to fiber to the APD box.
3. When PL spectrum, all mirrors are up, and beam goes into focusing lens to Triax to CMOS .

One of the disadvantages of such geometry is the focus criticality: the out coming beam is not perfectly collimated, this means that focus has to be finely adjusted depending on the distance between the objective and the detector. With such geometry that splits light

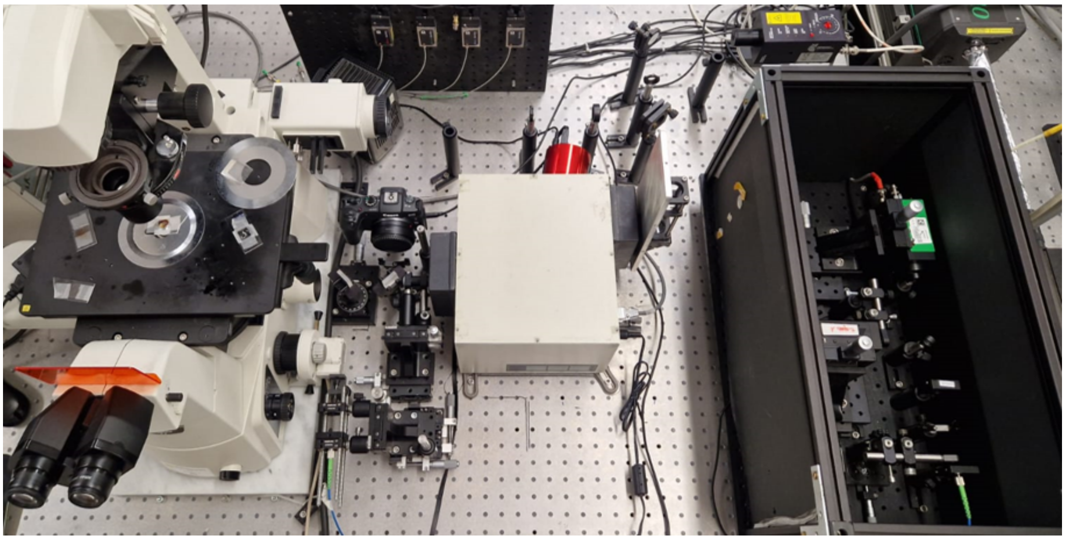

Figure 1.26: Real Geometry of the Set-up. In the closed black box is the Hansbury-Twiss interferometer

in three different paths, each beam line potentially has a different focus which needs to be adjusted each time we switch from one detector to the next.

We tried to optimize this difference by measuring the length of each path on the optical table and, compatibly with the geometrical restrictions, placing the optomechanics in the position where those distances are the most similar possible. Then, for fine adjustments, we first focused the beam on the last detector (Triax 190) which has no possibility to be translated and moved the other two collection systems' stages with micrometer screws in order to spatially find the position where beam is focus along each path. In the next section I will present the results we obtained with this geometry.

1.4.2. Results with new geometry

In this section I will report the most significative results on NPs obtained with such geometry; sample preparation recipe is the same used with previous set-up.

In figure, I reported the far field images recorded with the canon Camera of the sample's surface with nanoplatlets dispersed on top of it. Progressive dilution until the red spots are far distanced enough. The photos are taken in excitation condition so that repetition rate is the highest and energy per pulse is kept low, the exposition is 10 seconds and the ISO (amplification) is the highest possible.

All measurements reported have been performed with a Picosecond Pulsed Diode Laser with wavelength 510 nm and modifiable repetition rate down to 50 MHz. Dichroic mirror

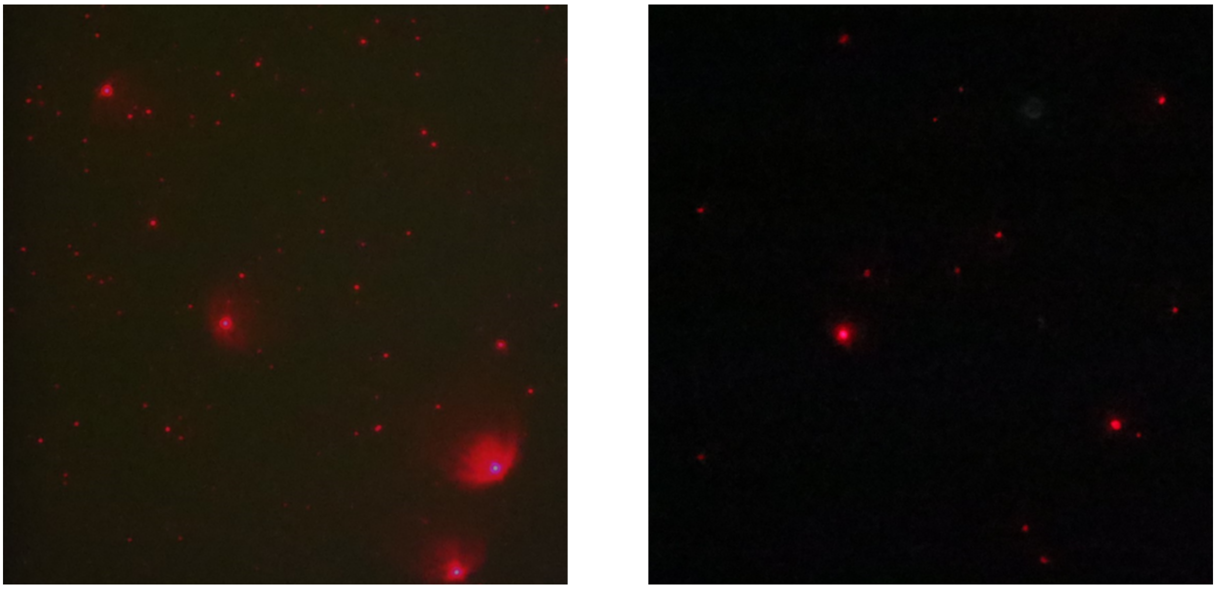

Figure 1.27: Far field images of the focal plane where the NPs are dispersed. Left: more concentrated. Right: more diluted starting solution

has a reflection band spanning from 450 nm to 590 nm, and transmission band from 605 nm to 800 nm. Excitation power is set in order to have a maximum probability to generate a certain number of excitons per laser pulse per dot.

It is possible to set the required laser power for a specific repetition rate by knowing the absorption cross section of the system. As a starting point, we used a reasonable value taken from literature [27].

The equation to calculate the number of excitons is the following:

$$< n >= \frac{P}{E_{ph} f A_s} \sigma_{abs} \tag{1.12}$$

where P is the measured incident power, E is the energy of the photons, A is the spot area, f is the frequency of the excitation, and σ is the cross-section.

Finally, detection line is the one described in details in the previous section. PL spectra have been recorded with integration time up to 10 minutes. T2 and T3 from which blinking, second order correlation $g^{(2)}$ and FLID have been reported have been performed for 10 minutes of total accumulation.

In figure 1.28 and 1.29, we report the most meaningful measures on a single particle at single exciton fluence.

As a proof of single particle measure, we clearly see that $g^{(2)}$ function at zero delay is

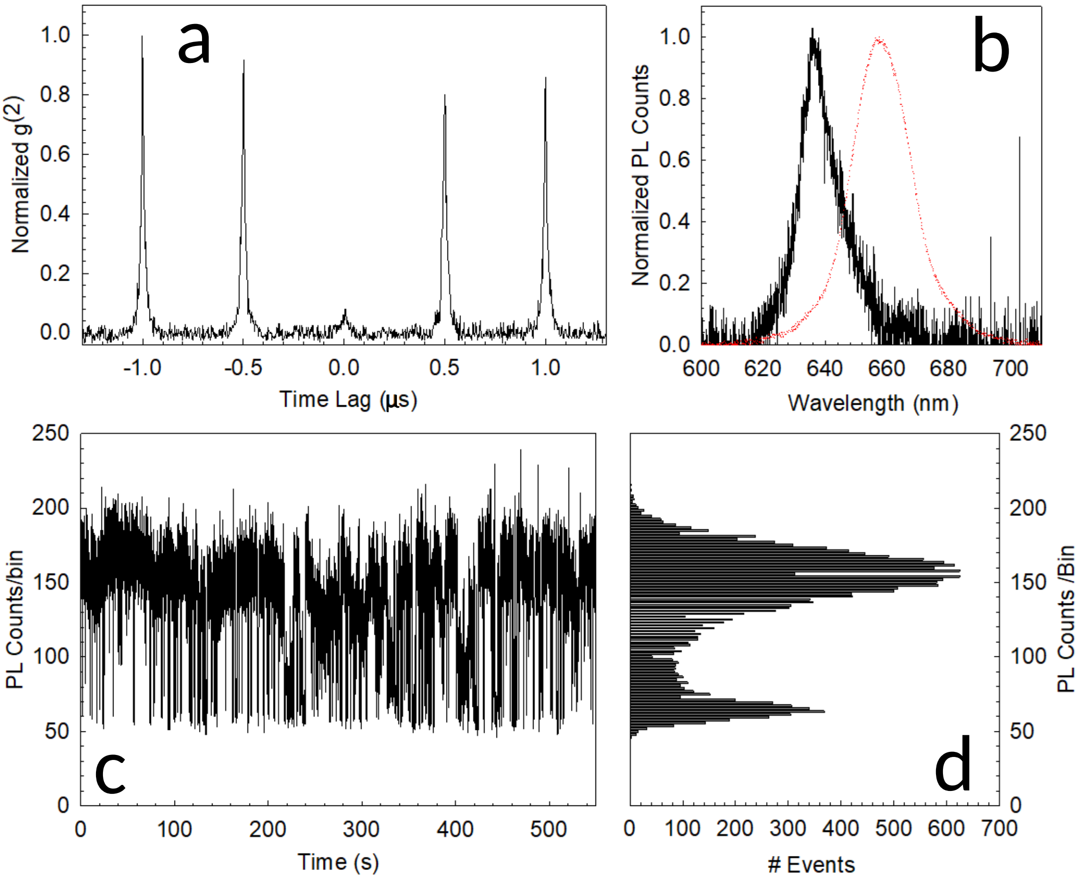

Figure 1.28: Single Particle T2 Measurement in single exciton regime. a) Measured $g^{(2)}$ function b) PL spectrum of the particle in black, PL spectrum of the ensemble in dotted red c) PL trajectory showing blinking behaviour d) Histogram of events with assigned counts/bin

very different from the adjacent peaks (1.28a). If we integrate the area below the first adjacent peaks and the 0 peak, then divide them, we obtain a ratio of 0.08. This value is considered low enough to label our particle as single;

PL spectrum in 1.28b shows a peak at 640 nm which is visibly narrower compared to the ensemble PL (dotted in red), with FWHM = 14nm compared to 22 nm of ensemble PL measured with the same experimental conditions (same excitation and detection set-up). The maximum position is slightly blue shifted (20 nm) but we do not have enough statistics to predict weather this shift is related to a single particle systematic shift or we have just measured prominently smaller NPs; smaller NPs in fact are known to have lower $g^{(2)}(0)$ and higher energy PL peaks [28] [29]. In any case, with this measurement we can speculate that there is a broadening of the PL in the ensemble, reasonably ascribable to size dispersion of the NPs. We demonstrate that we can overcome this with our SPS measurements.

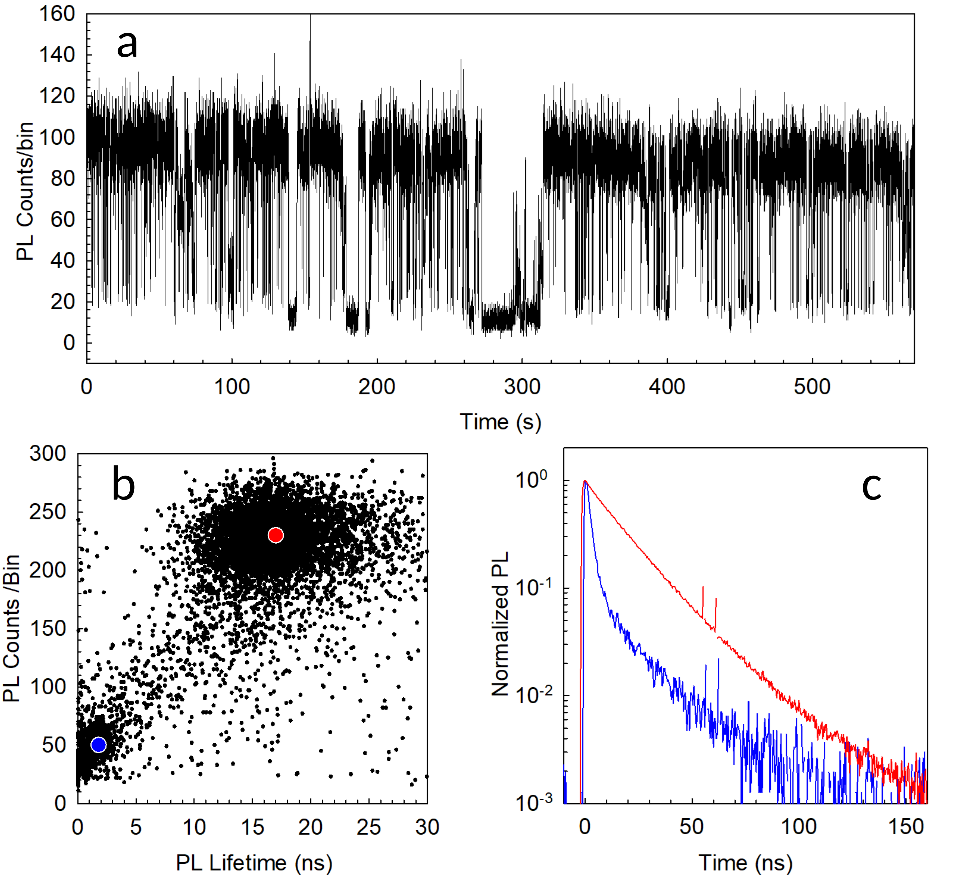

Figure 1.29: Single Particle T3 Measurement in single exciton regime. a) Blinking trace b) FLID; c) Lifetimes extracted at different count levels: blue curve is taken at blue point, red curve at red point in FLID

On the PL trace vs time (1.28c), we clearly observe an ON-OFF behaviour, tested by two distinct peaks in the histogram of events (1.28d). ON events clearly dominate over the OFF events: for this particle, we can estimate the particle being ON circa 80% of total 10 minutes measure time. This information is crucial as it changes the effective total PLQY in ensemble, but is only measurable at single particle level.

We measured the lifetime as a function of the counts to understand the dynamics of the ON and OFF states (T3 mode). The result is reported in figure 1.29. If we look at the Fluorescence Lifetime Intensity Distribution (FLID), we clearly see two distinct populations: for high counts (ON states, around red spot) higher lifetimes, for low counts (OFF states, around blue spot) much lower lifetimes. This behaviour is typical of type A blinking [11]. If we plot the decays associated to the count levels, the ON states shows a perfectly mono-exponential decay for over three decays with τ= 17.9 ns (red curve). The OFF states on the other side have a very fast mono-exponential decay with τ= 2.5 ns (blue curve); the long tail is residual PL but its weight is roughly 1% of the total intensity. The ON dynamic is ascribed to exciton bright radiative recombination, while OFF fast decay is ascribed to the fast quenching of the PL due to Auger relaxation process, leading to low measured counts events.

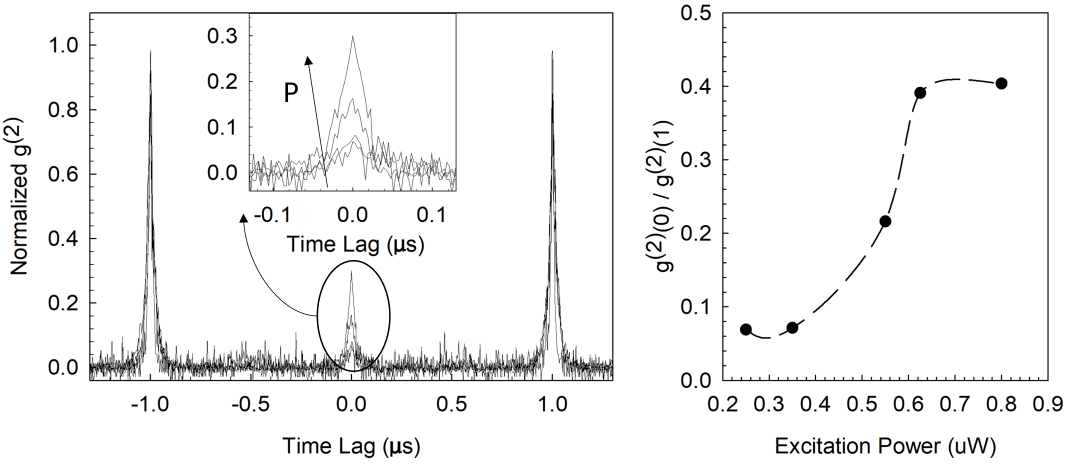

Figure 1.30: Single Particle T2 Measurement as a function of excitation power. a) $g^{(2)}$ at increasing power: the inset shows the $g^{(2)}(0)$ increasing with increasing power P. c) Reported value of $g^{(2)}(0)$ / $g^{(2)}(adjacent\ peaks)$ as a function of power, leading to a sigmoid experimental function.

When we raise the excitation power to allow the formation of biexcitons, we observe a raise of the $g^{(2)}$ signal at 0 delay, due to radiative decays of biexcitons (figure 1.30). When we plot the $g^{(2)}(0)/g^{(2)}(adjacent\ peaks)$ ratio as a function of power, we observe a sigmoid curve going to saturation over a certain power. The offset of the sigmoid represent the power at which the probability of forming more than one exciton becomes different from 0. This is a good experimental value to estimate the absorption cross section for $< n >= 1$. When the ratio goes to plateau at high fluence, its final value is correlated with the biexciton PLQY. Such measurement is indeed very important for fundamental spectroscopic characterization of a luminescent nanoparticle.

Morover, if we analyze PL trace in such multi-exciton regime (fig. 1.31a), we appreciate an increase of the the OFF states occurrences, compatible with the higher probability of Auger in multiexcitonic regime.

If we look at the histogram of events we do not see a neat division between a ON level

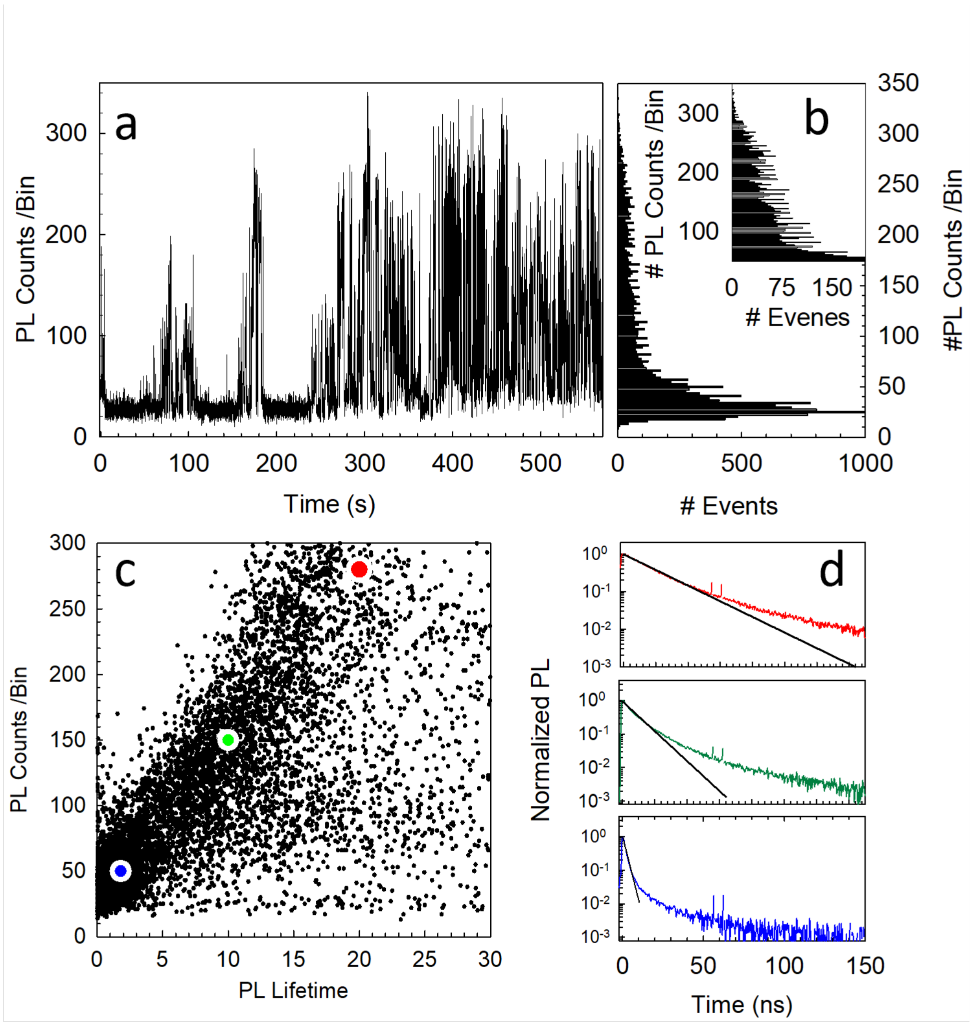

Figure 1.31: Single Particle T3 Measurement in multiple exciton regime: a) Blinking trace and b) its histogram ; c) FLID d) Lifetimes extracted at different count levels: blue curve is taken at blue point, red curve at red point, and green curve at green point in FLID

of intensity and a OFF level of intensity as in single exciton but an apparent spread of values of counts for the ON states. A closer analysis at the histogram reveals two main populations, the highest count and intermediate intensity level (fig. 1.31b and inset). When we correlate such counts to their lifetime in the FLID diagram (fig. 1.31c), we also observe, that compared to single exciton regime, we do not have a clear distinction of two populations but rather a spread of different intensity events with an almost continuum of lifetimes associated.

The highest counts have the same τ of single exciton measured at low fluence (18 ns)(red curve/point) but shape is not neatly mono-exponential as before; the intermediate counts level has a τ value which is circa half the single exciton, ~10ns (green curve/point). This change of dynamic is then ascribed to the presence of biexcitons, which lead to acceleration of the decay: this claim is also consistent with the biexitonic PLQY being roughly half of PLQY of the exciton PLQY for such systems. This explains very well why those events around green point have circa half intensity then single exciton (around red point). OFF events have exactly the same intensity and lifetime as before (blue curve), but much higher occurrence due to increased probability of Auger quenching when increasing the probability of biexciton formation.

Our characterization on single particles NPs is very consistent with typical single particle results; it proves how many useful and unique information we can obtain on the system with our detection and analysis methods, but mostly the potential of such system for advanced spectroscopic investigations.

Among the distinctive single particles with clear $g^{(2)}(0) << 0.2\ g^{(2)}(t)$ (condition commonly used in literature for single particle labelling) , a lot of particles have also been measured with $g^{(2)}(0)$ different from 1, spanning from 0.3 to 0.6. Given this, those objects are plausibly composed by a number of particles close to one; another possibility is that those are measures on individual isolated NPs but antibunching is not measured for most of them because of their physical properties; possibly, even when the single nanocrystals are isolated, their photon purity is not good enough to consider them single photon emitters. This hypothesis is corroborated by the fact that $g^{(2)}(0) << 0.2$ measurement previously reported are very few compared to these with $g^{(2)}(0) > 0.3$, which could agree with the fact that only few particles in the considered ensemble are small enough to show antibunching; most of them are simply too big and should not show such property. We can conclude that, statistically, even if we are in the presence of a single NPs, the probability of $g^{(2)}(0) << 0.2$ might be extremely low because only a very small fraction of the NPs have such property. So, those $g^{(2)}(0) > 0.3$ might be as well single particle, but their single photon purity might be simply not high enough and $g^{(2)}$ function not a good discriminator between single and clusters. Further work has to be carried out to understand this phenomenology.

As a explanatory example, we report in figure 1.32 the complete set for one of those measurements where strong antibunching was not measured. $g^{(2)}$ ratio at 0 lag and after the first pulse is 0.5 (1.32a) and blinking shows less discreet ON/OFF levels also in the histogram (1.32c-d). When we take a look at FLID (1.32e), we see that the lifetime distribution is a continuum of values from ON to OFF events; decay time and shape might be affected by the presence of multiple particles surrounding the emitting one, resulting in a longer-highly stretched lifetimes compared to the single particle measurements at all intensity levels. Three representative points are reported to show such effect (1.32f).

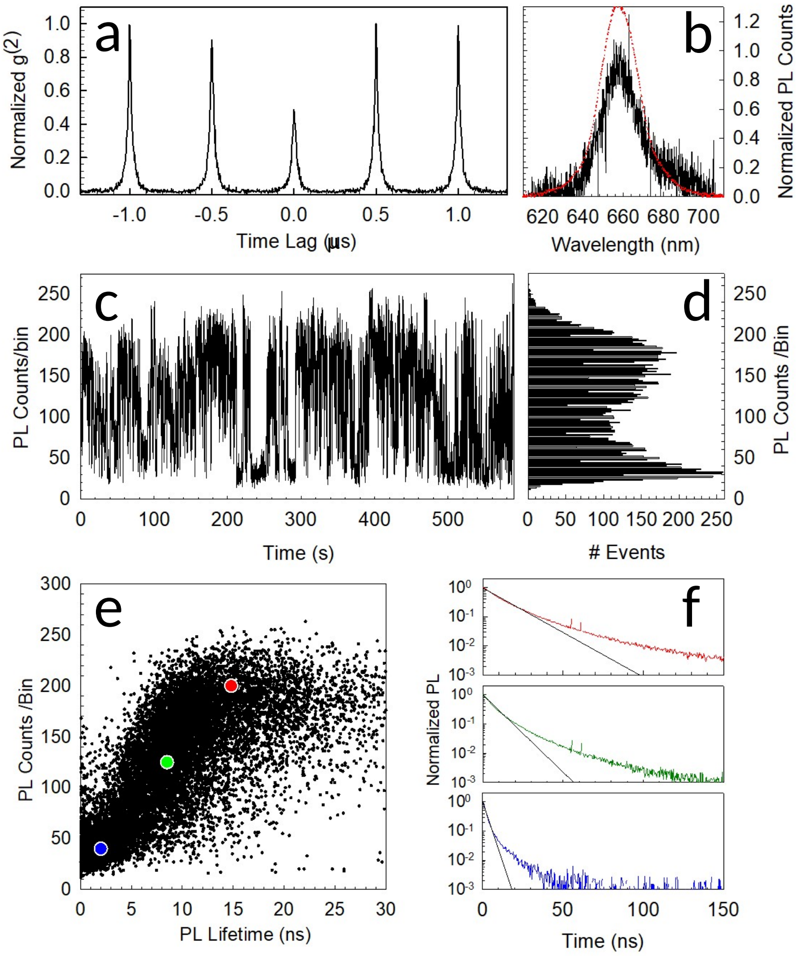

Figure 1.32: Multiple Particle T2/T3 Measurements. a) $g^{(2)}$ b) PL spectrum of the particle in black, PL spectrum of the ensemble in dotted red c) PL trajectory showing blinking behaviour d) Histogram of events with assigned Counts/bin e) FLID f) Different lifetimes extracted from FLID with the same colour label as before.

We measured PL of those $g^{(2)}$=0.5 emitting points and reported them in figure 1.33. It is possible to see a good distribution of maxima within the ensamble peak, but those peaks have all comparable width to the ensamble and among them, which is in agreement with literature on single NPs luminescence [30].

1.4.3. Conclusions and future work

We demonstrated that the new geometry for the SPS set-up allowed us to measure single particles' fluorescence efficiently on CdSe/CdZnS NPs, giving results which are comparable to literature data; optimization can be expanded even more: first, with a illumination

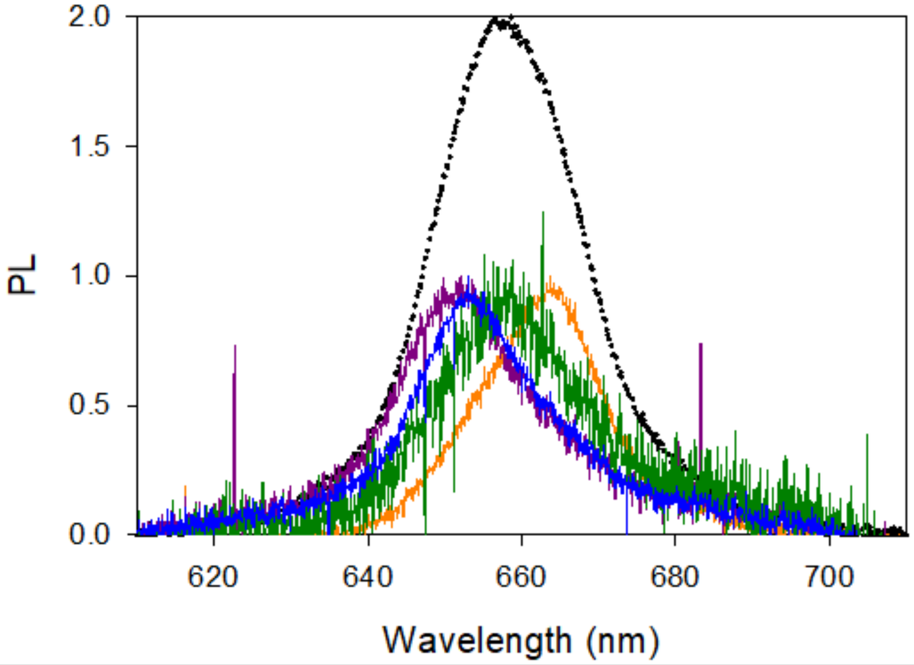

Figure 1.33: PL spectra of different multiparticles compared with the ensemble one (black curve)

system able to switch from confocal to wider far-field imaging without switching from lamp to laser continuously; secondly, with a more precise mechanical stage to increase the accuracy of the alignment. Optical detection and analysis tools of the detected phonons allowed us to access with state-of-art resolution, accuracy and precision the key single-particle properties to speculate about advanced photophysics only accessible in individual nanocrystals. Finally, the new geometry gives complete freedom to adjust both excitation path and detection line to the desired application without losing efficiency in any area of the UV/VIS/NIR spectrum; this will give us the possibility to extend its use to the study of any novel system without limitations.

2 | Cutting-edge designs of Lead Halides Perovskites-based nanostructures

Following the discussion on how we managed to develop a key characterization technique for advanced NPs design, in this chapter I will discuss some of the those innovative nanocrystal design that have been developed and studied in collaboration with different international groups. First, in section 2.1, a new synthetic route has allowed us to produce stable highly confined lead halide perovskite (LHP) $CsPbBr_3$ *which exhibit distinct quantum confinement effect on the optical properties, that are rarely observed due to low stability of such small crystals Then in section 2.2 I will go through the topic of realizing efficient heterostructures based on LHP, a challenge that has been tackled in this field for years and has still not been reached. Finally in section 2.3, following from this last topic, I will discuss a interesting work which focus on the use of such heterostructures to access thermodinamically unfavourited phases by using LHP as epitaxial templates.*

2.1. Confined PVK: from the chemical challenge to the optical properties

The research for highly confined LHP has been very limited by stability in solution due to uneffective ligand passivation; various works have shown that their surface passivation, via a proper choice of surfactants, plays a fundamental role [31, 32] Aliphatic amines and carboxylic acids (most often oleylamine and oleic acid) are the standard ligands employed in the synthesis of these NCs, eventually passivating their surface as charged species (as ammonium and carboxylate ions, respectively). Various studies have demonstrated that a simple variation of the local pH, which can cause protonation/deprotonation of carboxylate/ oleylammonium ions, or even a dilution of the NC suspension, which decreases the chemical potential of the free ligands with respect to that of bound ones, can lead to ligands detachment, which is deleterious for both colloidal stability and PL[31, 33]. Conse-

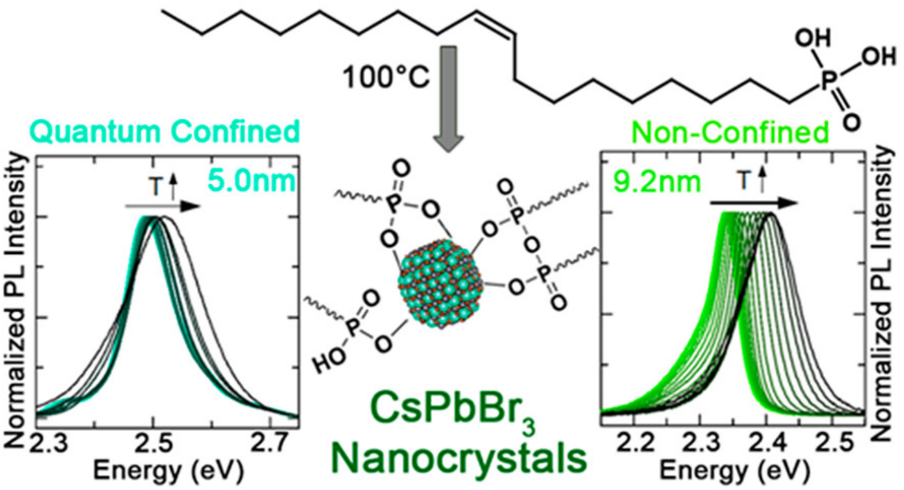

Figure 2.1: Optical properties for confined e for non-confined $CsPbBr_3$

quently, these types of ligands are weakly bound to the NCs surface, and a highly dynamic equilibrium exists between free and bound ligands[31, 34, 35]. In order to optimize the surface passivation of LHP NCs, various alternative surfactants have been investigated, with zwitterionic molecules, quaternary alkyl ammonium ions, and sulfonic and alkyl phosphonic acids being the most promising ones [31, 33, 36–38]. The improved stability in these cases arises from the fact that either they cannot be deprotonated (zwitterionic molecules, quaternary alkylammonium ions), or they have a strong affinity toward surface Pb^{2+} ions (sulfonic and phosphonic acids). As a result, all these ligands yield LHP NCs with higher stability and near-unity PL quantum yield (QY). In a recent work from our group, we demonstrated that $CsPbBr_3$ NCs, synthesized in the presence of alkyl phosphonic acids as the only ligands in the reaction environment, are very stable against dilution, maintaining ∼100% PLQY even at concentrations as low as 1 nM. These NCs were found to be coated by hydrogen phosphonate and phosphonic acid anhydride molecules, the latter formed in situ, during the NCs' synthesis. In these NCs, we could observe ligand desorption under an inert atmosphere, in the form of Pbphosphonates, only when heating the NCs dispersions at temperatures of 50 °C or above[33]. Such stability stems from the strong binding affinity of the alkyl phosphonate species to Pb^{2+} cations at ambient temperature. On the other hand, that synthesis approach had two major limitations: (i) the NC dispersions turned out to be unstable in air; (ii) the phosphonic acids employed (namely tetradecyl- and octadecylphosphonic acids) require high temperatures (at least 220 °C or above) to solubilize the metal cation precursors and this prevented the synthesis of small NCs [33]. As a matter of fact, with that method we could not grow NCs with sizes smaller than 7 nm. To overcome these issues, we have developed a synthesis of $CsPbBr_3$ NCs that employs oleylphosphonic acid (OLPA) as the sole surfactant present in the reaction environment. The good solubility of OLPA in common apolar solvents allows for the solubilization of metal cation precursors at low temperatures (as low as 80 °C) which, in turn, enable the synthesis of $CsPbBr_3$ NCs with a good control over their mean size down to 5.0 nm (figure 2.2), thus accessing the strong quantum confinement regime (the exciton Bohr diameter of $CsPbBr_3$ is 7 nm) [39, 40].

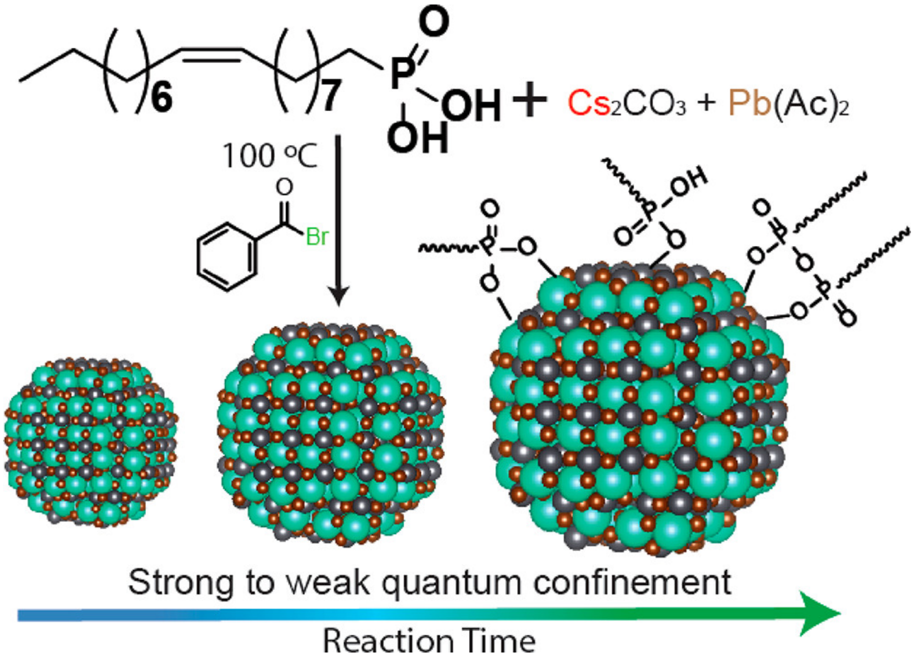

Figure 2.2: Colloidal Synthesis of $CsPbBr_3$ NCs Employing Oleylphosphonic Acid

OLPA-based $CsPbBr_3$ NCs, which are passivated by hydrogen phosphonates, phosphonic acid anhydrides, and phosphonate species (figure 2.2), exhibit excellent colloidal stability even when exposed to air and at extremely low concentration (1 nM), with no need to avoid cleaning procedures or to perform postsynthesis ligand exchange treatments aimed at preventing size evolution, as done in previous works in which small $CsPbBr_3$ NCs were prepared and studied optically[40, 41]. Our PL measurements evidenced that quantum confined NCs feature highly efficient, blue-shifted emission with respect to bulk $CsPbBr_3$, and their kinetics slows down dramatically at cryogenic temperature, with no concomitant change of the PLQY. This radiative effect is markedly different from the accelerated decay with decreasing temperature commonly observed for larger NCs, which is ascribed to the presence of a bright triplet lowest excitonic state [42] and suggests an exciton fine structure featuring a low energy dark state in thermal equilibrium with a higher-lying bright state, in agreement with recent works[41]. The $CsPbBr_3$ NCs of this work were prepared by modifying the colloidal approach that we recently reported [33]. In the present case, we synthesized OLPA and used it as the only surfactant to drastically reduce the temperature at which the metal cation precursors (Cs_2CO_3 and $Pb(ac)_2$) could be dissolved in octadecene (ODE). As a comparison, a complete dissolution (i.e., the formation of a transparent reactant solution) of metal precursors was observed only at 220 °C when working with either tetradecyl- or octadecylphosphonic acids, while in the case of OLPA this was achieved at 120 °C. Moreover, when using OLPA, the complexes that form during this step were soluble in ODE at temperatures as low as 80 °C, while those formed when employing tetradecyl- or octadecylphosphonic acids required at least 160 °C to completely dissolve [33]. This is due, most likely, to the fact that OLPA molecules are characterized by the presence of a double bond, so that intermolecular London forces are weaker and their melting points are lower than in the case of phosphonic acids with linear and saturated alkyl chains [43, 44] Three NC samples were prepared by performing the synthesis at 100 °C and varying the reaction time from 45 to 600 s. The XRD analysis confirmed that all the NC products have the expected orthorhombic $CsPbBr_3$ perovskite structure (ICSD number 98751) with no presence of impurities (Figure 2.3d).

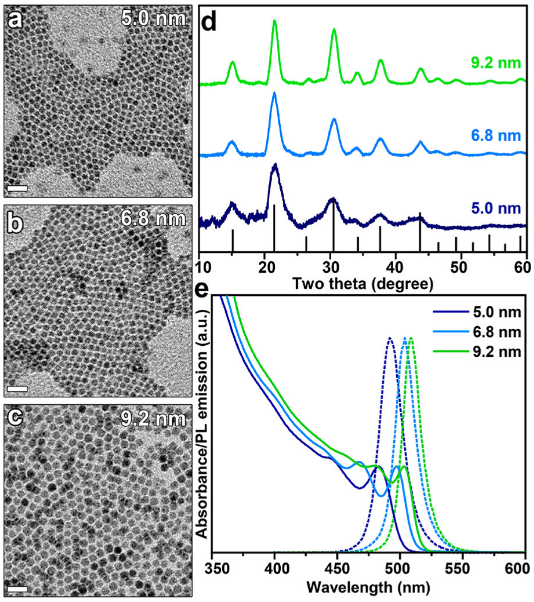

Figure 2.3: TEM images of (a) 5.0 nm, (b) 6.8 nm, and (c) 9.2 nm (green) OLPA-based $CsPbBr_3$ NCs. The scale bars are 50 nm. (d) XRD patterns of OLPA-based NC samples together with the bulk reflections of the orthorhombic $CsPbBr_3$ perovskite structure (ICSD number 98751). (e) Corresponding absorption and PL emission spectra of suspensions of the same three NC samples.

The TEM images indicated that the increase in reaction time from 45 to 600 s at 100 °C enables tuning the $CsPbBr_3$ NCs size from 5.0 to 9.2 nm (figure 2.3a-c) with all the samples exhibiting a narrow size distribution. These OLPA-based NCs have a truncated octahedron shape, similarly to what we previously observed when using tetradecyl- or octadecyl- phosphonic acids in the synthesis. This shape originates from the preferential binding affinity of alkylphosphonates to both (001) and (110) Pb-terminated facets [33] As a further support to this, the XPS analysis indicated a Cs/Pb/Br/P ratio of 1/1.2/2.5/0.75, close to that measured in our previous work, which is consistent with $CsPbBr_3$ NCs having a Pb-rich surface termination, with part of Br ions being replaced by alkyl phosphonates, hydrogen phosphonates and phosphonic acid anyhdrides (ensuring charge balance). As a consequence of a broader range of accessible sizes with this method, the absorption and photoluminescence spectra of these samples can be tuned from 503 nm (PL maximum at 509 nm) in the case of 9.2 nm NCs to 482 nm (PL maximum at 491 nm) for 5.0 nm NCs (see figure 2.2e). The PLQYs of 5.0, 6.8, and 9.2 nm NCs are 91%, 84%, and 81%, respectively, indicating an efficient passivation of surface trap states. Moreover, according to our stability tests, such high PL emission was retained even when diluting the NCs dispersions down to 1-10 nM, also in the case of strongly quantum confined NCs. Such experiments highlight that OLPA-based NCs exhibit a high colloidal stability with ligands being strongly bound to the surface[31, 45]. Another important feature of OLPA-based samples is that the colloidal dispersions of NCs are stable in air up to 2 weeks (fig 2.4. This is a relevant improvement, considering that colloidal suspensions of NCs prepared with tetradecyl- or octadecylphosphonic acids are poorly stable in air: upon air exposure, the precipitation of NCs was observed together with the formation of an insoluble foam-like product. These results point to an improved stability of OLPA-based NCs, which is remarkable in the case of quantum confined ones (i.e., 5.0 nm). With the aim of explaining the improved stability of OLPAbased NCs, and, in particular, that of quantum confined NCs, and to unveil the composition of their ligand shell, we thoroughly characterized them via NMR analysis.

Both ^{1}H and ^{31}P NMR spectra of quantum confined LHP NCs evidenced the presence of P-based molecules bound to the surface of the NCs: both alkenyl protons [31, 32] at 5.3 ppm (figure 2.5a) and phosphorus signals peaks in the range 10-40 ppm (figure 2.5b) were broadened with respect to those of free OLPA ligands, an indication that these P-based molecules have a longer correlation time (τ_c) as a consequence of their binding to NCs' surface [44]. Also, the presence of multiple ^{31}P signals was a mark of a complex ligand-surface interaction, with surface molecules adopting different binding motifs with Pb^{2+} cations. To reveal how OLPA molecules were anchored to the surface of perovskite NCs, we treated our NCs with trimethylchlorosilane (TMS-Cl) and we analyzed the corresponding products via ^{31}P NMR. TMS-Cl and, in general, halides and chalcogenides (i.e., TMS-I, -Br, -Se, or -S) are known to react with phosphonate species bound to the surface of colloidal NCs delivering the corresponding TMS-substituted compounds (and leading to the precipitation of the NCs)[33, 45]. Upon reaction of OLPA-based NCs with TMS-Cl we observed

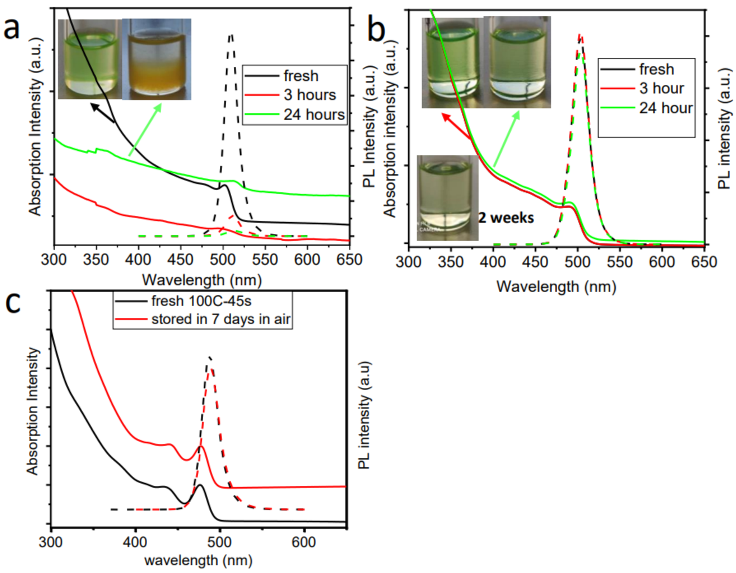

Figure 2.4: Absorption and PL emission curves of (a) TDPA $CsPbBr_3$ NC (PL peak maximum at 507 nm) and (b) OLPA CsPbBrr3 NCs (PL peak maximum 507 nm) as a function of their storage tine in air. The pictures of corresponding soluions are shown in the inset of panels (a) and(b). (c) Absorption (solid) and PL emission (dashed) curves of quantum confined $CsPbBr_3$ NCs (5 nm) before and afteri their exposure to air for 7 days

the formation of free species being characterized by four individual ^{31}P NMR peaks (figure 2.5c): one pair of sharp peaks at 14.92 and 15.52 ppm with similar intensities were assigned to O,O-bis(trimethylsilyl)- oleylphosphonic acid anhydride diastereoisomers; the peaks at 33.95 and 16.65 ppm could be ascribed to mono- and diTMS substituted OLPA species (namely, TMS hydrogen oleylphosphonic acid and O,O-bis(TMS)oleylphosphonic acid), respectively[33, 46]. Furthermore, the analysis of the 1 H NMR peaks ascribable to alkenyl protons of such species indicated a cis/trans isomer ratio of 65/35 (i.e., the portion of trans isomers slightly increased upon the synthesis; These results indicate that the surface of the NCs was passivated by different species including phosphonates (PA^{2-}), hydrogen phosphonates (PA^{-}), and phosphonic acid anhydrides [PA(anhy)] (see the sketch in 2.5b). The calculated PA^{-}/PA^{2-}/PA(anhy) ratios are 1/2.15/3.2 (that corresponds to a 1/1.02 ratio between phosphonate and anhydride species). Interestingly, PA^{2-} species were not observed in our previous work in which tetradecylphosphonic acid molecules were employed for the synthesis of LHP NCs at higher temperatures (180 °C) and where a PA^{-}/PA(anhy) ratio of 1/2.21 was detected[33]. Overall, our NMR studies suggest that low synthesis temperatures (i.e., 100 °C) promote the formation of deprotonated PA^{-} and especially PA^{2-} moieties rather than PA(anhy) ones.

Our results highlight that the reaction temperature plays a major role in dictating the binding motif of phosphonic acids on the surface of LHP and, presumably, metal halide NCs in general. On the other hand, the presence of PA^{2-} species on the surface of OLPA-based NCs is not sufficient to explain their improved stability under air. Indeed, as we previously calculated, the binding energies of PA^{2-} and PA^{-} species with surface Pb^{2+} cations are similar (47.9 and 52.2 kcal/mol, respectively). One possible explanation for the stability of OLPA-based NCs in air can be attributed to the high solubility of OLPA molecules (and anhydrides) in apolar solvents. After the exposure to air, oleyl phosphonates (and anhydrides) can be protonated by water molecules and, thus, partially released from the NC surface and solubilized by the solvent. Being still in solution they can rebind to the surface of the NCs in a dynamic fashion. Such hypothesis was supported by a control experiment in which we dispersed OLPA-based NCs into nonanhydrous $CDCl_3$, added a stoichiometric amount of OLPA molecules (9 mmol of OLPA per mmol of NCs), and analyzed the corresponding dispersions via NMR. The analyses indicate that neutral OLPA molecules are capable of dynamically binding the surface of the NCs. Conversely, phosphonic acids with linear alkyl chains (such as tetradecyl- or octadecylphosphonic acids), once protonated (again, upon exposure of the NC dispersion to air), are not soluble in apolar solvent, forming an insoluble gel hence they cannot participate to the surface passivation of the NCs anymore. In this case, the NCs become progressively deprived of surface ligands and start aggregating.

2.1.1. Quantum confinement effect on optical properties: Dark and Bright Exciton

The stability that characterizes even the small, strongly quantum confined $CsPbBr_3$ NCs that are accessible through this synthesis, with no need of postsynthesis ligand treatment [40, 41], presents us with a unique opportunity to study the optical properties of these materials in the strong confinement regime. We therefore proceeded to investigate the optical properties of both non- (9.2 nm) and quantum- (5.0 nm) confined OLPA-based NCs via side-by-side PL measurements as a function of temperature. Upon lowering the temperature, the PL spectra of both samples progressively red-shifted (Figure 2.6a,b), as expected due to bandgap renormalization,[47, 48] and their PL intensity remained essentially constant (Figure 2.6c), in agreement with the near-unity PLQY measured at RT and confirming excellent passivation of surface traps. Consistent with the smaller number of atoms involved in the thermal expansion of the perovskite crystal lattice upon lowering the temperature, the red shift of the PL maximum was less pronounced for the 5.0 nm NCs than for the 9.2 nm ones (~30 meV vs ~80 meV, respectively, Figure

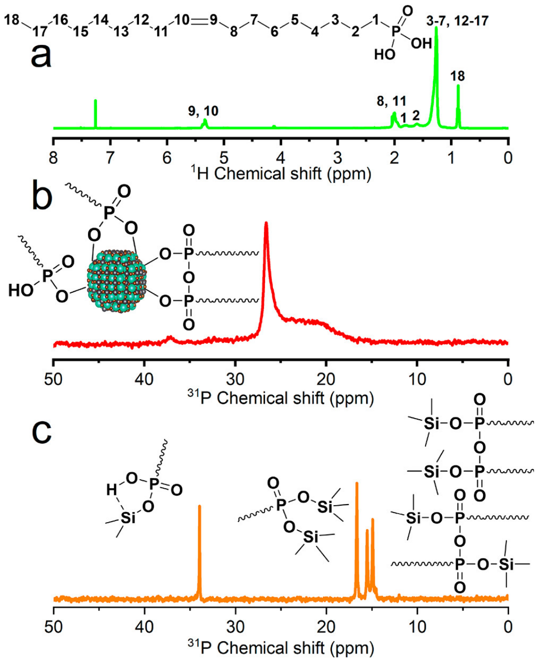

Figure 2.5: a) ^{1}H NMR and (b) ^{31}P NMR spectra of quantum confined (5.0 nm) $CsPbBr_3$NCs dispersed in $CDClr_3$. (c) ^{31}P NMR spectrum in $CDClr_3$ of the products of the reaction between OLPA-based NCs and TMS-Cl.

2.6a,b,d). The most striking difference between the optical properties of small vs weakly confined NCs was found by comparing the temperature evolution of the respective PL kinetics reported in Figure 2.6e,f. At room temperature, both systems showed a nearly single-exponential dynamics with lifetime (τ) of ~5 ns. Upon lowering the temperature, the PL dynamics of the 9.2 NCs progressively accelerated, reaching τ ~2.5 ns at T =5K (Figure 2.6e,g). This effect is typical of LHP NCs with a lateral size of 8 to 15 nm and has been ascribed to the radiative decay of bright triplet excitons becoming dominant at cryogenic temperatures[42, 48]. On the other hand, the evolution of the PL kinetics of the 5.0 nm NCs was substantially different: for 300 K $<$ T $<$ 50 K, the PL lifetime gradually lengthened, reaching τ ~13 ns at 50 K; at lower temperatures (i.e., below 50 K), the PL decay was characterized by a marked double exponential kinetics, with a fast resolution-limited component followed by a slow PL with τ ~700 ns (at 5 K), over 2 orders of magnitude longer than that at room temperature (Figure 2.6f). Importantly, no concomitant change of the PL intensity was observed (Figure 2.6c), indicating that such a double exponential decay kinetics originates from purely radiative effects. As sketched in the inset of Figure 3f, this behavior can be described by the thermal equilibrium between two states: a higher energy excitonic state (labeled as 1) with a large oscillator strength responsible for the fast decay at room temperature and a lower lying state (labeled as 2),

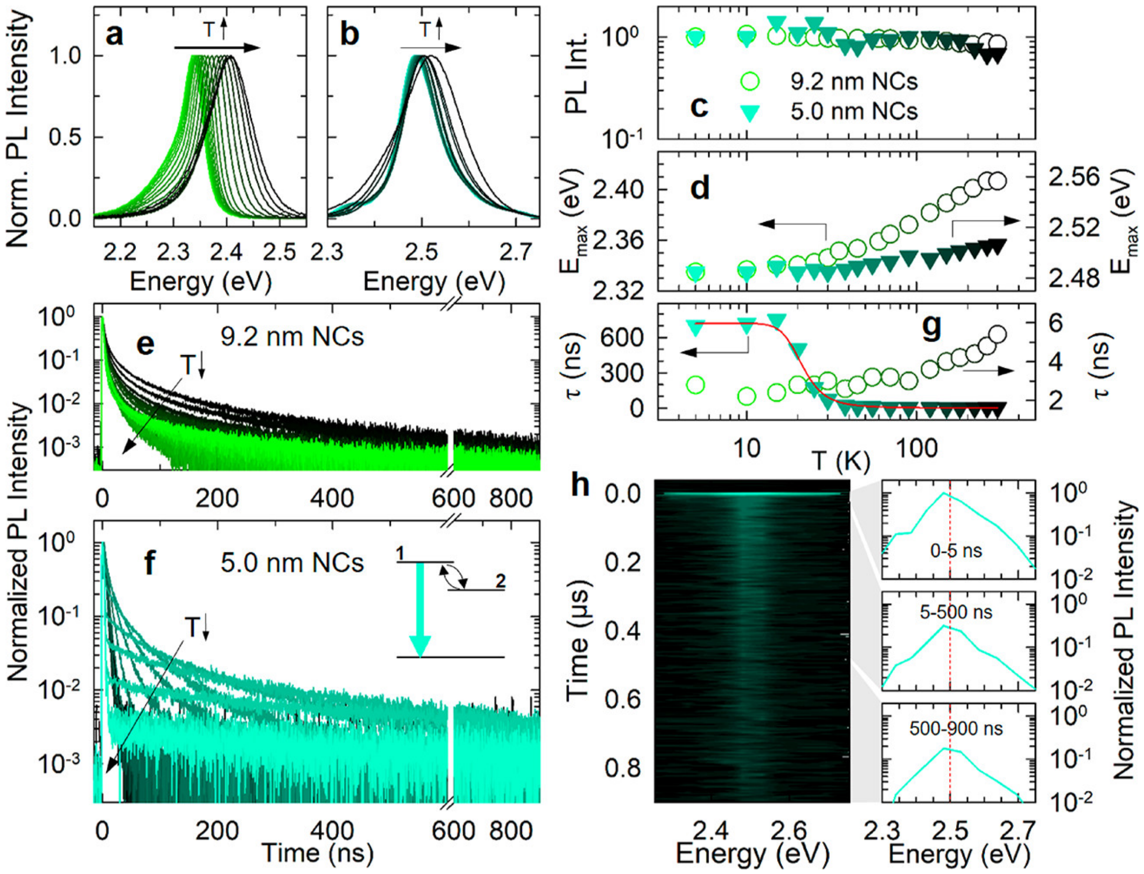

Figure 2.6: Normalized PL spectra of (a) 9.2 nm and (b) 5.0 nm OLPA-based $CsPbBr_3$ NCs as a function of temperature from T = 5 K (light green) to T = 300 K (dark green). Temperature dependence of (c) the PL intensity (normalized to the value at T = 5K) and (d) the PL energy position of the 9.2 and 5.0 nm NCs (circles and triangles, respectively). Normalized PL decay traces as a function of temperature of (e) 9.2 nm and (f) 5.0 nm NCs acquired at the PL peak. Inset: Sketch of the thermal equilibrium between a high-energy emissive state (1) and a lower-energy, nonemissive state (2). (g) Temperature dependencies of the PL lifetimes. The red line is the result of the fitting procedure with eq 1 for the 5.0 nm NCs. (h) Contour plot of the PL emission of 5.0 nm NCs acquired at T = 5 K together with the respective PL spectra as extracted by integrating in the 0 to 5 ns (top panel), 5 to 500 ns (middle panel), and 500 to 900 ns (bottom panel) ranges. The same color scheme applies to all panels

weakly optically coupled to the ground state, that determines the slow PL kinetics below 20 K. According to literature studies [42] on less confined crystals such excitonic states are ascribed as follows: the top of the valence band arises from a mixture of Pb 6s and Br 4p atomic orbitals, with an overall s symmetry, while the the conduction band consists of Pb 6p orbitals, leading to three possible orthogonal spatial components for the Bloch function.

At high temperatures, state 1 is thermally populated, and the respective fast PL, thus, dominates the emission. Upon lowering the temperature, excitons thermalized into state 2 could no longer be promoted to state 1, resulting in the very slow PL tail. Consistent with this picture, we adequately fitted the trend of τ as a function of temperature with the equation:

$$\tau(T) = (1 + exp(\Delta_{1,2}/k_b T))/(\tau^{-1} + \tau^{-2} exp(\Delta_{1,2}/k_b T)) \tag{2.1}$$

where k_b is the Boltzmann constant, $\tau_1 1$ and τ_2 are the PL lifetimes of state 1 and 2, respectively, and $\delta_{1,2}$ is the energy separation between these two states (Figure 2.6g). From the fitting procedure, we obtained $\delta_{1,2}$ ~12 meV, which is significantly smaller than the PL line width of the NC ensemble. Consistently, the contour plot of the time-resolved PL of the 5.0 nm OLPA-based NCs showed no spectral modification over time. This effect can be better appreciated by looking at the PL spectra obtained by integrating the contour plot in the 0 to 5 ns (which is dominated by the resolution-limited component), 5 to 500 ns, and 500 to 900 ns time ranges, all featuring the same PL profile (Figure 3h). All such observations, including comparable value for $\delta_{1,2}$, agree with recent results on small $CsPbBr_3$ NCs, ascribing the long-lived PL tail at cryogenic temperatures to the radiative decay of a nonemissive or "dark" exciton state [41]. To date, such an interpretation is mostly based on the phenomenological similarity to the exciton fine structure effects commonly observed for strongly confined CdSe NCs, yet a detailed theoretical description of the exciton fine structure of quantum confined LHP NCs is still lacking. Therefore, our results could be of interest to extend the theoretical framework currently available for larger NCs (lateral size of 8 to 15 nm) through the above-mentioned bright-triplet model,[42] to more strongly confined NCs where the exciton fine structure could be substantially different. For completeness, we do not exclude that the observed phenomenology could also arise from the involvement of very shallow trap states that store the excitation at low temperature (via single carrier or exciton trapping) and slowly repopulate the band edge, leading to the long-lived PL tail. In this case, however, constant PLQY with decreasing temperature would require suppression, at identical temperatures, of nonradiative decay channels for long-lived trapped carriers and band edge excitons, which is unlikely to occur. The in-depth investigation of such a photophysical response and the nature of the involved electronic states is beyond the scope of this work and will be addressed in a dedicated study.

2.1.2. Conclusions and future works

In summary, we synthesized $CsPbBr_3$ NCs using oleylphosphonic acid (OLPA), which allows us to lower the reaction temperature (100 °C) and make it possible to finely control the size, down to 5.0 nm, thus giving us access to NCs in the quantum confinement regime that are colloidally stable. OLPA-based NCs are passivated by different species, including phosphonates, hydrogen phosphonates, and phosphonic acid anhydrides, and form very stable colloidal solutions even at very low concentrations (1-10 nM) and when exposed to air. Side-by-side PL measurements at cryogenic temperatures evidenced striking differences in the low-temperature emission kinetics between quantum-confined OLPA-based NCs and larger NCs. Such differences are in agreement with recently invoked size-dependent excitonic fine structure effects, giving rise to thermal equilibria between competitive radiative processes. We believe that the concept of using ligand with strong binding affinity to the surface of the NCs and at the same time having a high solubility in solvents, and organic media in general, can be exploited further for the synthesis of other metal halide NC systems.

2.2. Halide Perovskite–Lead Chalcohalide Nanocrystal Heterostructures

2.2.1. Introduction

Various groups have tackled the synthesis of NC heterostructures in which the perovskite domain is bound to a domain of another material[49, 50]. Examples include metal-perovskite (Au- $CsPbBr_3$),[51] metal chalcogenide-perovskite (PbS-$CsPbX_3$, [52] ZnS-$CsPbX_3$, [53, 54] and PbSe-$CsPbX_3$ [55], metal dichalcogenide-perovskite (Cs_2,SnI_6,/SnS_2,),[56] $CsPbX_3$/metal oxide Janus TiO_2-$CsPbBr_3$, [57] $CsPbX_3$/SiO_2,, [58] $CsPbX_3$/ZrO_2,, [59] and $CsPbBr_3$/TiO2 [60], CsBr-$CsPbBr_3$, [61] and Cs_4,$PbBr_6$,-$CsPbBr_3$ NCs[62]. The latter case is a particularly revealing example of an epitaxial heterointerface (recently disclosed by our group), in which it is possible to observe a continuity of the sublattice of Cs^+ cations across the interface between the two domains, a common theme underlying the various heterostructures involving metal halide NCs[63]. Many of these nano-heterostructures may find applications in various fields, such as solar cells, LEDs, and photocatalysis[60, 64, 65]. In the present work, we report a new type of heterostructure, in which a halide perovskite NC shares an epitaxial interface with a lead chalcohalide NC. Colloidal NCs of lead chalcohalides have been recently synthesized [66]: they are characterized by an indirect band gap, are nonemissive at room temperature, and are stable for months under ambient conditions[66].The synthesis that we discuss initially delivers $CsPbBr_3$-$Pb_4S_3Br_2$ NCs: from them, we could further prepare, by postsynthesis anion exchange, the corresponding heterostructures in which the perovskite domain is either $CsPbCl_3$ or $CsPbI_3$. In other words, anion exchange only affects the perovskite region and not the chalcohalide one, which remains $Pb_4S_3Br_2$. In all these heterostructures, the two domains are separated by a sharp interface. Epitaxial relationships between the two domains are possible due to a favorable matching of the respective Pb sublattices in the two structures, when they are arranged in some specific mutual orientations. In all the systems studied, density functional theory (DFT) calculations highlight that the interface joining $CsPbX_3$ and $Pb_4S_3Br_2$ leads to a significant change in the electronic structures of the individual components. In the heterostructure, the edge of the valence band is localized almost completely in the chalcohalide domain, whereas the edge of the conduction band is distributed almost evenly across the heterostructure. This indicates that the overall system is not just the sum of its components but a potentially valuable platform for wave function engineering strategies that are not typically accessible with halide perovskite materials due to compositional alloying promoted by ion migration. The resulting quasi-type II-like energy level alignment at the heterojunction promotes the rapid splitting of photogenerated excitons with the photoexcited hole localized in the chalcohalide domain and the electron partially delocalized in the entire nanostructure. This, together with the rapid carrier trapping at interface localized states, as also predicted by DFT, leads to a nearly complete suppression of the photoluminescence (PL) with respect to the pure NCs. Nonetheless, low-temperature spectroscopic measurements reveal a red-shifted PL (compared to that from pure $Pb_4S_3Br_2$ NCs), which is likely due to the optical recombination of interface trapped carriers, whose efficiency is substantially affected by nonradiative channels. Notably, the presence of the interface confers higher structural rigidity to the perovskite lattice. This is evident in the $CsPbI_3$-$Pb_4S_3Br_2$ heterostructure, in which the $CsPbI_3$ domain over time does not transform to the thermodynamically stable δ “yellow” phase, as is well established for $CsPbI_3$ NCs, but remains in the metastable “black” γ phase.

2.2.2. The $CsPbBr_3/Pb_4S_3Br_2$ heterostructure

2.2.3. Synthesis

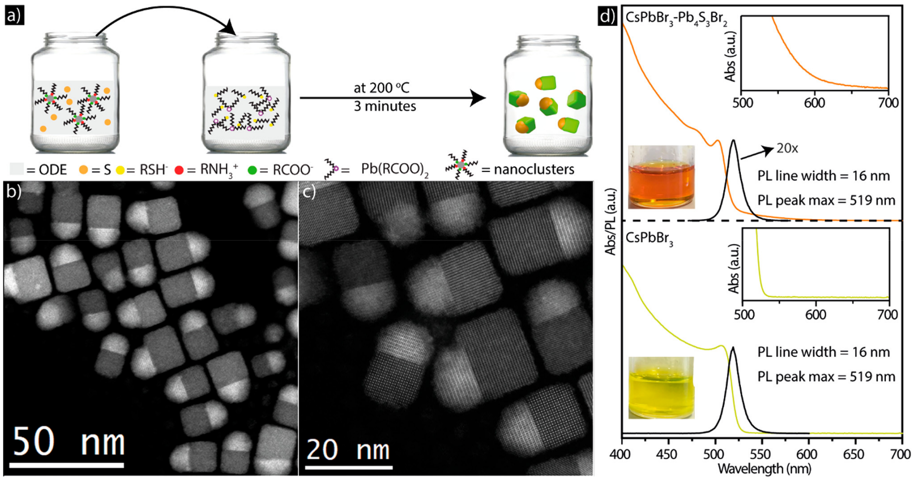

Figure 2.7: (a) Sketch describing the synthesis of the $CsPbBr_3$-$Pb_4S_3Br_2$ heterostructures. STEM images of (b, c) $CsPbBr_3/Pb_4S_3Br_2$ NCs at two different magnifications. (d) Absorbance and PL spectra of dispersions in toluene of the $CsPbBr_3/Pb_4S_3Br_2$ heterostructures and the $CsPbBr_3$ NCs, along with the photographs of the corresponding colloidal dispersions under room light. The insets are magnified absorption features in the 500- 700 nm range for both samples

The synthesis of the heterostructures started with the preparation and purification of $CsPbBr_3$ nanoclusters, following a previously reported method[67]. These clusters, of subnanometer size, have an exciton absorption at 402 nm and are nonemissive at room temperature. They have been recently prepared and used as convenient “monomers” for the growth of perovskite NCs, as they enable a more precise control over size and shape than by using a standard synthesis approach, including the possibility to access branched geometries[68]. In the preparation of these clusters, both oleic acid and oleylammine were used. It is therefore likely that their surface is coated by both oleate and oleylammonium ions. In a typical synthesis, these nanoclusters were mixed with a solution of elemental sulfur dissolved in degassed octadecene (ODE), and the resulting mixture was injected in a vial containing a solution of dodecanethiol and lead oleate in degassed ODE, heated at 200 degrees (Figure 2.7). The reaction was allowed to proceed for 3 min and was subsequently quenched by immersing the vial in an ice water bath. The NCs were collected by centrifugation and were then redispersed in toluene for further use. High angle annular dark field scanning transmission electron microscopy (HAADF-STEM) analysis evidenced the presence of heterostructures formed by a cubic shaped domain bound to a more rounded and higher contrast domain with an edge length of 20.3 ± 2.2 nm, most often along one face of the cube (Figure 1b,c). A statistical analysis done on roughly 1300 NCs indicated that only around 80 NCs (i.e., around 6% of the total) were cubes, apparently not carrying an additional domain attached to them. On the other hand, contrast variations in most of these cubes suggest that most of them were heterostructures as well, but they were simply sitting on the substrate in a verticalor lateral projection. Overall, we can state that the fraction of isolated $CsPbBr_3$ NCs in this sample was definitely below 6%. If instead the initial $CsPbBr_3$ nanoclusters were heated under the same conditions as in the synthesis that we have just described for the heterostructures of Figure 1b,c, but in ODE alone (that is, with no elemental sulfur, dodecanethiol, and lead oleate), the product was represented by nearly monodisperse $CsPbBr_3$ cube-shaped NCs with an edge length of 15.9 ± 1.6 nm. Optical absorption and photoluminescence (PL) spectra of colloidal dispersions of the cube-shaped $CsPbBr_3$ NCs and of the heterostructures are reported in Figure 1d. Compared to the $CsPbBr_3$ NCs, the heterostructures exhibited an additional absorption tail at long wavelengths, which became more prominent for wavelengths shorter than 550 nm. The two insets of figure 2.7 are magnified views of the absorption features in the range 500-700 nm for both samples. For the heterostructure, this feature matched closely the optical absorption spectrum of our recently synthesized $Pb_4Br_3S_2$ NCs [66]. The $CsPbBr_3$ NCs evidenced the typical narrow PL peak (full-width-half-maximum, FWHM, of 16-17 nm) at 519 nm. The formation of the heterostructure led to a substantial suppression of the $CsPbBr_3$ NC emission, as discussed in detail later. The much weaker emission from the heterostructures sample (5% of the $CsPbBr_3$ NC PL intensity) can be ascribed to the few $CsPbBr_3$ NCs present in solution that are not bound to a $Pb_4S_3Br_2$ domain, in quantitative agreement with the statistical analysis of the wide-field TEM images (indicating less than 6% residual $CsPbBr_3$ cubes). The X-ray powder diffraction (XRPD) pattern of the cubes contained diffraction features that are ascribable to the orthorhombic phase of $CsPbBr_3$. The pattern of the heterostructures had the same features as that of the $CsPbBr_3$ cubes, with additional peaks appearing around 25° and 36° (2θ). To identify the origin of these extra peaks, we recorded XRPD patterns of $Pb_4Br_3S_2$ NC and of mixtures of $CsPbBr_3$ and $Pb_4Br_3S_2$ NC powders. A comparison of these various patterns confirmed that the XRPD pattern of the heterostructures had contribution from both phases, albeit with strong predominance of the signal from the perovskite domain. We tested the influence of reaction temperature, time, relative concentrations of dodecanethiol and of lead oleate, and addition of oleylammonium bromide (OLAM-Br) on the formation of the heterostructures, while keeping the concentration of $CsPbBr_3$ clusters constant. In brief, the optimal temperature window for growing the heterostructures was around 200 °C. At sensibly lower temperatures (150 °C or below) no heterostructures were formed, and at higher temperatures (230 °C) the size and shape distributions worsened considerably. We then tested the influence of dodecanethiol in syntheses performed at the optimal temperature of 200 °C. In the absence of dodecanethiol, no $CsPbBr_3$- $Pb_4S_3Br_2$ heterostructures were formed, and instead we obtained large $CsPbBr_3$ NCs, each carrying a tiny, low contrast domain attached to it. At increasing amounts of dodecanethiol added, past a range of concentrations that enabled the ideal growth of heterostructures, the latter were still formed, but their size and shape distributions worsened considerably; additionally, PbS NCs appeared as a byproduct. A controlled amount of lead oleate was also critical to prepare well-defined heterostructures. With excessive addition of lead oleate, isolated $Pb_4S_3Br_2$ particles were found as a byproduct. To understand the growth mechanism, syntheses were run at varying reaction times, while all other reaction conditions were kept constant (including the synthesis temperature, always set at 200 °C). The TEM images of the sample obtained after 30 s of reaction time evidenced nearly cube-shaped NCs containing higher contrast domains (presumably $Pb_4S_3Br_2$) at their edges. These higher contrast domains further grew in sizes at longer reaction times, while the perovskite domain remained nearly the same. This trend was confirmed by optical absorption spectra of the corresponding samples (dominated by the features from $CsPbBr_3$), which remained almost unchanged over the course of the reaction. By crossing the TEM images and optical absorption data of various samples prepared with different reaction times, we conclude that the perovskite domains formed first, followed by the growth of $Pb_4S_3Br_2$. The optimal reaction time was around 3 min. The $CsPbBr_3$ clusters that were used as "precursors" for the perovskite domain have a large surface-to-volume ratio; hence, their dissolution during the synthesis of the heterostructures should release a certain amount of oleylammonium ions. This is, however, negligible compared to the amount of oleate that was added (as lead oleate) together with the $CsPbBr_3$ clusters. To test the influence of higher concentrations of oleylammonium ions, we also attempted the synthesis of $CsPbBr_3$- $Pb_4S_3Br_2$ heterostructures under the same conditions as in the synthesis of Figure 2.7b,c, but with the extra addition of 10-2 mmol of OLAM-Br. These attempts failed at producing heterostructures. TEM analysis revealed that the product was mainly represented by $CsPbBr_3$ nanoplatelets/ lamellar structures. As a final test, we also attempted to synthesize $CsPbBr_3$- $Pb_4S_3Br_2$ heterostructures by following conventional hot injection-based syntheses used for the preparation of halide perovskite NC, that is, not employing preformed $CsPbBr_3$ nanoclusters,[69–71] but none of them was successful. Therefore, we inferred that a controlled growth of the heterostructures was possible only through the use of $CsPbBr_3$ nanoclusters, most likely as they prevent a massive homogeneous nucleation of perovskite NCs, separately from the chalcohalide NCs.

2.2.4. Characterization by Electron Microscopy

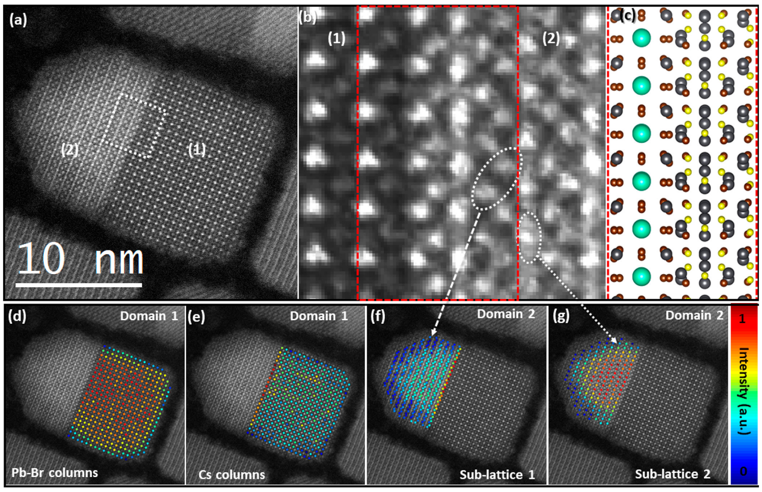

Figure 2.8: . Structural analysis of a single $CsPbBr_3$-$Pb_4S_3Br_2$ heterostructure. (a) High-resolution HAADF-STEM image of a single heterostructure composed by a $CsPbBr_3$ (1) and a $Pb_4S_3Br_2$ (2) domains. (b) Magnified image of the region highlighted in white in (a), depicting the interface between $CsPbBr_3$ and $Pb_4S_3Br_2$ domains. The region highlighted in red represent a $Pb_4S_3Br_2$ pattern oriented along the [101] zone axis, as confirmed in (c) showing the CsPbr3 and $Pb_4S_3Br_2$ structural model along this orientation. (d) Column intensity map of Pb-Br columns of the perovskite phase. (e) Column intensity map of Cs columns of the perovskite phase. (f) and (g) represent the intensity map of Pb columns belonging to the $Pb_4S_3Br_2$ domain

Detailed analyses were performed on single heterostructures through high-resolution, high-angle annular dark field scanning TEM (HAADF-STEM) imaging. Figure 2a represents a highresolution HAADF-STEM image of a typical $CsPbBr_3$- $Pb_4S_3Br_2$ heterostructure. Both domains were single crystalline. The chalcohalide domain is facing the [101] zone axis, as demonstrated by its Fourier transform (FT, Figure S16), and is attached to one of the facets of the $CsPbBr_3$ cube-shaped NC. The orthorhombic perovskite domain FT can be matched with either the [101] or [010] zone axes, as those are almost indistinguishable because of the small deviation from the ideal cubic symmetry. The same is true for (101) and (010) planes, which are the planes exposed by the facets of NCs. From a close scrutiny of several heterostructures, we found that the lead chalcohalide domains can grow most commonly on the (101) facets and less commonly on the (010) and (001) facets of the orthorhombic $CsPbBr_3$ perovskite NC, with a mutual orientation of the two domains such that there is little or nearly no mismatch between the joining planes. It is also interesting that although the $CsPbBr_3$ NCs present several sets of equivalent facets, basically all the heterostructures that we could observe were made of only one domain of chalcohalide, and not of multiple domains, attached to a $CsPbBr_3$ NC. This behavior is most likely due to a slow nucleation kinetics of the chalcohalide on the surface of the perovskite NC. Our interpretation is that as soon as a nucleus of chalcohalide is formed on one facet of a $CsPbBr_3$ NC, the energetic barrier for its further accretion is much lower than the energetic barrier for the formation of other chalcohalide nuclei on the other facets. We then quantitatively analyzed the intensities of the individual atomic columns in a single heterostructure by using STAT-STEM [72]. In an HAADF-STEM image, the intensity of an atomic column depends on the material thickness (amount of atoms composing the column) and its atomic composition (Z number). Panels d and e of figure 2.8 show the intensities of the Pb-Br and Cs columns of the perovskite domain, while panels f and g of figure 2.8 represent the Pb column intensities of sublattices 1 and 2 from the $Pb_4S_3Br_2$ domain, respectively. The relatively homogeneous distribution confirmed the singlephase character of both the perovskite and the lead chalcohalide domains. Notably, the atomic columns located at the interface presented higher intensities, especially the Cs columns and the columns belonging to the sublattice 2 of the $Pb_4S_3Br_2$ domain (figure 2.8 e,f). The intensity of the atomic columns located at the boundary of two materials can be affected by local strain that can change the alignment of the atoms, which in turn modifies the channeling effect that is at the base of the HAADF-STEM signal[73]. In this specific case, such rearrangement appears to bring the atoms close to a perfect alignment in the specific zone axis along which the heterostructure is being imaged. The compositional analysis by energy dispersive X-ray spectroscopy (STEM-EDX) of individual heterostructures attested a uniform distribution of the corresponding elements in the respective domains and returned elemental ratios of Cs:Pb:Br equal to 1.05:1:2.7 for the perovskite domain and of Pb:S:Br equal to 4:2.9:2.6 for the lead chalcobromide domain. These values are in line with the respective stoichiometries of the two materials (i.e., $Pb_4S_3Br_2$ and $CsPbBr_3$). This was further supported by an EDX-line scan across a single heterostructure which evidenced that the Cs signal was localized in the perovskite domain and the S signal was mainly present in the $Pb_4S_3Br_2$ domain. A close look at the epitaxial relationship between the two domains, as sketched in Figure figure 2.8b, reveals that the lead and bromide ions in the perovskite are aligned with those of the chalcobromide. This is made clearer in Figure 2.9 , showing how the interface monolayer of $Pb_4S_3Br_2$ presents an atomic arrangement similar to the perovskite orthorhombic lattice if one focuses on the Pb atoms only.

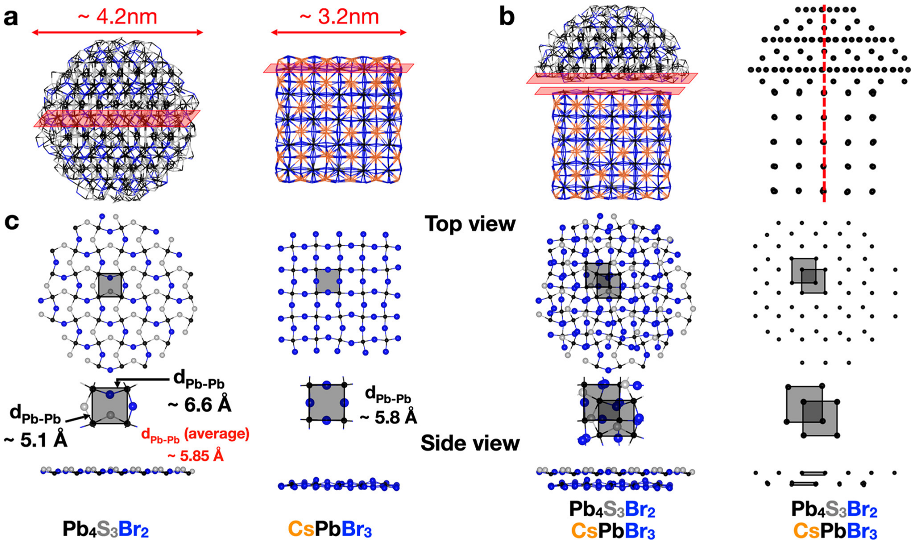

Figure 2.9: (a) Sticks representation of (left) a spherical ~4.2 nm diameter $Pb_{548}S_{423}Br_{250}$ NC model and (right) a cubic ~3.2 nm sided $Cs_{200}Pb_{125}Br_{450}$ NC model optimized at the DFT/PBE level of theory. (b) Preparation of the heterostructure NC model by (left) stacking of the $Pb_4S_3Br_2$ and $CsPbBr_3$ moieties and (right) alignment of their Pb ions along the [010] axis. (c) Top and side view of the interface layers of both the $Pb_4S_3Br_2$ and $CsPbBr_3$ nanocrystals. A cell of four Pb ions was taken to demonstrate the smooth alignment at the interface.

2.2.5. DFT modeling

The models discussed above give us important hints on how to build a model of the heterostructure for our DFT calculations. For the $CsPbX_3$ perovskite cube we have simply taken one of our "trap-free" models of about 3.2 nm in size published earlier,29 whereas for the lead chalcohalide we first cleaved the bulk into a sphere of 4.2 nm diameter with a

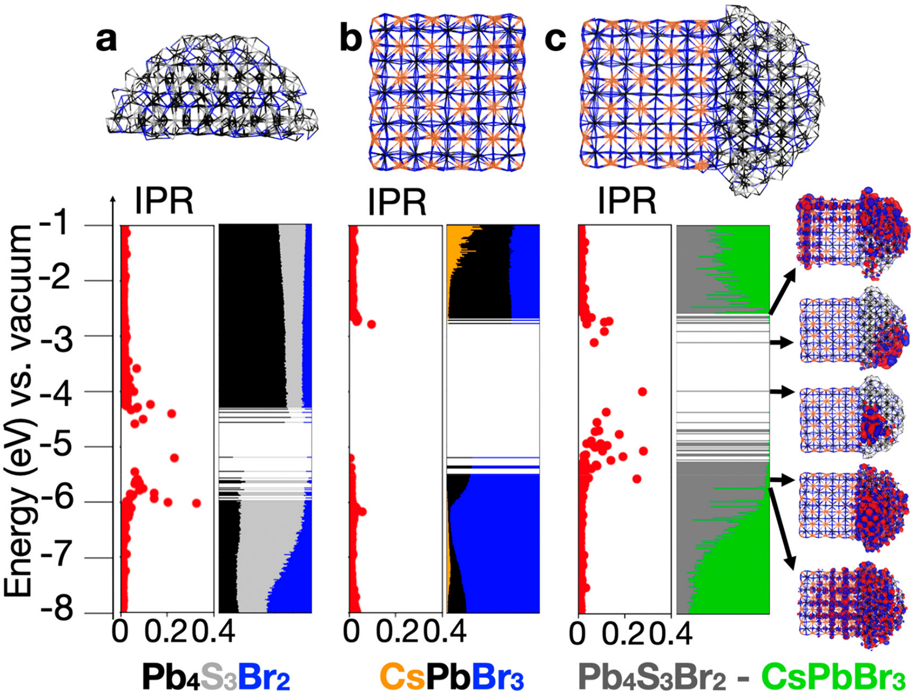

Figure 2.10: Electronic structure and IPR plots of the (a) $Pb_4S_3Br_2$ half-sphere model, (b) $CsPbBr_3$ cube model, and (c) heterostructure model computed at the DFT/PBE level of theory. The color code indicates the contribution of an atom/moiety type to each molecular orbitals. On the right we plotted both delocalized and localized molecular orbitals at the band edges

charge balanced stoichiometry (2.9a), and then we relaxed the structure and computed its density of states. This shows a large number of surface defects, as evidenced by the inverse participation ratio (IPR) analysis (2.10a). IPR with values deviating significantly from zero provide a fingerprint for the presence of localized states in the electronic structure, which in the case of chalcohalide are mostly present at the conduction band (CB) and valence band (VB) edges. For comparison, the IPR analysis for the perovskite systems exhibits only delocalized states, as expected (2.10b). IPR values can also be used to filter trap states in the electronic structure and deduce the actual intake of the CB and VB edges, here extrapolated (with IPR below 0.03) at about 1.6-1.7 eV (2.10a), in good agreement with the experimental value for the emission of 1.6-1.8 eV for $Pb_4S_3Br_2$ (see the discussion on the optical properties). Note that as in the case of lead halide perovskites our DFT approach provides the correct band gap for the wrong reason: the lack of spin-orbit coupling in our calculations, which lowers the band gap but is computationally prohibitive for the heterostructure size, is compensated by the typical band gap underestimation for pure exchange-correlation functionals like the Perdew-Burke-Ernzerhof (PBE) employed here. The choice of IPR below 0.03 is arbitrary; however, it does indicate that trap states are present in various kinds, from very localized to less localized ones. After we assessed this part, we cut half of the chalcohalide sphere, relaxed it, and arranged it on top of the perovskite domain, following the alignment proposed above and sketched in 2.9b,c. The relaxation of the heterostructure occurred smoothly, an indication that the structural alignment between the two domains was indeed the correct one. We then computed the electronic structure and the density of states followed by the IPR analysis. As expected, by looking at the electronic structure of the domains computed separately, the CB edge of the heterostructure is apparently dominated by the $Pb_4S_3Br_2$ domain. Notably, although the band edge is fully defined by trap states, as expressed by the IPR values, the first delocalized states in the CB are present in both the chalcohalide and perovskite domains. To make this clear, we plotted the molecular orbitals for both the localized states and the first of the delocalized one (2.10c). Conversely, in the valence band region, the orbital contribution is different. The first states at the VB edge are still mostly localized in the chalcohalide domain, pointing toward the presence of an energy offset with the perovskite domain. The first delocalized molecular orbitals deeper in the VB appear intermixed, with some present only on the chalcohalide domain and others delocalized on both domains (2.10c). States even deeper exhibit mostly mixing between the two domains. Notably, there are no states at the VB edge region that belong solely to the perovskite domain. Overall, following the core-shell nomenclature,[74] these data suggest that the energy level alignment of the heterostructure is quasi-type II, with the VB localized on the chalcohalide domain and the CB mixed between the two domains.

2.2.6. Optical Properties

On the basis of theoretical insights provided by DFT, we proceeded to investigate the excitonic processes of the $CsPbBr_3$-$Pb_4S_3Br_2$ heterostructures. To this end, we prepared pure $CsPbBr_3$ and $Pb_4S_3Br_2$ NCs of nearly the same size as the respective domains in the heterostructure (namely, $CsPbBr_3$NCs having an edge length of 14 nm and $Pb_4S_3Br_2$ NCs with a diameter of 8.5 nm) and performed sideby-side optical spectroscopy experiments. The optical spectra for $CsPbBr_3$ NCs and related heterostructures are shown in Figure 2.11a. As anticipated, the pure $CsPbBr_3$ NCs featured the typical sharp absorption edge and a nearly resonant PL peak with PLQY = 67 ± 7%. The PL dynamic followed a multiexponential decay with effective lifetime of circa 10 ns (Figure 2.11b). The spectral properties of the $Pb_4S_3Br_2$ NCs are reported in Figure 2.11c and show a nearly featureless absorption spectrum typical of an indirect band gap material,29 as confirmed by the Tauc plot in the inset of Figure 2.11c, showing a linear dependence of the absorption profile on the square root of (αh), where α is the absorption coefficient and h the energy of the

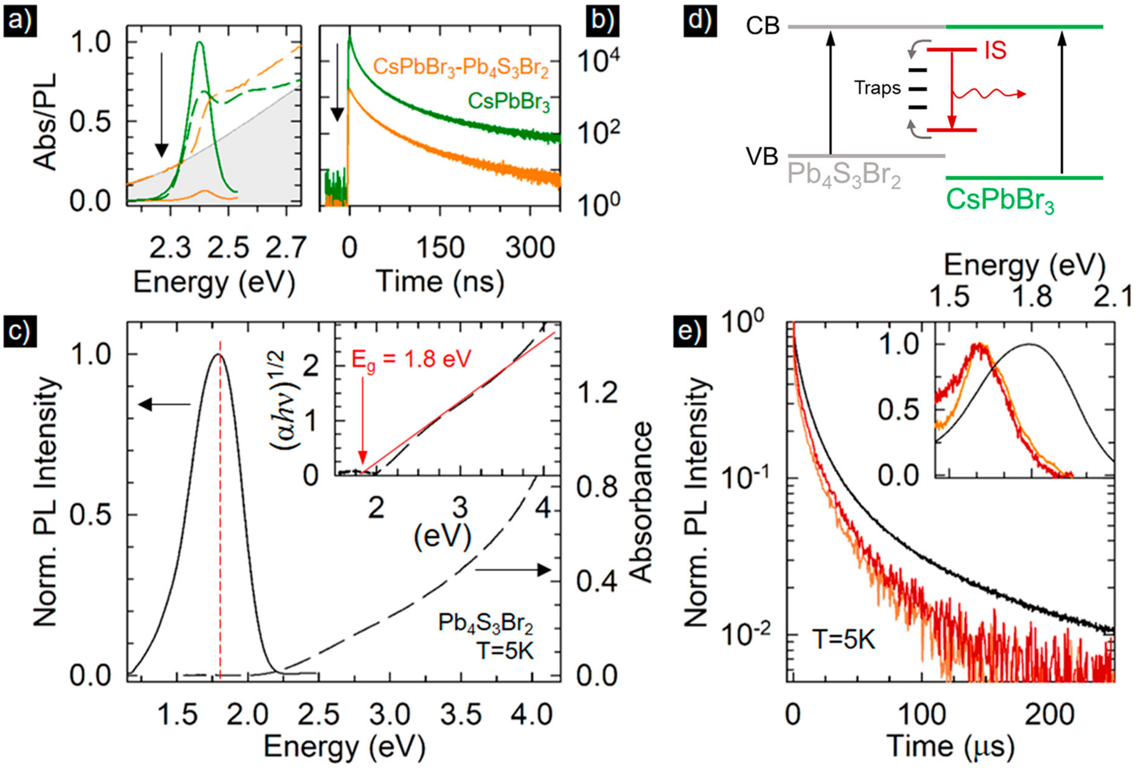

Figure 2.11: . (a) Optical absorption PL spectra and (b) time-resolved PL decay curves of colloidal dispersions of $CsPbBr_3$ NCs and $CsPbBr_3$- $Pb_4S_3Br_2$ heterostructures (normalized to the intensity of bare $CsPbBr_3$ NCs). Green lines refer to $CsPbBr_3$ NCs, and orange lines refer to the heterostructure. The arrow highlights the quenching of the PL intensity in the heterostructure. (c) Optical absorption and PL spectra of $Pb_4S_3Br_2$ NCs (excitation at 3.5 eV). Inset: respective Tauc plot showing the linear dependence (red line) of (h)1/2 with the photon energy typical for indirect band gap transitions. The red arrow indicates the band gap energy that corresponds to the PL peak position. (d) Schematic depiction of the energy levels of the $CsPbBr_3$-$Pb_4S_3Br_2$ heterostructure highlighting the radiative recombination (red arrow) in interface localized states (IS) following excitation of either the perovskite or chalcobromide domains and the respective quenching by traps. (e) Time decay curves of the $Pb_4S_3Br_2$ PL from $CsPbBr_3/Pb_4S_3Br_2$ NCs at $T = 5$ K upon 2.33 and 3.5 eV excitation energy (orange and red lines, respectively) compared to the PL decay curve of bare $Pb_4S_3Br_2$ NCs (black line). Inset: PL spectra of $CsPbBr_3$-$Pb_4S_3Br_2$ NCs at $T = 5$ K upon 2.33 and 3.5 eV excitation energy (orange and red lines, respectively) compared to the PL spectrum of $Pb_4S_3Br_2$ NCs at the same temperature.

incident photons. The fitting yields a band gap energy of ∼1.8 eV, in good agreement with the band gap energy estimated by DFT (figure 2.10a). The broad PL spectrum was also peaked at ∼1.8 eV, thus indicating that the radiative recombination is due to an indirect transition coupling the band edge states, possibly promoted by partial relaxation of momentum conservation in nanoscale systems. The PLQY at room temperature was $<1\%$, likely due to nonradiative quenching by carrier trapping in surface defects. Cooling the $Pb_4S_3Br_2$ NCs to cryogenic temperatures strongly suppressed such nonradiative losses, resulting in a substantial enhancement of the PL intensity at $T = 5$ K, accompanied by a concomitant lengthening of the PL lifetime that increased from 70 ns to 4.1 μs (Figure 2.12. This behavior suggests a recombination from an indirect transition. Combining the $Pb_4S_3Br_2$ and $CsPbBr_3$ domains in the heterostructure strongly quenches the emission from both domains. The quenching of the PL from $CsPbBr_3$ in the heterostructure is consistent with an ultrafast hole transfer from the perovskite domain to the $Pb_4S_3Br_2$ domain (Figure 2.11). The very weak green PL that was observed from the

sample of heterostructures had the same spectral position and decay kinetics as the sample of pure $CsPbBr_3$ NCs (Figure 2.11ab) Hence, we ascribe this residual PL to the presence of isolated $CsPbBr_3$ NCs in the sample of heterostructures. Interestingly, by cooling the heterostructures to $T < 70$ K, an emission peak at 1.60 eV emerged, either under direct excitation of the $CsPbBr_3$ domain at 2.33 eV (that is, below the band gap of the $CsPbBr_3$ NCs) or under UV excitation at 3.5 eV. This emission was red-shifted by $\sim$200 meV from that observed, at the same temperature, in the sample of pure $Pb_4S_3Br_2$ NCs and was thus ascribed to the recombination from intragap localized states in the heterostructures, consistent with the DFT analysis in Figure 2.10c. No such emission was observed from the heterostructures at room temperature, indicating substantial nonradiative losses, likely associated with carrier trapping. Also, the PL decay at 5 K associated with such 1.6 eV emission from the heterostructures was faster than the PL decay of the 1.8 eV emission from the $Pb_4S_3Br_2$ NCs (1.6 μs vs 4.1 μs) and was identical under either excitation conditions (2.33 and 3.5 eV). This behavior suggests that in the heterostructure the PL dynamics does not depend on the regions of the heterostructure where the photocarriers are initially generated and confirms the quenching effect of the interface.

2.2.7. Heterostructures obtained by halogen exchange

The exposure of the $CsPbBr_3$-$Pb_4S_3Br_2$ heterostructures to either Cl or I- ions resulted in anion exchange, as evidenced by the changes in the optical absorption spectra (Figure 6a). Notably, the Cl^- treated sample exhibited a more evident absorption feature toward longer wavelengths in addition to the band edge absorption of the $CsPbCl_3$ domain. This tail, arising from the chalcohalide domain, is partially hidden in the initial sample and completely hidden in the iodide-exchanged sample. Morphological analysis by TEM showed that the NCs retained nearly the same size and shape as the initial NCs after

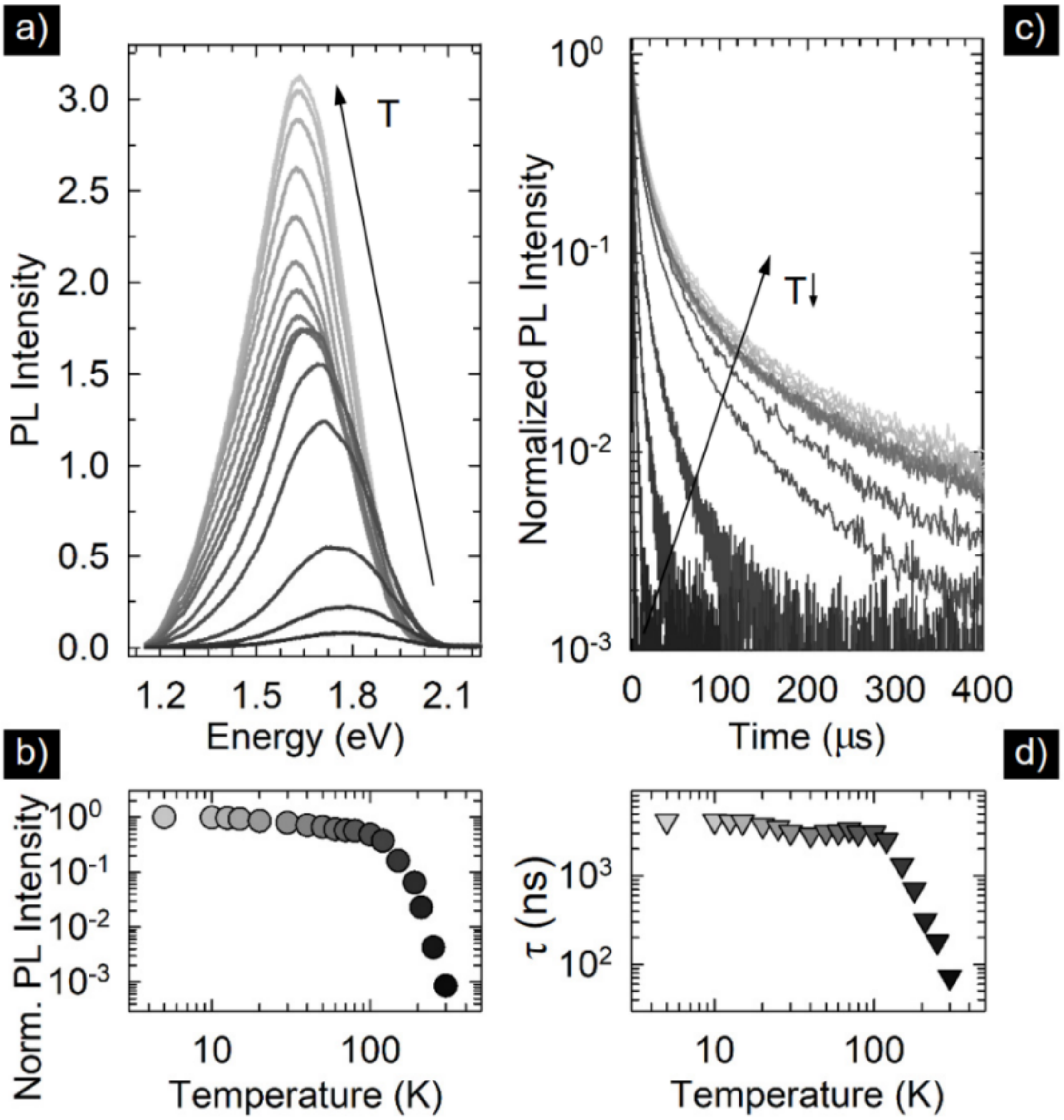

Figure 2.12: 5. (a) PL spectra of $Pb_4Br_3S_2$ NCs upon lowering the temperature from T=300 K down to T=5 K (from black to light grey curves, respectively). (b) Integrated PL intensity values as a function of temperature extracted from the PL spectra reported in ‘a’ and normalized to the value at T=5 K. (c) Time-resolved PL traces of $Pb_4Br_3S_2$ NCs upon lowering the temperature from T=300 K to T=5 K (from black to light grey curves, respectively). (d) Temperature dependence of the effective PL decay lifetimes (τ, evaluated as the time after which the PL intensity drops by a factor of e) extracted from the PL decay curved reported in ‘c’.

anion exchange. Compositional mapping of individual heterostructures by STEM-EDX to assess anion distribution evidenced a clear segregation of the Cl and the Br signals in

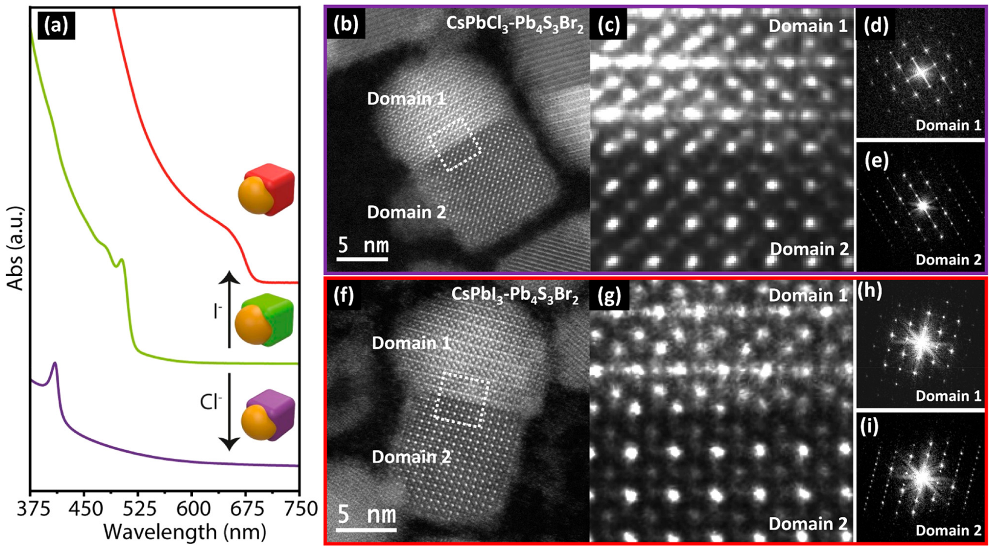

Figure 2.13: a) Optical absorption spectra of pristine $CsPbBr_3$-$Pb_4S_3Br_2$ NCs and of the same NCs after halide exchange with either Cl^- or I^- recorded in colloidal dispersions. (b) HRSTEM image of $CsPbCl_3$-$Pb_4S_3Br_2$ NC. (c) Magnified image of the region highlighted in white dotted line. (d) and (e) show the FT of the regions labeled as domain 1 and domain 2 in (b), respectively. (f) HRSTEM image of a CsPbl3-$Pb_4S_3Br_2$ NC. (g) Magnified image of the region highlighted in white dotted lines. (h) and (i) show the FTs of the domains labeled as domain 1 and domain 2 of panels f and g. The $CsPbCl_3$ and $CsPbI_3$ domains were in the [100] and [101] orientation, while the $Pb_4S_3Br_2$ domain was in the [101] orientation, respectively, with respect to the viewing direction.

the two domains of the heterostructures , with Cl preferentially segregated in the perovskite domain and Br in the chalcohalide domain, compatible with a $CsPbCl_3$-$Pb_4S_3Br_2$ composition for the heterostructure. Similar conclusions were drawn from EDX line scans on the heterostructures reacted with I- ions, suggesting a $CsPbI_3$-$Pb_4S_3Br_2$ composition in the latter case. HAADF-STEM analyses of these two samples revealed again a sharp interface between the two domains (Figure 6b- i), with the same epitaxial relationships as in the $CsPbBr_3$- $Pb_4S_3Br_2$ sample discussed earlier, evidencing that anion exchange had not disrupted the overall structure of the initial $CsPbBr_3$-$Pb_4S_3Br_2$ NCs. The sharpness of the interface was also obvious from the intensity maps of the various columns in the perovskite and chalcohalide domains in representative heterostructures belonging to these two samples. This was confirmed by the FT of the cubic $CsPbCl_3$ domain displayed in Figure 6d along its [100] zone axis and is in agreement with the XRPD analysis of the same sample. The FT of the iodide exchange sample is reported in Figure 6h and does not show the additional diffraction spots typical of an orthorhombic structure whereas the chalcohalide domains was found to be unaffected, retaining the $Pb_4S_3Br_2$ phase. The

XRPD pattern of the iodideexchanged sample unambiguously conformed to the “black” orthorhombic perovskite phase of $CsPbI_3$[75]. As a further control, the attempt at halide exchange on pure $Pb_4S_3Br_2$ NCs left the NCs unaltered comparing optical absorption, XRPD, and TEM data of $Pb_4S_3Br_2$ NCs before and after treatment with either Cl^- or I- ions). Taken together, these sets of data indicate that anion exchange took place only in the halide perovskite region of the heterostructures. The electronic structure and IPR analysis of these systems shows that also for the lead chloride and iodide perovskites the energy alignment is quasi-type II, with features similar to those of the bromide case. Extensive spectroscopic analysis was performed on these two heterostructures as well, revealing, in both cases nearly complete quenching of the PL from the perovskite domain, as observed for the $CsPbBr_3$-$Pb_4S_3Br_2$ systems. Notably, no acceleration was observed also for the kinetics of the $CsPbCl_3$ domain in the heterostructures with respect to the isolated $CsPbCl_3$ NCs. These kinetics, because of their fast decay time, were measured by using a streak camera with temporal resolution better than 7 ps (Figure 2.14), thus confirming the ultrafast nature of the hole transfer process.

One interesting question that arises in these nanostructures is whether the presence of the chalcohalide domain has any influence on the structural stability of the perovskite domain. This is particularly insightful for the “black” γ-$CsPbI_3$ phase, as this structure is metastable at room temperature and quickly undergoes a transition to the nonemitting “yellow” δ-$CsPbI_3$ phase in the case of colloidal NCs (on a time span of hours/ days). The “yellow” δ-$CsPbI_3$ phase is characterized by linear arrays of edge-sharing [PbI6] 4- octahedra, very much different structurally from the perovskite structure. By monitoring the stability of the $CsPbI_3$-$Pb_4Br_3S_2$ NCs both as colloidal dispersions and as solids films over time under air, and through a comparison with $CsPbI_3$ NCs of nearly the same size, we found the following: the $CsPbI_3$ NCs, as already well established, were very unstable, since they transformed to the yellow phase already within 1 day of storage under air, as revealed by XRPD analysis. On the other hand, after several days of aging, colloidal suspensions of $CsPbI_3$- $Pb_4Br_3S_2$ heterostructures did not show any relevant change, neither in their optical features and morphology nor in their XRPD patterns. Importantly, in the XRPD patterns, there are no additional diffraction peaks observed that belong to the δ-$CsPbI_3$ phase, even after 3 weeks of aging under air. We ascribe this structural stability to the presence of the interface joining $CsPbI_3$ and $Pb_4S_3Br_2$. This interface most likely confers higher structural rigidity to the perovskite $CsPbI_3$ lattice, preventing the reorganization both of the substructure of $[PbI6]^{4-}$ octahedra and of the Cs^+ ions that would be necessary for the transition to the δ-$CsPbI_3$ phase to take place. This reorganization would disrupt the epitaxial connection of the two lattices, creating a new interface charac-

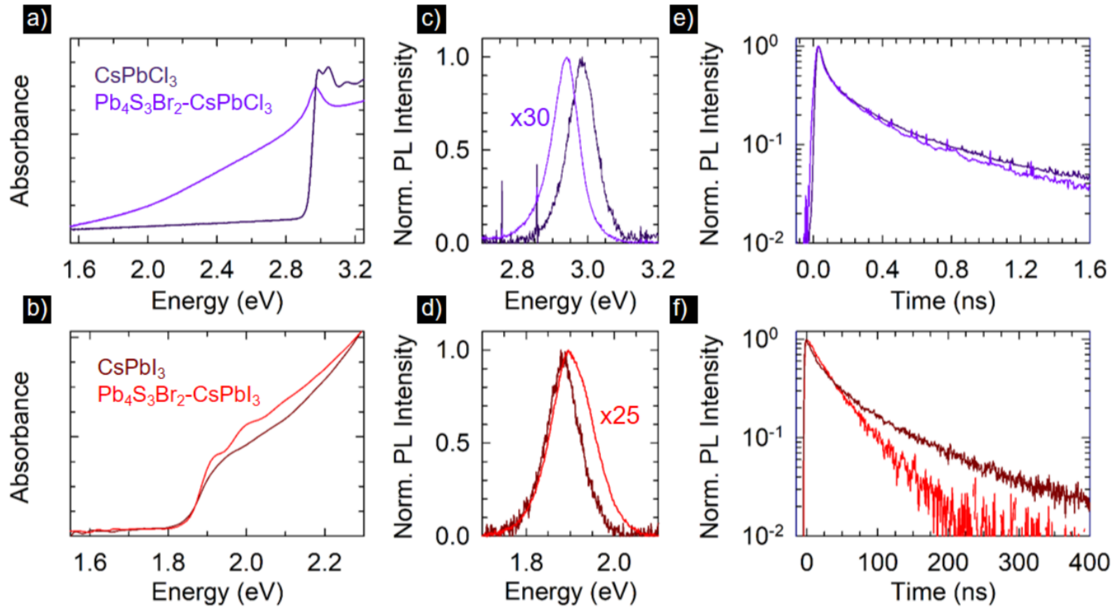

Figure 2.14: Absorption spectra of (a) $CsPbCl_3$ NCs and $CsPbCl_3$-$Pb_4Br_3S_2$ heterostructures (blue and purple, respectively) and (b) $CsPbI_3$ NCs and $CsPbI_3$-$Pb_4Br_3S_2$ heterostructures (dark and light red, respectively). PL spectra of (c) the chloride and (d) iodide-based samples. The spectra of the respective heterostructures have been multiplied as indicated. Normalized PL decay traces of (e) $CsPbCl_3$ NCs and $CsPbCl_3$-$Pb_4Br_3S_2$ heterostructures and (f) $CsPbI_3$ NCs and $CsPbI_3$-$Pb_4Br_3S_2$ heterostructures. The color scheme is the same for all panels. All measurements were performed on toluene dispersions at room temperature

terized by a much higher interfacial energy. Indeed, a hypothetical interface between the “yellowphase” δ-$CsPbI_3$ and $Pb_4S_3Br_2$ heterostructure is extremely unlikely to exist: our observations demonstrate that the interfaces that we observe experimentally are based on the sharing of a plane of lead ions which produces a square pattern, as shown in 2.9c. Such a squared plane of lead is not found in δ-$CsPbI_3$ in any orientation. Our conclusion is that the transformation of black $CsPbI_3$ into its yellow polymorph is impossible without disrupting the heterostructure.

2.2.8. Conclusions and future work

We have reported the synthesis of a series of $CsPbX_3$-Pb_4/Br_3S_2 heterostructures and have studied their growth mechanisms as well as their structural and optical features and modeled their overall electronic structure. One likely reason for the affinity of this specific chalcohalide with lead halide perovskites is that its sublattice of Pb cations is similar to that of the perovskite, so that epitaxial heterostructures can be grown. In the present synthesis scheme, the use of preformed, subnanometer $CsPbBr_3$ clusters appears to be a very valuable strategy for preparing the initial $CsPbBr_3$- $Pb_4Br_3S_2$ heterostructures, from which the other two have been derived by selective anion exchange in the perovskite domain. It is likely that this synthesis strategy can be extended to other nanocrystal heterostructures containing a halide perovskite domain, providing new ground for materials scientists to develop new types of nanoscale materials. On the other hand, it remains to be seen whether other chalcohalides, not based on Pb, can also form heterostructures with lead halide perovskites as easily as in the present case. One potential issue is that the introduction of another cation, instead of Pb^{2+}, in the reaction environment, might render the lead halide perovskite unstable. There is also ample space for improving the optical properties of the nanocrystals developed in this present work, and a finer control of the interfacial structure could unlock the full potential of these heterostructures for optoelectronic or photonic applications. Finally, the increased structural rigidity conferred to the perovskite lattice by virtue of an epitaxial interface with another material is a fascinating aspect of these nanostructures and can provide a possible avenue for mitigating the well-known instability of halide perovskites. As a final remark, I would like to underline the fact that even if at this point the poor optical performances limit their application, this study is still very relevant in the field of perovskite beacuse is one of the first case of successful shelling procedure, which is something that has to be achieved in order to use lead perovskites as stable and reliable technologies.

2.3. Cl-based Heterostructures: epitaxial synthesis as phase selective method

2.3.1. Introduction

We exploit the formation of epitaxial heterostructures as a reaction-directing step for the phase-selective synthesis of colloidal NCs, and we take advantage of this approach to further expand the family of lead chalcohalides we focus our attention on the lead sulfochlorides, demonstrating that the yet unknown Pb-S-Cl phase obtained through direct synthesis is $Pb_3S_2Cl_2$, whose structure, here identified as monoclinic, is a distorted version of the cubic $Pb_3Se_2Br_2$ prototype (Fig. 2.15, left reaction route)[76]. Conversely, the introduction of $CsPbCl_3$ nanoclusters in the reaction medium, under comparable reaction conditions, produces $Pb_4S_3Cl_2$/$CsPbCl_3$ heterostructures while suppressing the formation of $Pb_3S_2Cl_2$. Once the heterostructures are formed, the perovskite domain can be etched by exploiting the solubility of $CsPbCl_3$ in polar solvents, while leaving the $Pb_4S_3Cl_2$ domains intact. Hence, the use of $CsPbCl_3$ as a disposable template yields colloidally stable $Pb_4S_3Cl_2$ NCs that could not be obtained by direct synthesis due to the competitive nucleation of $Pb_3S_2Cl_2$ (Fig. 2.15, top-right reaction route).

The reason why $CsPbCl_3$ induces such phase selectivity lies in the fact that the structures of $Pb_3S_2Cl_2$ and $Pb_4S_3Cl_2$ are remarkably different [77, 78] to the point that only $Pb_4S_3Cl_2$ can match epitaxially with the $CsPbCl_3$ perovskite. Indeed, $Pb_4S_3Cl_2$ meets two strict structural constraints: i) the presence of a perovskite-like atomic plane [79], and ii) the continuity of the cationic subnetwork across the chalcohalide/perovskite interface [80]. Such conditions are not met for $Pb_3S_2Cl_2$, whose homogeneous nucleation is, therefore, less favorable than the heterogeneous nucleation of $Pb_4S_3Cl_2$ templated by the $CsPbCl_3$ perovskite.

Overall, our method effectively combines the concept of sacrificial substrates, such as the alkali halide single crystals used for the large-area synthesis of films and ultrathin materials[81, 82], with the phase-selection capabilities ensured by the epitaxial templating, all in the liquid phase.

2.3.2. Synthesis methods

We start by discussing the synthesis and structure solution of lead sulfochloride NCs prepared by homogenous nucleation, that is, in the absence of halide perovskites. We recently reported the synthesis of the same NCs by a different procedure[77], but in our

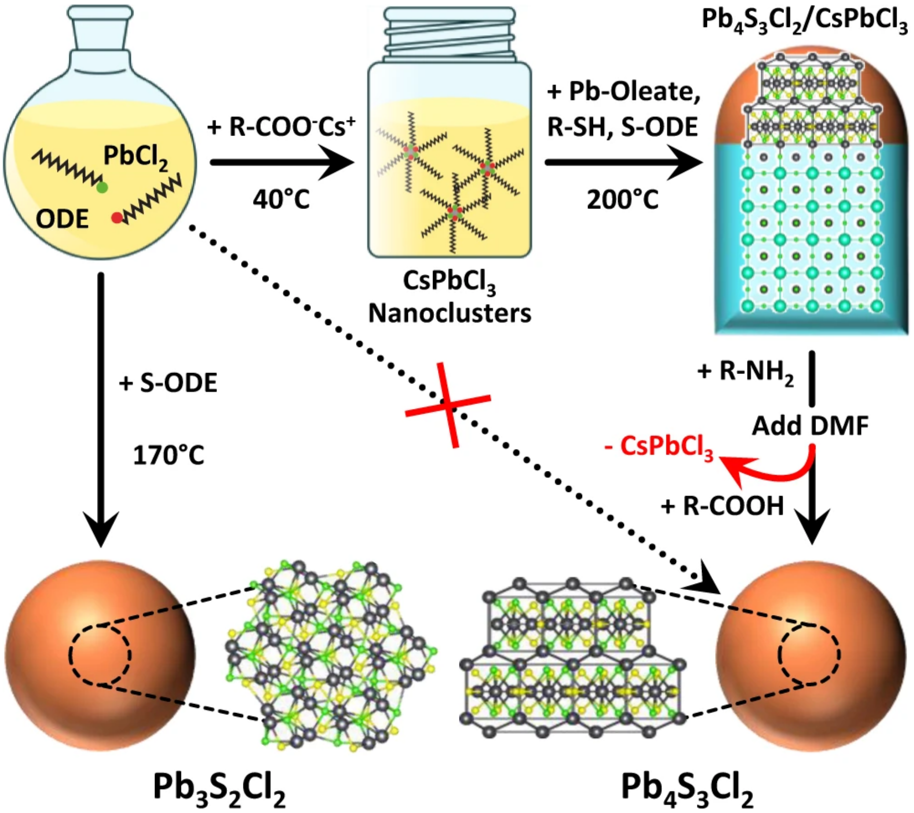

Figure 2.15: A solution of $PbCl_2$ reacts with sulfur dissolved in 1-octadecene (S-ODE) to form $Pb_3S_2Cl_2$ NCs. When reacted with Cs-oleate (R-COO-Cs^+) it produces instead $CsPbCl_3$ nanoclusters, that can be further reacted with Pb-oleate, S-ODE, and an alkyl thiol (R-SH) to form $Pb_4S_3Cl_2/CsPbCl_3$ heterostructures. The $CsPbCl_3$ domain can be then selectively etched by the sequential addition of oleylamine (R-NH2), dimethyl formamide (DMF), and oleic acid (R-COOH), yielding colloidally stable $Pb_4S_3Cl_2$ NCs that could not be obtained by direct synthesis. Atoms color code: Cs = cyan; Pb = gray; S=yellow; Cl = green.

previous work the small size of the particles and the heavy PbS contamination prevented us from determining the composition and crystal structure, which had therefore remained unknown to date. To solve the structure in the present work, we prepared large-size NCs via a two-step procedure, consisting of nucleation and seeded growth.

The synthesis yielded particles with a diameter of 29.5±2.0nm, as estimated by Transmission Electron Microscopy (TEM). Beyond this size the NCs became insoluble in the reaction medium, and the accretion process halted. The composition measured by SEM-EDX was Pb:S:Cl=3.2:1.8:2.0, which is compatible with our previously advanced hypothesis of a $Pb_3S_2Cl_2$ compound25. However, the X-Ray Powder Diffraction (XRPD) pattern could not be fitted based on the supposedly related $Pb_3Se_2Br_2$ cubic prototype [77], suggesting

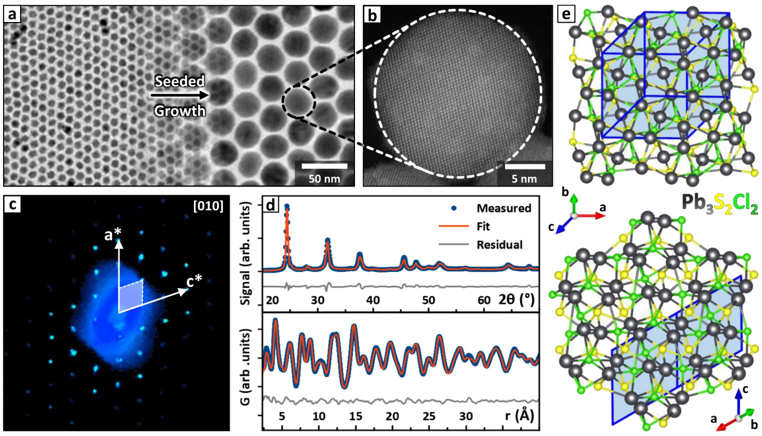

Figure 2.16: $Pb_3S_2Cl_2$ NCs as synthesized (left) and after the accretion process (right). b HAADF-STEM image of a $Pb_3S_2Cl_2$ NC. c [010] projection of the $Pb_3S_2Cl_2$ reciprocal lattice measured by 3D-ED, together with a representation of the reciprocal lattice axes and unit cell. d XRPD (top) and PDF (bottom) fits obtained by refining the $Pb_3S_2Cl_2$ structure in the Cc space group (experimental data = blue, fit curves = orange, residuals = gray). The XRPD profiles are plotted in the Cu-K 2 scale to ease the comparison with lab-grade diffraction patterns. e Two views of the Cc monoclinic $Pb_3S_2Cl_2$ structure are shown along the high symmetry directions of the corresponding pseudocubic cell ([100] top, [111] bottom). A projection of the monoclinic cell is overlaid in blue, and the directions of the corresponding lattice vectors are indicated by labeled arrows. Atoms color code: Pb = gray; S=yellow; Cl = green.

a different structure. Therefore, we exploited a combination of techniques to solve it. First, we performed a single-NC 3D Electron Diffraction (3D-ED) experiment to identify the unit cell parameters and a list of possible space groups (2.16c). For some of them we also produced ab-initio solutions; however, a definitive structural model could not be obtained due to the small size of the NCs, which made the integrated intensity of the diffraction spots inaccurate. Thus, we exploited the information from 3D-ED to repeat the ab-initio structure solution from XRPD data with the software EXPO201438, eventually obtaining a model close to the cubic $Pb_3Se_2Br_2$ in terms of connectivity, but with a lower symmetry. Finally, we refined this model in both reciprocal and direct spaces on data collected at the Brookhaven National Laboratory synchrotron, on setups optimized for XRPD and Pair Distribution Function (PDF) experiments respectively. The solution was found in the monoclinic Cc space group, capturing deviations from the $Pb_3Se_2Br_2$ cubic prototype that are likely due to the small ionic radii of S^{2-} and Cl^{-}. Density Functional Theory calculations confirmed that as a bulk crystal the monoclinic $Pb_3S_2Cl_2$ would be more stable than a hypothetical cubic polymorph by 164kcal/mol. The ionic

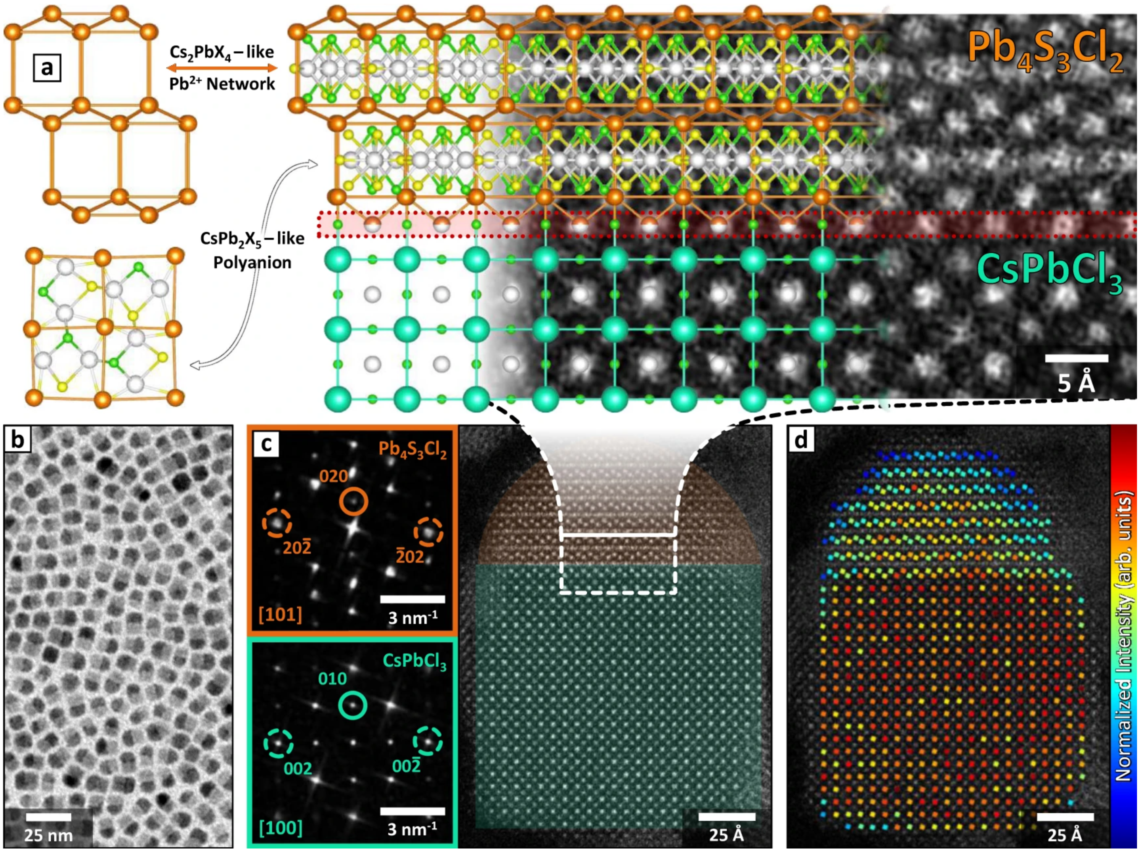

Figure 2.17: a) On the left, models of the Cs_2PbX_4 like Pb^{2+} subnetwork (orange Pb^{2+}) and of the $CsPb_2X_5$-like [Pb2S3Cl2]- polyanion (white Pb^{2+}, yellow S^{2-}, green Cl^-) found in $Pb_4S_3Cl_2$. On the right, model of the $Pb_4S_3Cl_2/CsPbCl_3$ epitaxial interface superimposed on a close-up view of c), highlighting the continuity of the Pb^{2+}/Cs^+ cationic subnetwork. The $Pb_4S_3Cl_2$ structure has been represented by adapting the $Pb_4S_3Br_2Br$ structure. Atoms color code: Cs = cyan; Pb = orange/white; S=yellow; Cl = green. b Low resolution TEM image of as-synthesized $Pb_4S_3Cl_2/CsPbCl_3$ heterostructures. c) HAADF-STEM image of a single $Pb_4S_3Cl_2/CsPbCl_3$ heterostructure. Insets: FFTs of the $Pb_4S_3Cl_2$ (top) and $CsPbCl_3$ (bottom) domains. The spots circled in a solid line correspond to planes parallel to the heterostructure interface and to each other; those circled in a dashed line are instead perpendicular to the interface and share similar periodicities, ensuring the match of the two lattices. d) Column intensity map of the Pb-containing columns in the perovskite phase and of the Pb columns in the Cs_2PbX_4like subnetwork of the $Pb_4S_3Cl_2$ domain. The color in the intensity map correlates with the total intensity scattered from the corresponding atomic column (red=higher intensity; blue = lower intensity)

radii are also likely to play a major role in favoring the $Pb_3S_2Cl_2$ phase over $Pb_4S_3Cl_2$ for free-standing lead sulfochloride NCs. Indeed, $Pb_3E_2X_2$appears to be favored if rE2-/rX-1

(Se^{2-}/Br^{-}=1.01; S^{2-}/Cl^{-}=1.02)31, while rE2-/rX-<1 favors $Pb_4E_3X_2$ (S^{2-}/Br- = 0.94; S^{2-}/I^{-}=0.84) [62, 67, 83].

Indeed, in both structures Pb^{2+} is surrounded by eight anions, and S^{2-} features a distorted octahedral coordination. Conversely, the coordination of the halide changes: in $Pb_3S_2Cl_2$ the smaller Cl^{-} ions share the same octahedral coordination as S^{2-}, while the larger Br- and I- ions in $Pb_4S_3X_2$ are surrounded by seven Pb^{2+} ions in a pentagonal bipyramidal configuration. The reason is likely that bulkier anions can accommodate an enlarged coordination environment. Interestingly, $Pb_3S_2Cl_2$ is the only lead chalcohalide where Cl^{-} is coordinated by an octahedron of Pb^{2+} ions. Such coordination has been recently proposed on the surface of PbS NCs synthesized in excess of $PbCl_2$ to account for the formation of a Cl^{-}rich shell that improves the optical properties [84–87] suggesting that these NCs might be passivated by a layer of some lead sulfochloride compound.

Our prior studies demonstrated that the lead sulfobromide $Pb_4S_3Br_2Br$ can grow epitaxially on lead halide perovskite domains [63], suggesting that other isostructural compounds, i.e.,$Pb_4S_3I_2$ and a hypothetical $Pb_4S_3Cl_2$, would do the same. Conversely, the $Pb_3S_2Cl_2$ structure we hereby solved is remarkably different from that of the $Pb_4S_3X_2$ compounds, to the point that the epitaxial compatibility with $CsPbX_3$ would be lost. This prompted us to think that the synthesis of a sulfochloride/perovskite heterostructure would produce domains of the yet unknown compound $Pb_4S_3Cl_2$ instead. Indeed, the $Pb_4S_3X_2/CsPbX_3$ match, regardless of the halide, is strictly structure specific. First, both the chalcohalide and the perovskite share a plane of Pb^{2+} ions arranged in a square grid, which serves as an interface between the two domains (in red in Fig. 2.17a, right)[79].

No such plane can be found in $Pb_3S_2Cl_2$. Moreover, $Pb_4S_3X_2$ shares deep similarities with some of the Cs-Pb-X phases and the heterostructures they form with $CsPbX_3$, which are easily overlooked at first sight. Indeed, the Cs-Pb-X compounds share a common cationic subnetwork of Cs+ ions, which in Cs-Pb-X/Cs-Pb-X heterostructures is preserved across the interface and ensures the lattice compatibility [80]. Remarkably, similar connectivity is found across the $Pb_4S_3X_2/CsPbX_3$ interface. Relevant examples for our discussion are the $CsPb_2X_5/CsPbX_3$ heterostructures. In $CsPb_2X_5$, the Cs+ subnetwork encloses layers of $[Pb_2X_5]^{-}$ bidimensional polyanions [80]. Remarkably, $Pb_4S_3X_2$ is almost isostructural to $CsPb_2X_5$, being formed by a Pb^{2+} subnetwork enclosing $[Pb_2S_3X_2]^{-}$ polyanions of identical geometry.

The only difference is the presence of an extra layer of Pb^{2+} ions in between each polyanion, that is needed to maintain the charge balance (Fig. 2.17a, left). This makes the Pb^{2+} subnetwork of $Pb_4S_3X_2$ resemble that of another Cs-Pb-X phase, namely Cs_2PbX_4.

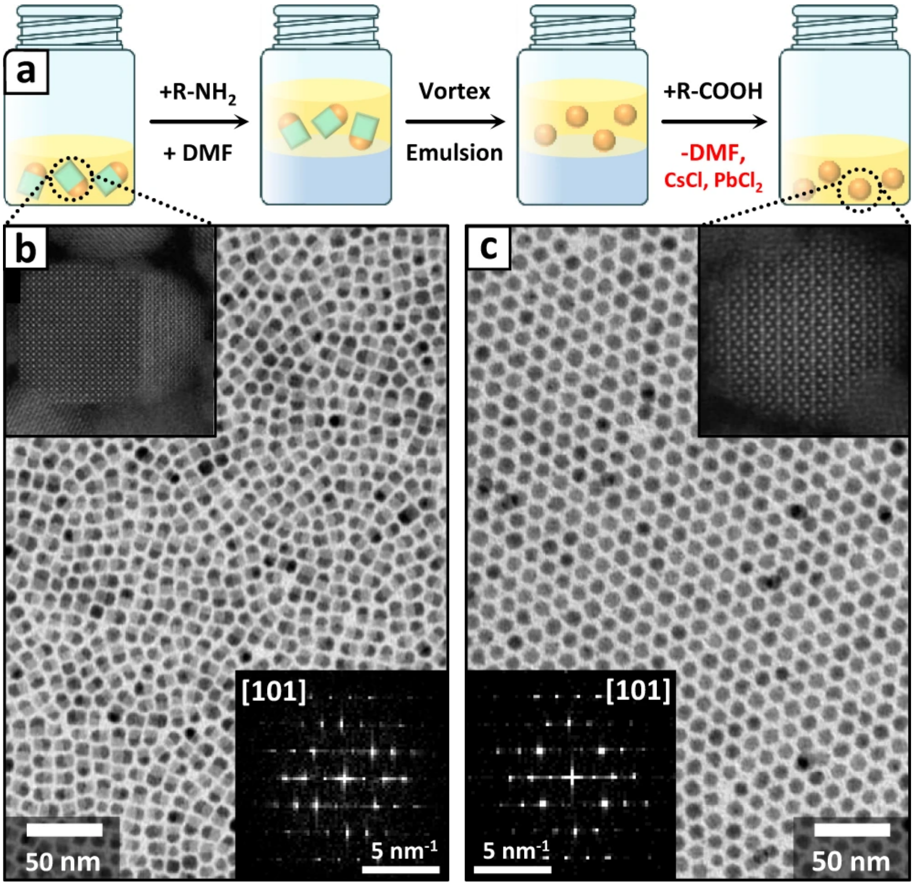

Figure 2.18: a) Scheme of the DMF-assisted etching procedure developed to transform the Pb4S3Cl2/CsPbCl3 heterostructures into $Pb_4S_3Cl_2$ NCs in the presence of surfactants (R-NH2=oleylamine, R-COOH=oleic acid). The cyan cubes and the orange spheres represent the $CsPbCl_3$ and the $Pb_4S_3Cl_2$ domains of the heterostructures, respectively. b TEM image of the starting heterostructures. The top inset shows an HAADF-STEM image of one heterostructure prior to the etching, while the bottom inset shows the FFT of the chalcohalide domain of the same image. c) TEM image of the etched NCs. The top inset shows an HAADF-STEM image of one NC after the etching, while the bottom inset shows the FFT of the same image. The two FFTs demonstrate that the $Pb_4S_3Cl_2$ domains retain the same crystal structure before and after the etching procedure

Consequently, the cationic subnetwork of $Pb_4S_3X_2$ is similar to that found in Cs-Pb-X compounds and can find its natural prosecution in the $CsPbX_3$ perovskite (Fig. 2.17a, right), ensuring the stability of the interface and remarking the pivotal role of ionic sub-networks in the formation of colloidal heterostructures

To test whether the natural affinity of the $Pb_4S_3X_2$ phases for lead halide perovskites would lead to the formation of $Pb_4S_3Cl_2$, we adapted our previously reported method to attempt the synthesis of $Pb_4S_3Cl_2/CsPbCl_3$ heterostructures26. In the first step of the procedure, $CsPbCl_3$ nanoclusters, prepared separately, were reacted with elemental sulfur in the presence of lead oleate and dodecanethiol at 200 °C, indeed producing heterostructures. The resulting particles were recovered through antisolvent precipitation, and then treated with a solution of $PbCl_2$, oleylamine, and oleic acid to restore their colloidal stability. he heterostructures were homogeneous in terms of size and shape (Fig. 2.17b), and no single-phase perovskite or sulfochloride NCs were observed.

High-Angle Annular Dark-Field Scanning TEM (HAADF-STEM) showed that the heterostructures were composed of two highly crystalline domains jointed along a flat interface spanning across the entire nanoparticle (Fig. 2.17a, c). As expected, the fast Fourier transform (FFT) of the HAADF-STEM image revealed that the $CsPbCl_3$ domain matches with the perovskite structure, while that of the lead sulfochloride domain is incompatible with $Pb_3S_2Cl_2$. Instead, the unit cell parameters and the overall FFT symmetry match with what is expected for a $Pb_4S_3X_2$ domain based on our previous observations on $Pb_4S_3Br_2Br/CsPbX_3$ heterostructures (insets of Fig. 2.17c)[79]. Such phase selectivity was granted by the transformation of $CsPbCl_3$ nanoclusters into NCs during the early stages of the reaction. The perovskite NCs then acted as phase-selective heterogeneous nucleation seeds for $Pb_4S_3Cl_2$, providing a significant advantage over the homogeneous nucleation of $Pb_3S_2Cl_2$, which was indeed suppressed.

The predicted structure of the $Pb_4S_3Cl_2/CsPbCl_3$ interface, superimposed in Fig. 2.17a to a high-resolution HAADF-STEM image of the heterostructure, was further confirmed by highlighting the Pb-containing atomic columns involved in the Pb^{2+} cationic subnetwork through the quantitative analysis of HAADF-STEM images (Fig. 2.17d). Indeed, it is worth noting that a prosecution of the chalcohalide-Pb^{2+} subnetwork, identified in Fig. 2.17a with the perovskite-Cs+ subnetwork in analogy with the $CsPb_2X_5/CsPbX_3$ heterostructures, can also be found in the Pb^{2+} subnetwork of the perovskite domain, as it shares the same symmetry as the Cs+ one

Our templated synthesis approach could be pushed a step further as we took advantage of the solubility of $CsPbCl_3$ in polar solvents to selectively etch the perovskite domains and recover phase-pure $Pb_4S_3Cl_2$ NCs (Fig. 2.17). Briefly, the heterostructures dispersed in hexane were first treated with oleylamine to improve the colloidal stability of the etched NCs in nonpolar media. Then, we added to the dispersion an equal volume of dimethylformamide (DMF), and the resulting mixture was vortexed for 30s, forming an emulsion. After its complete separation, DMF was removed, and predried oleic acid was introduced in the NCs hexane dispersion. Subsequently, the particles were recovered through antisolvent precipitation followed by a centrifugation, and redispersed in toluene for further use. The procedure yielded remarkably uniform $Pb_4S_3Cl_2$ NCs, whose structure was confirmed via high-resolution HAADF-STEM imaging and analysis of the lattice by means of FFTs. Interestingly, the NCs appeared to be sphere-shaped despite the original chalcohalide domains in the heterostructures being hemispherical. We attribute this change of morphology to the need of lowering the surface energy of the extended and non-passivated facet left after the dissolution of the perovskite. It is likely that the excess ions released by the etching process will recrystallize on the chalcohalide domains, thus reshaping them into a more stable spherical morphology

2.3.3. Optoelectronic properties of lead sulfochloride NCs

Obtaining both $Pb_3S_2Cl_2$ and $Pb_4S_3Cl_2$ NCs, and the latter both in the form of free-standing NCs and heterostructures with $CsPbCl_3$, gave us the opportunity to investigate the impact of stoichiometry, structure, and presence of a heterojunction on the optoelectronic properties of lead sulfochlorides. Figure 2.19 summarizes the experimental results, along with data from DFT calculations. The free-standing $Pb_3S_2Cl_2$ and $Pb_4S_3Cl_2$ NCs exhibited basically overlapping and featureless absorption spectra, with onset at ~1.8eV (~690nm, Fig. 2.19a, solid blue and orange plots). The Tauc plot analysis suggested an indirect band gap of ~1.8eV in both cases, in agreement with the DFT predictions. This is in stark contrast with the direct bandgap observed for lead chalcogenides (PbE) and many lead halides (e.g., $CsPbX_3$), remarking that the electronic properties of lead chalcohalides are not straightforwardly related to those of chemically similar compounds. A comparable absorption profile was found in the heterostructures spectrum, combined with the blunt absorption edge of the direct-gap $CsPbCl_3$ domain (~3.1eV=400nm [44, 88], Fig. 2.19a, solid black plot). Such edge was instead sharp for free-standing $CsPbCl_3$ NCs (Fig. 2.19a, solid cyan plot), suggesting an intimate electronic connection between the two domains in the heterostructures. This was further supported by the almost complete suppression of the $CsPbCl_3$ photoluminescence (PL) when the perovskite domain was involved in the heterojunction (Fig. 2.19b, inset).

DFT calculations suggested that the cause for the PL quenching was the nearly type-I band alignment between $Pb_4S_3Cl_2$ and $CsPbCl_3$ (Fig. 2.19e. Interestingly, this contrasts with the structurally equivalent $Pb_4S_3Br_2Br/CsPbBr_3$ heterostructures investigated in our previous work, which were instead identified as quasi-type-II junctions. Indeed, the molecular orbitals corresponding to the band edge states of the heterostructures are strongly localized on the sulfochloride domain (Fig. 2.19f). It is worth noting that the predicted type-I alignment should promote the migration of photocarriers into the sulfochloride domain of the heterostructure. Indeed, the decay of the barely detectable PL of $CsPbCl_3$

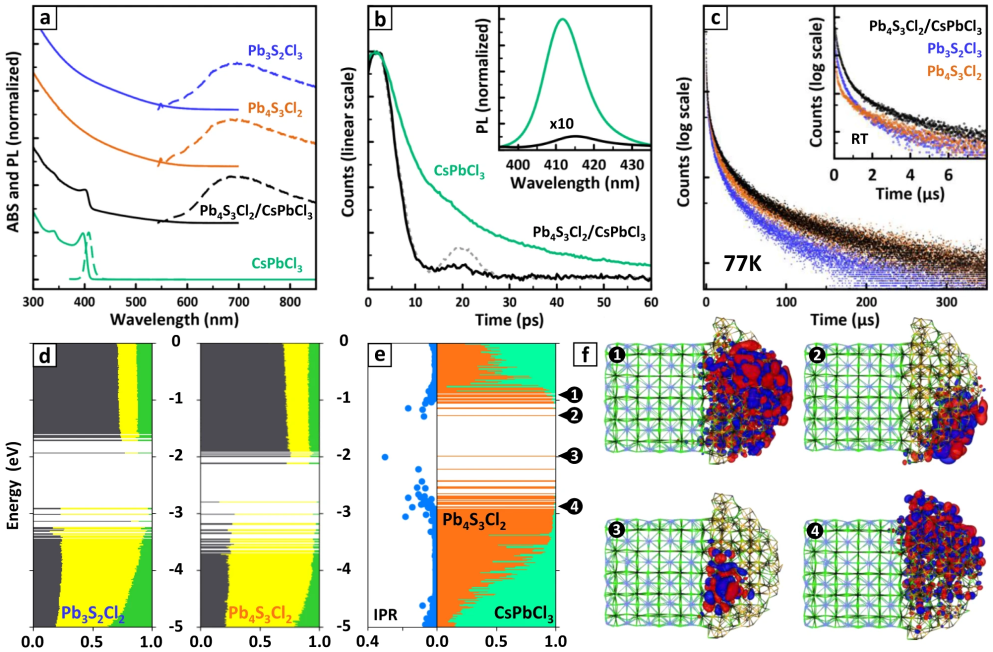

Figure 2.19: Absorption (ABS, solid lines) and photoluminescence (PL, dashed lines) spectra of free-standing $Pb_3S_2Cl_2$, $Pb_4S_3Cl_2$, $CsPbCl_3$ NCs and of $Pb_4S_3Cl_2/CsPbCl_3$ heterostructures. The $CsPbCl_3$ NCs were prepared for comparison purposes by heating the $CsPbCl_3$ precursor nanoclusters. b) Decay curves of the ~410nm PL from $CsPbCl_3$ as free-standing NCs and in the $Pb_4S_3Cl_2/CsPbCl_3$ heterostructures. The dashed gray line is the time response of the experimental setup. Inset: PL spectra of $CsPbCl_3$ as free-standing NCs and in the heterostructures, showing a drastic quenching in the latter case. The PL intensity of the heterostructures is multiplied x10 to make it more visible. n. c) Decay curves of the ~1.8eV (~690nm) emission of the three samples at room temperature and at 77K (inset). Color code: cyan = $CsPbCl_3$, blue = $Pb_4S_3Cl_2$, orange = $Pb_3S_2Cl_2$, black = $Pb_4S_3Cl_2/CsPbCl_3$ heterostructures. d Electronic structure of free-standing $Pb_3S_2Cl_2$ (left) and $Pb_4S_3Cl_2$ (right) NC models computed at the DFT/PBE level of theory. The color code indicates the elemental contribution to each molecular orbital (Pb=gray; S=yellow; Cl = green). e) Electronic structure of the $Pb_4S_3Cl_2/CsPbCl_3$ heterostructure model computed at the DFT/PBE level of theory, color coded by domain ($Pb_4S_3Cl_2$=orange; $CsPbCl_3$=cyan). The Inverse Participation Ratio (IPR, left panel) quantifies the degree of localization of a state (1/Natoms=completely delocalized; 1 = localized on one single atom). f) Representation of molecular orbitals corresponding to band edge delocalized states (1,4) and to band edge trap states (2,3). In both cases, the band edge states are localized on the $Pb_4S_3Cl_2$ domain

in the heterostructures was strongly accelerated if compared with that of free-standing $CsPbCl_3$ NCs (τavg ~8ps vs ~18ps, Fig. 2.19b).

Owing to the relaxation of the momentum conservation at the nanoscale, both the free-standing sulfochlorides and the heterostructures exhibited a broad PL peak at ∼1.8eV (∼690nm, see fig. 2.19a, dashed lines), indicating in all the cases a sulfochloride band edge emission. Such emission was negligible at room temperature (PLQYlesst then 1%) due to the efficient thermal quenching. However, lowering the temperature to 77K resulted in a ∼100-fold intensification of the PL, accompanied in the case of heterostructures by a brightening of the residual, yet still negligible, $CsPbCl_3$ emission. In all three cases, the PL kinetics of the lead chalcohalides was markedly non-exponential, with a dominant sub-microsecond drop followed by a slower decay (Fig. 2.19c). The process was slightly slower in the heterostructures with respect to both free-standing $Pb_3S_2Cl_2$ and $Pb_4S_3Cl_2$ NCs, suggesting that the $CsPbCl_3$ domain might suppress some trapping losses by passivating part of the sulfochloride domain surface. This is also consistent with our observation of a more intense PL. At low temperatures, all the PL decays became substantially longer. Fitting the dataset with an Arrhenius function yielded for all the samples an activation energy of ∼15meV. Remarkably, the spectral shape of all samples followed a nearly identical trend with the temperature, showing a progressive shift to ∼1.5eV (∼827nm) and a band narrowing, further corroborating the strong similarities between the optoelectronic properties of these three systems (see figure 2.20)

In general, our analysis indicates that the properties of lead sulfochlorides are largely independent of both stoichiometry and structure. This completes our preliminary observations on $Pb_4S_3Br_2Br$ and$Pb_4S_3I_2$ NCs, that shared nearly identical absorption spectra despite containing different halides [77]. We rationalized such behavior as a consequence of two factors. First, in these materials the band edge states feature a prominent participation of Pb^{2+} and S^{2-}, while the halides mostly contribute to states buried deep in the valence band, making the electronic properties almost halide-insensitive. Second, regardless of the structure of the specific chalcohalide, the geometry and connectivity of the coordination polyhedra surrounding both Pb^{2+} and S^{2-} is the same, making the electronic properties basically structure-insensitive.

2.3.4. Conclusions and future works

We have exploited the epitaxial templating effect of $CsPbCl_3$ to control the synthesis of lead sulfohalide NCs through the formation of $Pb_4S_3Cl_2/CsPbCl_3$ heterostructures. Indeed, while a direct synthesis approach (i.e., in the absence of $CsPbCl_3$ acting as a template) yielded $Pb_3S_2Cl_2$ NCs, only the selective etching of the heterostructures perovskite domain allowed us to recover free-standing $Pb_4S_3Cl_2$ NCs. This ultimately means that we could select the reaction product between two competing phases, a problem of great

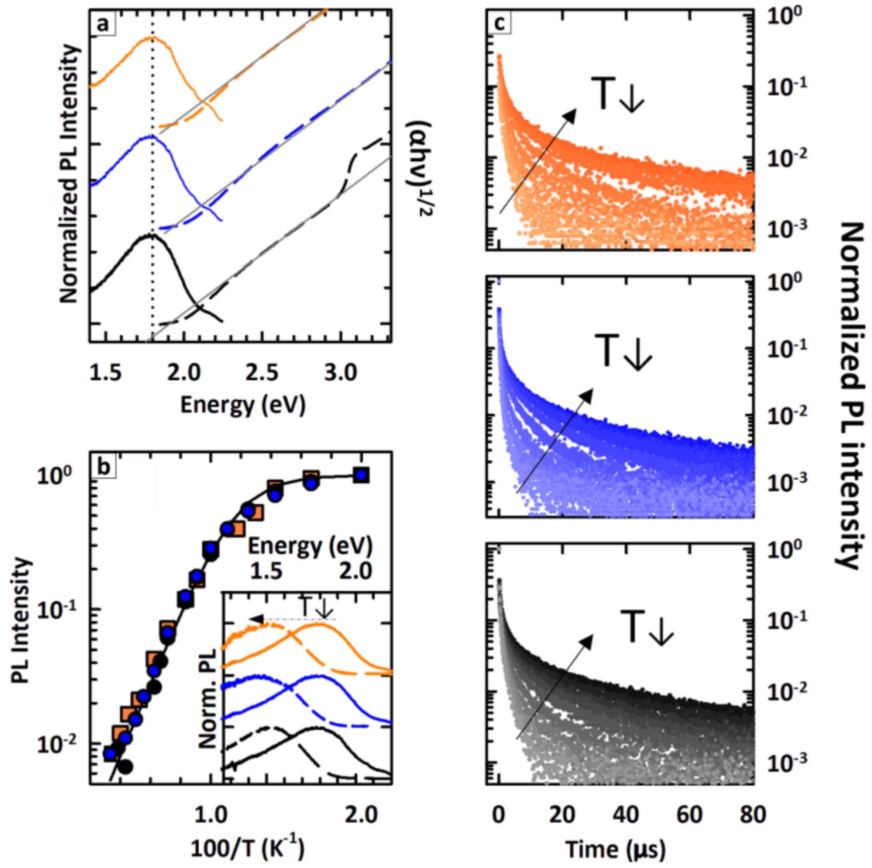

Figure 2.20: a) Photoluminescence spectra (solid lines) and Tauc plot analysis (dashed lines) of the absorption spectra of $Pb_3S_2Cl_2$ NCs (blue), $Pb_4S_3Cl_2$ NCs (orange) and $Pb_4S_3Cl_2/CsPbCl_3$ heterostructures (black), superimposed to the corresponding fit lines(grey). The analysis highlights that all the three materials are characterized by comparable band gaps and emissions. b) Temperature dependence of the photoluminescence intensity of $Pb_3S_2Cl_2$ NCs (blue), $Pb_4S_3Cl_2$ NCs (orange) and $Pb_4S_3Cl_2/CsPbCl_3$ heterostructures (black). Inset: temperaturedependent spectral shift of the photoluminescence spectra, measured at 300K (solid lines) and at 77K (dashed lines). c) Time resolved photoluminescence spectra as a function of temperature for the three samples. Darker lines indicate lower temperatures, lighter lines higher temperatures.

relevance in the synthesis of colloidal inorganic nanomaterials. Both the obtained lead sulfochlorides shared remarkably similar optoelectronic properties. This, combined with our previous observation on bromine- and iodine-based sulfohalides25, suggests that lead sulfohalide compounds are mostly stoichiometry- and structure-insensitive. Interestingly, the discovery of the $Pb_3S_2Cl_2$ structure demonstrates that Cl^- in lead chalcohalides can be coordinated by an octahedron of Pb^{2+} ions, differently from Br- and I-. This supports the recent observations of a PbClx-rich shell on the surface of PbS NCs synthesized using

$PbCl_2$ as a precursor, a condition that is remarkably similar to our synthetic protocol and might indeed lead to the formation of a lead sulfochloride surface layer.

We remark that our use of perovskite NCs as disposable and phase-selective epitaxial templates parallels that of reaction-directing groups in traditional organic chemistry and catalysis, and allowed us to design the phase-selective synthesis of two yet unknown materials ($Pb_3S_2Cl_2$ and $Pb_4S_3Cl_2$) based on structural considerations only. Such an approach to a deterministic synthesis of NCs may be extended to other phases with known or predictable epitaxial relations, taking advantage of the vast library of already reported nanomaterials as starting templates. For example, in the field of chalcohalides it might lead to yet unknown selenium- and tellurium-based materials, or even to compounds where the halide is replaced by pseudohalide ions (e.g., CN^- and SCN^-). In conclusion, we envision that our phase-selective templating approach will open new routes for the colloidal syntheses of nanomaterials which are now hindered by an excessive activation energy for the homogeneous nucleation, or by the competitive formation of undesired phases.

3 | Towards novel Pb-free nanocrystals: the case of Cesium Manganese Bromides

In this chapter, I will discuss another approach to the research of novel architectures for luminescence NPs. Instead of focusing on refining the design of already existing and well known LHP nanocrystals, here we discuss some alternatives which do not use Pb. Lead-free nanocrystals are in fact highly desirable due to the high toxicity and enviroment pollution of such element. One of the novel NPs alternative to LHP and which present promising optical prpoperties has been studied and will be presented.

3.1. Introduction and state of art

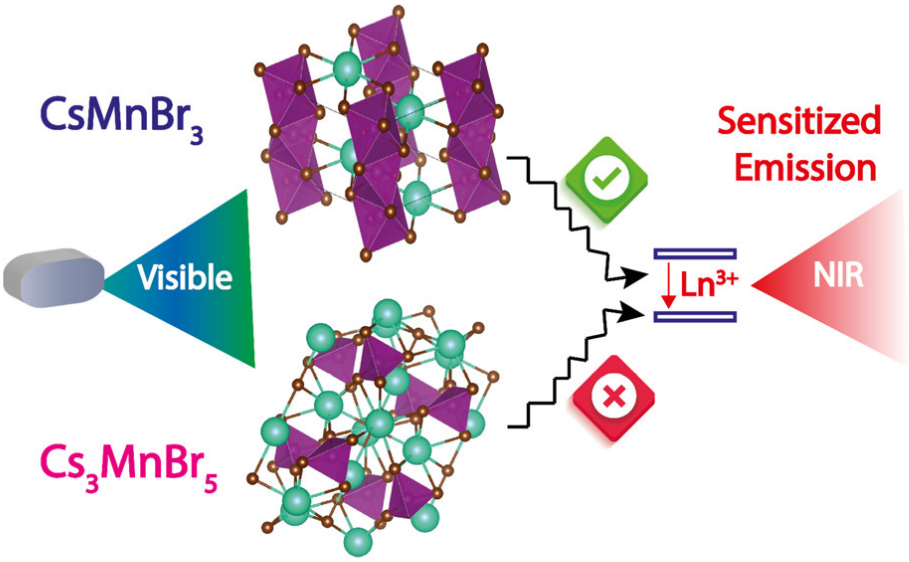

Figure 3.1: Scheme of Downshifting process using Mn Based perovskites

Downshifting luminescence is a single-photon process that converts absorbed high-energy photons to lowenergy ones,1 and it is employed in a broad range of applications including solar cells,[89–91] luminescent solar concentrators, [92] near-infrared light emitting diodes (NIR LEDs),[93] bioimaging,[94–96] and biosensors[97, 98]. A common strategy for downshifting luminescence is based on a trivalent lanthanide (Ln^{3+}) ion as the emission center and a sensitizer as the light absorption center. Lanthanide ions have several interesting properties as potential sensitizers, such as ladderlike electronic states and long radiative lifetimes (10 μs-10 ms),[99, 100] which can promote luminescence conversion.

However, their progress as downshifters is limited since Ln^{3+} ions (e.g., Yb^{3+}, Er^{3+}, Tm^{3+}, Nd^{3+} and Ho^{3+}) have narrow absorption widths as well as very small absorption cross sections due to their electric-dipole-forbidden 4f→4f transitions [101, 102]. Although traditional semiconductor nanocrystals (NCs) such as CdSe,[103, 104] InP,[105, 106] and Ag_2Se[107] have a high absorption cross section and can be used as host materials, their covalently bonded rigid lattices complicate the doping process with lanthanide ions[99, 108]. Instead, halide perovskites are ideal for substitutional doping due to the softness and strong ionicity of their lattice, and additionally they offer very high absorption cross sections[90, 93, 109, 110]. Various reports have shown that in lead halide perovskites a downshifted luminescence in the visible and infrared spectral range can be achieved through doping with divalent cations (for instance, Cd^{2+}, Mn^{2+}),[111] trivalent cations (Ln^{3+}),[109, 112, 113] or a combination [114]. Yet, the toxicity and stability issues of lead-based perovskites are a strong drive toward alternative metal halides,[115–117] and several Pb-free double perovskites (e.g., $Cs_2AgInCl_6$, [118] Cs_2AgBiX_6 (X = Cl, Br),[119] and $Cs_3Bi_2Br_9$ 3[120]) have been synthesized and tested as hosts. Furthermore, most of these materials absorb only in the blue visible range (<500 nm)[118, 119]. Therefore, it is highly desirable to increase absorptivity and overall broadening of the absorption spectrum of the downshifter to the visible spectral range. The recently reported cesium manganese bromide NCs offer several appealing properties and hold great potential as sensitizers[121, 122]. The advantages of cesium manganese bromide NCs include (i) a broad absorption spectrum covering the visible spectral range (ii) high absorption coefficients (ϵ=544 nm = 83.6 M-1 ·cm-1 for $CsMnBr_3$, and (iii) significantly reduced toxicity compared to Pb-based compounds. Also, recent works have shown that the luminescence of these materials can be tuned by changing the coordination geometry of the Mn^{2+} ions since, depending on whether such coordination is tetrahedral or octahedral, the emission is either in the green or in the red spectral range, respectively[123]. Nonetheless, it is significantly challenging to control and engineer the colloidal synthesis of cesium manganese bromide NCs due to the presence of energetically similar competing phases [121] Herein, we report phase-selective syntheses of colloidal Cs_3MnBr_5 NCs and $CsMnBr_3$ NCs exhibiting green and red luminescence, respectively. We then attempt to dope both phases with various NIR-emitting lanthanide ions. Interestingly, our results show that $CsMnBr_3$ can be doped successfully with Nd^{3+}, Er^{3+}, Tm^{3+}, and Yb^{3+}, while Cs_3MnBr_5 is inert toward all dopants due to the difficulty of lanthanides incorporation in tetrahedrally coordinated environments. Lanthanide-doped $CsMnBr_3$ NCs demonstrate emission in the NIR-I (∼800-900 nm) [123] and NIR-II (1000-1700 nm)[124] spectral regions. These findings agree with our computational analysis on both cesium manganese bromide systems. Our study demonstrates a versatile sensitizer for downshifting luminescence of lanthanides, and it provides new opportunities for applications of lanthanide-doped nanosystems.

3.2. Synthesis and Optical Characterization of Cs_3MnBr_5 and $CsMnBr_3$ nanocrystals

As mentioned earlier, the synthesis of phase-pure cesium manganese bromide-based NCs is more challenging than that of classical lead halide perovskite NCs due to the presence of different competing phases that can be easily formed in the CsBr-MnBr2 phase diagram, such as $CsMnBr_3$, Cs_3MnBr_5, and Cs_2MnBr_4. 46 In a recent study, $CsMnBr_3$ and Cs_3MnBr_5 NCs were synthesized in a Schlenk line system using the highly reactive trimethylbromosilane as the bromide source [123] As a safer synthesis route, we prepared here Cs_3MnBr_5 and $CsMnBr_3$ NCs using a modified version of our previously developed benzoyl halide-based synthesis approach, which enables independent tunability of the concentration of metal cations, halide ions, and surfactants [125–127]. Briefly, NCs were synthesized by injecting benzoyl bromide into a solution of cesium and manganese oleates in the presence of oleylamine (see scheme in Figure 3.2a).

We found that $CsMnBr_3$ and Cs_3MnBr_5 NCs can be separately prepared, each with high phase purity, under optimized sets of reaction conditions. X-ray diffraction (XRD) analysis indicates that $CsMnBr_3$ NCs have a hexagonal crystal structure (P63/mmc space group) formed by chains of face-sharing [MnBr6] octahedra that are chargebalanced by cesium ions along the c-axis (Figure 3.2a). The Cs_3MnBr_5 NCs has instead a tetragonal crystal structure formed by isolated [MnBr4] tetrahedra (each Mn^{2+} ion is bound in a tetrahedral configuration to four Br- ions) and stabilized by cesium ions (I4/mcm space group, Figure 3.2a). These results are consistent with existing literature on bulk $CsMnBr_3$ [128, 129]and Cs_3MnBr_5 [130] crystals. According to transmission electron microscopy (TEM) analysis, the NCs has a mean size of 78 ± 14 nm (Figure 1b, inset) and 33 ± 7 nm (Figure 3.2c, inset) for Cs_3MnBr_5 and $CsMnBr_3$ NCs, respectively. The much larger size of the Cs_3MnBr_5 NCs can be attributed to the higher injection temperature

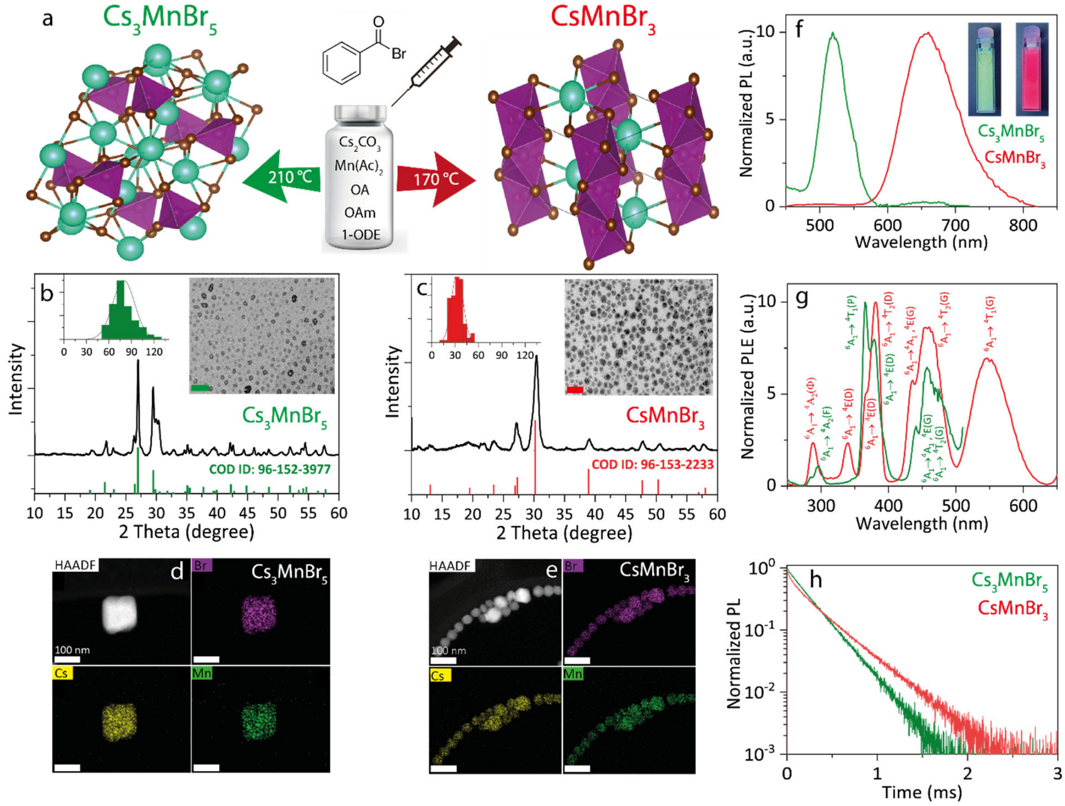

Figure 3.2: Structural and optical analyses of CsMnBr$_3$ and Cs$_3$MnBr$_5$ NCs. (a) Schematic representation of the synthesis procedure and standard depiction (Cs = green, Mn = violet, and Br = brown) of the Cs$_3$MnBr$_5$ andCsMnBr$_3$ structures. (b) XRD pattern and reference pattern COD ID: 96-152-3977 of the Cs$_3$MnBr$_5$ NCs (right inset: TEM image, scale bar = 400 nm; left inset: particle size distribution). (c) XRD pattern and reference pattern COD ID: 96-153-2233 of theCsMnBr$_3$ NCs (right inset: TEM image, scale bar = 100 nm; left inset: particle size distribution). HAADF STEM image and EDS maps of (d) Cs$_3$MnBr$_5$ and (e)CsMnBr$_3$ NCs. (f) Photoluminescence (PL) spectra of the Cs$_3$MnBr$_5$ (green, λexc = 380 nm) andCsMnBr$_3$ (red, λexc = 380 nm) NCs dispersed in toluene. Inset: Photographs of the Cs$_3$MnBr$_5$ andCsMnBr$_3$ NC solutions under UV light. (g) Photoluminescence excitation (PLE) spectra of the Cs$_3$MnBr$_5$ (green, em = 522 nm) andCsMnBr$_3$ (red, em = 661 nm) NCs dispersed in tolouene. (h) PL time decay of Cs$_3$MnBr$_5$ (green, em = 522 nm) andCsMnBr$_3$ (red, em = 661 nm) NCs dispersed in toluene.

(210 °C) required in their synthesis compared to the CsMnBr$_3$ NCs case (170 °C). HAADF STEM images in combination with EDS mapping confirm compatible compositions for Cs$_3$MnBr$_5$ (Figure 3.2d) and CsMnBr$_3$ NCs (Figure 3.2e). The optical properties and electronic structure of manganese halides are due to electronic transitions localized in the

[MnBrx] (x = 4, 6) polyhedra that are dominated by d-d transitions within the Mn cations mixed with some orbital contribution from the nearby 4p of the Br ions. These excitations are typically spin and parity forbidden;[131] nevertheless, exchange coupling as well as spin-orbit coupling are responsible for the relaxation of spin selection rules in antiferromagnetic manganese halides.[131]. These optical properties can be tuned by changing the coordination geometry around the Mn^{2+} ions and the Mn-Mn distance[132, 133]. In particular, tetrahedrally coordinated Mn^{2+} exhibits green emission [124], while octahedrally coordinated Mn^{2+} exhibits red emission[134, 135]. We studied the steady-state optical properties in colloidal dispersions to reconfirm the presence of Cs_3MnBr_5 and $CsMnBr_3$ NCs. Cs_3MnBr_5 NCs features green emission centered at 522 nm, while the $CsMnBr_3$ NCs shows red emission centered at 661 nm (Figure 3.2f), and both phases show photoluminescence quantum yields (PLQYs) in the range of 33 ± 4%, which decreases to 8 ± 2% after storage in the ambient air for 10 days (relative humidity 40%). Importantly, the Cs_3MnBr_5 NC solution shows only negligible emission in the red spectral region compared to the literature. In fact, the only reported Cs_3MnBr_5 NCs' photoluminescence to date had two intense emissions around 520 and 660 nm [123], indicating the actual presence of both Cs_3MnBr_5 and CsMnBr phases in that sample. Figure 3.2g displays the photoluminescence excitation (PLE) spectra, in which the d-d transition of the Mn^{2+} ion in d5 configuration and different excitation states funnel the excitation to the same transition (6 A1→4 T1(G)) for both tetrahedral Cs_3MnBr_5 [124] and octahedral $CsMnBr_3$ [134, 135] NCs (Figure 3.2g). The PL time decays of $CsMnBr_3$ and Cs_3MnBr_5 NC solutions reveal a single exponential kinetics at room temperature. The Cs_3MnBr_5 NCs, emitting at 522 nm, decay faster ($\tau = 170$ μs) than the $CsMnBr_3$ NCs ($\tau = 235$ μs), the latter emitting at 661 nm, which is in agreement with the literature (Figure 3.2h) [123].Interestingly, no excitation dependent PL decay lifetime has been observed for $CsMnBr_3$ and Cs_3MnBr_5 NCs (excitation at 532 nm vs 355 nm).

3.3. Vis-to-NIR Downshifting using Ln^{3+}-doped $CsMnBr_3$ NCs

Sensitizers hosting different types of lanthanides and efficiently absorbing in the visible spectral range are highly desirable for downshifting applications [105, 136]. This motivated us to investigate the performance of both $CsMnBr_3$ and Cs_3MnBr_5 NCs as sensitizers. For that, we attempted doping with different lanthanide dopants, including Yb^{3+}, Nd^{3+}, Tm^{3+}, and Er^{3+}, via a facile synthesis route, on both NC systems. Energy-dispersive X-ray spectroscopy (EDS) revealed unsuccessful doping of the Cs_3MnBr_5 NCs.

Dopant	Emission Wavelenght (nm)	Lifetime τ	NIR PLQY (%)
Nd3+ doped$CsMnBr_3$ NCs	895	810 μs	0.41
Tm3+ doped$CsMnBr_3$ NCs	1230	1.4 ms	0.63
Yb3+ doped$CsMnBr_3$ NCs	990	700 μs	1.1
Er3+ doped$CsMnBr_3$ NCs	1545	.	0.24

Table 3.1: Table with the result of optical characterization of all doped systems

The apparently ineffective doping of Cs_3MnBr_5 NCs with lanthanides might stem from the difficulty to incorporate lanthanides (preferring CN 662-64) in a tetrahedrally coordinated environment or by the lack of a favorable energy alignment between the dopant and the Mn matrix [99]. On the other hand, $CsMnBr_3$ NCs were successfully doped by Yb^{3+}, Nd^{3+}, Tm^{3+}, and Er^{3+}. However, for the case of $CsMnBr_3$, two Ln^{3+} ions can, in principle, substitute three Mn^{2+} ions, generating a cation vacancy (VMn),65 as was reported for $CsMnCl_3$ [137, 138] and $CsMnX_3$. 2,3,26,68-72 The higher content of Nd (1.22 at.%) compared to Yb (1.19 at.%), Er (1.02 at.%), and Tm (0.89 at. %) that we could introduce in the NCs can be explained by the lower ionic radius mismatch between Mn^{2+} (97 ppm73) and Nd^{3+} (98.3 ppm74) compared to Er^{3+} (89 ppm74), Tm^{3+} (87 ppm75), and Yb^{3+} (86 ppm76). In addition, XRD patterns of lanthanide-doped $CsMnBr_3$ NCs indicate no extra diffraction peaks nor any notable shift compared to undoped $CsMnBr_3$ NCs (Figure 2l) due to the low amount of lanthanides (<1.5 at.%) that could be introduced in the lattice, as reported for Erdoped [109] and Yb-doped [139] CsPbCl3 NCs. We observed NIR emission features via excitation in the visible spectral range (550 nm) for $CsMnBr_3$ NCs doped with Yb^{3+}, Nd^{3+}, Tm^{3+}, and Er^{3+} (Figure 3.3a-d) having NIR PLQYs in the range of 0.24-1.1% (table 3.1)

Furthermore, the lanthanide-doped $CsMnBr_3$ NCs have the same PLE profile as the undoped $CsMnBr_3$ NCs toward all types of dopants (Figure 3.3e-h). This suggests that lanthanide NIR emission is triggered by excitation of the host $CsMnBr_3$ NCs. This phenomenon is in agreement with the efficient energy transfer from Mn^{2+} commonly observed in lanthanide-doped bulk

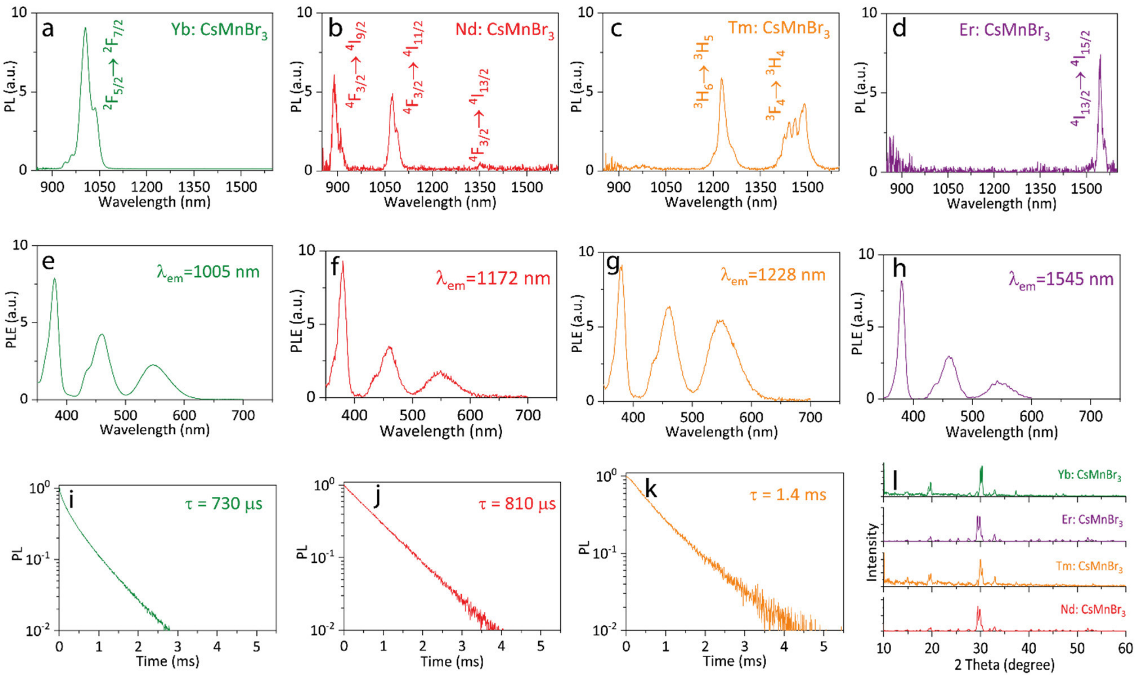

Figure 3.3: Vis-to-NIR downshifting using Ln3+-dopedCsMnBr$_3$ NCs. (a) Yb-doped, (b) Nd-doped, (c) Tm-doped, and (d) Er-dopedCsMnBr$_3$ NCs (exc = 550 nm). PLE spectra of (e) Yb-doped (em = 1005 nm), (f) Nd-doped (em = 1172 nm), (g) Tm-doped (em = 1228 nm), and (h) Er-doped (em = 1545 nm)CsMnBr$_3$ NCs. PL decay curves of (i) Yb-doped (det = 990 nm), (j) Nd-doped (det = 895 nm), and (k) Tm-doped (det = 1485 nm)CsMnBr$_3$ NCs (exc= 355 nm). (l) XRD patterns of theCsMnBr$_3$ NCs doped with Yb, Er, Tm, and Nd ions

CsMnBr$_3$, [131, 140, 141] CsMnCl$_3$, [131, 142] and CsMnI3. [131, 140] In our case, since the NCs are small and the doping level is relatively higher (around 1 part per 80, 84, 100, and 112 for Nd,- Yb-, Er-, and Tm-doped CsMnBr$_3$, respectively) than the one reported for doped CsMnBr$_3$ (1 part per 1000 for Nd:CsMnBr$_3$ 80 and 1 part per 500 for Er:CsMnBr$_3$ 77), energy transfer does not require migration of excitation among all Mn sites. For this reason, the introduction of lanthanides quenches completely the emission from the Mn-centered d-d transition of CsMnBr$_3$ at 661 nm. The near-infrared PL time decays show a singleexponential decay with a lifetime of 810, 730, and 1400 μs for Nd:CsMnBr$_3$, Yb:CsMnBr$_3$, and Tm:CsMnBr$_3$, respectively (Figure 3.3i-k), which also shows that there is no interdoping effect. Computational Analysis of Ln^{3+}-Doped CsMnBr$_3$ and Cs$_3$MnBr$_5$ NCs. To disentangle the mechanism of emission of lanthanide-doped CsMnBr$_3$ and Cs$_3$MnBr$_5$ NCs, we carried out DFT calculations. First, the band structures of both undoped CsMnBr$_3$ and Cs$_3$MnBr$_5$ systems were computed at the DFT/PBE level (Figure 3.4a,d).

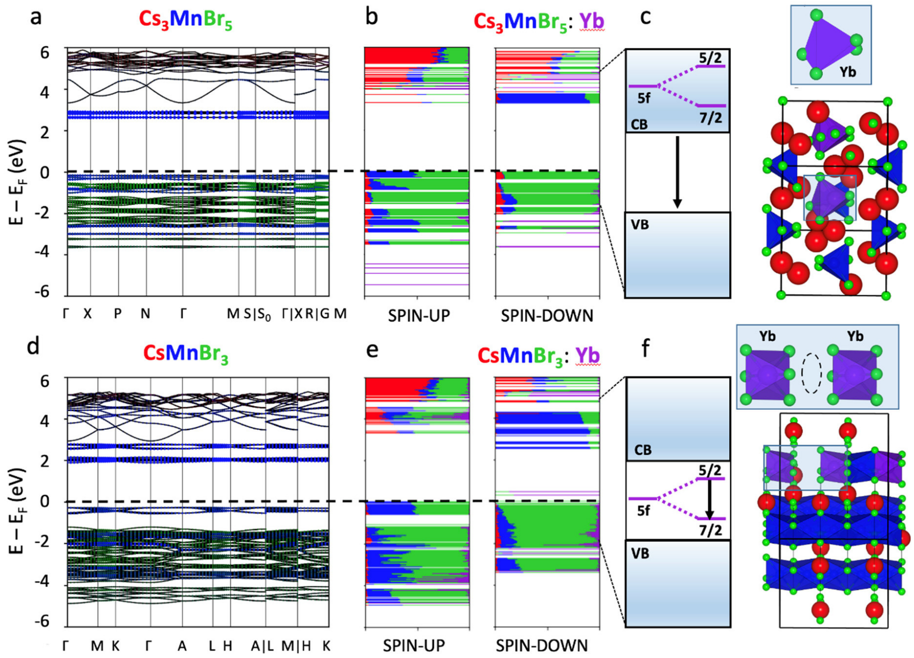

Figure 3.4: Density functional theory analyses of undoped and doped Cs_3MnBr_5 and$CsMnBr_3$ systems. (a) Element projected band structure of the relaxed Cs_3MnBr_5 unit cell calculated at the DFT/PBE level of theory. (b) Electronic structure of the Yb-doped Cs_3MnBr_5 2×2×2 supercell (shown on the right) computed at the Γ point at the DFT/PBE level of theory. Each orbital is represented in real space and decomposed according to each atom type. (c) Scheme of the expected position for Yb 5f(5/2) and 5f(7/2) orbitals upon spin–orbit mixing. (d), (e), and (f) are the same as (a), (b), and (c), respectively, but for the$CsMnBr_3$ system.

In these band structures, the flat conduction and valence band edges are dominated by localized Mn half-filled d orbitals, which confirms that the emission arises from the d-d transition of Mn^{2+} ion in d5 configuration (see Figure 3.2d,e). Our calculations also indicate that both systems slightly favor an antiferromagnetic behavior . For the doped systems, we decided to analyze the Yb doping since Yb presents only one unpaired electron that gives origin to one emission line (2 F5/2→2 F7/2) upon spin-orbit mixing and greatly facilitates the interpretation of the results. To improve the convergence of our DFT calculations, we considered spin-free calculations, i.e., no spin-orbit coupling: we doubled the size of the unit cell to perform the computation only in the Γ point and assumed a purely ferromagnetic behavior, with all unpaired electrons in Mn and Yb occupying the spin-up orbitals. We consider this latter approximation as valid due to the very small energetic difference from the purely antiferromagnetic systems. We do, however, warn the reader that based on the above approximations and considering that DFT has limitations in describing f-orbitals with high precision, we aim to acquire only a purely qualitative description of the doped systems. Starting with the density of states of the Cs_3MnBr_5:Yb system (Figure 3.4b), composed of disconnected tetrahedra, we can notice that even in the case when Yb is incorporated in Cs_3MnBr_5, the occupied f-orbitals of Yb lie very deep in the valence band, whereas the only unoccupied f orbital (spindown) is found at energies higher than the Mn d-orbitals. In Figure 3.4c, we show schematically that even if spin-orbit coupling would be considered, the Yb orbitals would probably lie above the conduction band, thus possibly preventing any energy transfer from the Mn d-orbitals, which we know absorb light from the PLE spectra of the doped systems. On the other hand, the $CsMnBr_3$ system presents a different electronic structure. The 1D connectivity among Mn and Yb octahedra moves the unoccupied f-orbital (spin-down) deep inside the band gap of the material, as shown in Figure 3.4e. Although the exact energetic position inside the gap is probably not well reproduced by DFT, we can safely assume that even after spin-orbit mixing, both 5f5/2 and 5f7/2 orbitals would still lie in the band gap, allowing emission from the dopant (Figure 3.4f). Additionally, we can also observe that the f-orbital is mixed with the 4p orbitals of Br, which are directly connected to the nearby Mn ions. This means that the conversion efficiency from Mn to Yb could be facilitated by electron-phonon coupling. A similar mechanism can be expected also from the other dopants.

3.4. Conclusions and future works

We have introduced an optimized synthesis of $CsMnBr_3$ and Cs_3MnBr_5 NCs and studied the funtamentals of their photphysics as undoped systems. Importantly, only $CsMnBr_3$ NCs could host different types of lanthanide ions and sensitize them via visible excitation, which was shown in our DFT calculations as well. As a result, sharp emissions at 890 and 1075 nm from Nd^{3+}, 1005 nm from Yb^{3+}, 1226 and 1489 nm from Tm^{3+}, and 1544 nm from Er^{3+} were detected upon visible excitation of the $CsMnBr_3$ NCs matrix. This work provides a lead-free material as an efficient sensitizer, which can lead to development and design of visible-to-NIR downshifters. Further studies are needed to fully understand the energy transfer mechanism and exciton migration within the perovskite absorbing matrix to the emissions centers in order to raise the NIR PLQY.

4 | Conclusions and future developments

During my PhD, I have been able to build an efficient, versatile and fully customizable Single Particle Set-up. Data on colloidal CdSe/ZnS Nanoplatles show that it is possible to fully characterize the peculiar photophysics of single quantum emitters by having state of art analysis tools and results. Some improvements can be done to further improve the usability of such complex set-up and make the measurement even more effective and less time consuming, such as a easy switchable source from wide area to confocal imaging and finer control of the x-y stage movement. Now the goal is to use such system for a great number of state-of-art luminescent nanoparticles for which such measurement can answer open scientific questions related to chemical nano-design; parallely, it would be interesting to study if it is possible to characterize well-known single photon sources for quantum applications.

Among those, strongly confined LHP showed in chapter two are great candidates for such studies and can be a great starting point. Regarding LHP Heterostructures, a great step has been made in the chemical challenge of building a complex and innovative nanocrystal, but exerimental effort still has to be done in order to raise the efficiency of those objects as emitters and improvements on surface chemistry will be crucial in the near future to make them competitive as optically active materials.

Meanwhile, the possibility of discovering new phases via epitaxial colloidal synthesis might open up to new synthetic routes in which SPS could play a key role in understanding the effect of crystal phase over the emission properties.

Ultimately, in the field of doped Cesium Manganese Bromides, we're currently studying fundamentals on how the excitation moves along 1D Mn chains to reach rare earth atoms emmission centers; the final goal would be realizing the most efficient energy transfer, so that the final NIR emission can reach the highest QY. Then, NIR single photon emission can be studied.

Bibliography

[1] Xun Wang, Jing Zhuang, Qing Peng, and Yadong Li. A general strategy for nanocrystal synthesis. *Nature*, 437(7055):121–124, 2005.

[2] Jiajia Zhou, Alexey I Chizhik, Steven Chu, and Dayong Jin. Single-particle spectroscopy for functional nanomaterials. *Nature*, 579(7797):41–50, 2020.

[3] Timothy P Spiller. Quantum information technology. *Materials Today*, 6(1):30–36, 2003.

[4] Mario Krenn, Mehul Malik, Thomas Scheidl, Rupert Ursin, and Anton Zeilinger. *Quantum Communication with Photons*, pages 455–482. Springer International Publishing, Cham, 2016.

[5] Nicolas Gisin, Grégoire Ribordy, Wolfgang Tittel, and Hugo Zbinden. Quantum cryptography. *Rev. Mod. Phys.*, 74:145–195, Mar 2002.

[6] Ł. Dusanowski, M. Syperek, A. Maryński, L. H. Li, J. Misiewicz, S. Höfling, M. Kamp, A. Fiore, and G. Sęk. Single photon emission up to liquid nitrogen temperature from charged excitons confined in gaas-based epitaxial nanostructures. *Applied Physics Letters*, 106(23):233107, 2015.

[7] X. M. Dou, X. Y. Chang, B. Q. Sun, Y. H. Xiong, Z. C. Niu, S. S. Huang, H. Q. Ni, Y. Du, and J. B. Xia. Single-photon-emitting diode at liquid nitrogen temperature. *Applied Physics Letters*, 93(10):101107, 2008.

[8] Jeffrey M. Pietryga, Young-Shin Park, Jaehoon Lim, Andrew F. Fidler, Wan Ki Bae, Sergio Brovelli, and Victor I. Klimov. Spectroscopic and device aspects of nanocrystal quantum dots. *Chemical Reviews*, 116(18):10513–10622, 2016. PMID: 27677521.

[9] Gabriele Rainò, Annelies Landuyt, Franziska Krieg, Caterina Bernasconi, Stefan T. Ochsenbein, Dmitry N. Dirin, Maryna I. Bodnarchuk, and Maksym V. Kovalenko. Underestimated effect of a polymer matrix on the light emission of single cspbbr3 nanocrystals. *Nano Letters*, 19(6):3648–3653, 2019. PMID: 31117751.

[10] Chenglian Zhu, Malwina Marczak, Leon Feld, Simon C. Boehme, Caterina Bernasconi, Anastasiia Moskalenko, Ihor Cherniukh, Dmitry Dirin, Maryna I. Bodnarchuk, Maksym V. Kovalenko, and Gabriele Rainò. Room-temperature, highly pure single-photon sources from all-inorganic lead halide perovskite quantum dots. *Nano Letters*, 22(9):3751–3760, 2022. PMID: 35467890.

[11] Christophe Galland, Yagnaseni Ghosh, Andrea Steinbrück, Milan Sykora, Jennifer A Hollingsworth, Victor I Klimov, and Han Htoon. Two types of luminescence blinking revealed by spectroelectrochemistry of single quantum dots. *Nature*, 479(7372):203–207, 2011.

[12] Christophe Galland, Yagnaseni Ghosh, Andrea Steinbrück, Jennifer A Hollingsworth, Han Htoon, and Victor I Klimov. Lifetime blinking in nonblinking nanocrystal quantum dots. *Nature communications*, 3(1):908, 2012.

[13] Robert H Hadfield. Single-photon detectors for optical quantum information applications. *Nature photonics*, 3(12):696–705, 2009.

[14] Abhinav Anand, Matteo L. Zaffalon, Graziella Gariano, Andrea Camellini, Marina Gandini, Rosaria Brescia, Chiara Capitani, Francesco Bruni, Valerio Pinchetti, Margherita Zavelani-Rossi, Francesco Meinardi, Scott A. Crooker, and Sergio Brovelli. Evidence for the band-edge exciton of cuins2 nanocrystals enables record efficient large-area luminescent solar concentrators. *Advanced Functional Materials*, 30(4):1906629, 2020.

[15] Huidong Zang, Hongbo Li, Nikolay S. Makarov, Kirill A. Velizhanin, Kaifeng Wu, Young-Shin Park, and Victor I. Klimov. Thick-shell cuins2/zns quantum dots with suppressed "blinking" and narrow single-particle emission line widths. *Nano Letters*, 17(3):1787–1795, 2017. PMID: 28169547.

[16] Patrick J. Whitham, Arianna Marchioro, Kathryn E. Knowles, Troy B. Kilburn, Philip J. Reid, and Daniel R. Gamelin. Single-particle photoluminescence spectra, blinking, and delayed luminescence of colloidal cuins2 nanocrystals. *The Journal of Physical Chemistry C*, 120(30):17136–17142, 2016.

[17] Chiara Capitani, Valerio Pinchetti, Graziella Gariano, Beatriz Santiago-González, Carlo Santambrogio, Marcello Campione, Mirko Prato, Rosaria Brescia, Andrea Camellini, Fulvio Bellato, Francesco Carulli, Abhinav Anand, Margherita Zavelani-Rossi, Francesco Meinardi, Scott A. Crooker, and Sergio Brovelli. Quantized electronic doping towards atomically controlled "charge-engineered" semiconductor nanocrystals. *Nano Letters*, 19(2):1307–1317, 2019. PMID: 30663314.

[18] Arman Najafi, Manoj Sharma, Savas Delikanli, Arinjoy Bhattacharya, Joseph R. Murphy, James Pientka, Ashma Sharma, Alexander P. Quinn, Onur Erdem, Subash Kattel, Yusuf Kelestemur, Maksym V. Kovalenko, William D. Rice, Hilmi Volkan Demir, and Athos Petrou. Light-induced paramagnetism in colloidal ag+-doped cdse nanoplatelets. *The Journal of Physical Chemistry Letters*, 12(11):2892–2899, 2021. PMID: 33724845.

[19] Benoit Mahler, Brice Nadal, Cecile Bouet, Gilles Patriarche, and Benoit Dubertret. Core/shell colloidal semiconductor nanoplatelets. *Journal of the American Chemical Society*, 134(45):18591–18598, 2012. PMID: 23057684.

[20] Sandrine Ithurria, MD Tessier, Benoit Mahler, RPSM Lobo, B Dubertret, and Al L Efros. Colloidal nanoplatelets with two-dimensional electronic structure. *Nature materials*, 10(12):936–941, 2011.

[21] Zitong Zhang and Handong Sun. Manipulation of the optical properties of colloidal 2d cdse nanoplatelets. *Advanced Photonics Research*, 2(8):2100045, 2021.

[22] MD Tessier, B Mahler, B Nadal, H Heuclin, S Pedetti, and B Dubertret. Spectroscopy of colloidal semiconductor core/shell nanoplatelets with high quantum yield. *Nano letters*, 13(7):3321–3328, 2013.

[23] Zhuoying Chen, Brice Nadal, Benoit Mahler, Hervé Aubin, and Benoit Dubertret. Quasi-2d colloidal semiconductor nanoplatelets for narrow electroluminescence. *Advanced Functional Materials*, 24(3):295–302, 2014.

[24] Dahui Zhao and Timothy M. Swager. Sensory responses in solution vs solid state: a fluorescence quenching study of poly(iptycenebutadiynylene)s. *Macromolecules*, 38(22):9377–9384, 2005.

[25] N. Akil, S.E. Kerns, D.V. Kerns, A. Hoffmann, and J.-P. Charles. A multimechanism model for photon generation by silicon junctions in avalanche breakdown. *IEEE Transactions on Electron Devices*, 46(5):1022–1028, 1999.

[26] A. G. Chynoweth and K. G. McKay. Photon emission from avalanche breakdown in silicon. *Phys. Rev.*, 102:369–376, Apr 1956.

[27] Aydan Yeltik, Savas Delikanli, Murat Olutas, Yusuf Kelestemur, Burak Guzelturk, and Hilmi Volkan Demir. Experimental determination of the absorption cross-section and molar extinction coefficient of colloidal cdse nanoplatelets. *The Journal of Physical Chemistry C*, 119(47):26768–26775, 2015.

[28] Zhongjian Hu, Ajay Singh, Serguei V. Goupalov, Jennifer A. Hollingsworth, and

Han Htoon. Influence of morphology on the blinking mechanisms and the excitonic fine structure of single colloidal nanoplatelets. *Nanoscale*, 10:22861–22870, 2018.

[29] Xuedan Ma, Benjamin T. Diroll, Wooje Cho, Igor Fedin, Richard D. Schaller, Dmitri V. Talapin, Stephen K. Gray, Gary P. Wiederrecht, and David J. Gosztola. Size-dependent biexciton quantum yields and carrier dynamics of quasi-two-dimensional core/shell nanoplatelets. *ACS Nano*, 11(9):9119–9127, 2017. PMID: 28787569.

[30] Mickaël D. Tessier, Clémentine Javaux, Ivan Maksimovic, Vincent Loriette, and Benoit Dubertret. Spectroscopy of single cdse nanoplatelets. *ACS Nano*, 6(8):6751–6758, 2012. PMID: 22783952.

[31] D. P. Nenon, K. Pressler, J. Kang, B. A. Koscher, J. H. Olshansky, W. T. Osowiecki, M. A. Koc, L.-W. Wang, and A. P. Alivisatos. Design principles for trap-free cspbx3 nanocrystals: Enumerating and eliminating surface halide vacancies with softer lewis bases. *J. Am. Chem. Soc.*, 140:17760, 2018.

[32] S. Ten Brinck, F. Zaccaria, and I. Infante. Defects in lead halide perovskite nanocrystals: Analogies and (many) differences with the bulk. *ACS Energy Lett.*, 4:2739, 2019.

[33] B. Zhang, L. Goldoni, J. Zito, Z. Dang, G. Almeida, F. Zaccaria, J. de Wit, I. Infante, L. De Trizio, and L. Manna. Alkyl phosphonic acids deliver cspbbr3 nanocrystals with high photoluminescence quantum yield and truncated octahedron shape. *Chem. Mater.*, 31:9140, 2019.

[34] S. Ten Brinck and I. Infante. Surface termination, morphology, and bright photoluminescence of cesium lead halide perovskite nanocrystals. *ACS Energy Lett.*, 1:1266, 2016.

[35] R. Grisorio, M. E. Di Clemente, E. Fanizza, I. Allegretta, D. Altamura, M. Striccoli, R. Terzano, C. Giannini, M. Irimia-Vladu, and G. P. Suranna. Exploring the surface chemistry of cesium lead halide perovskite nanocrystals. *Nanoscale*, 11:986, 2019.

[36] J. Shamsi, A. S. Urban, M. Imran, L. De Trizio, and L. Manna. Metal halide perovskite nanocrystals: Synthesis, post-synthesis modifications, and their optical properties. *Chem. Rev.*, 119:3296, 2019.

[37] M. Imran, P. Ijaz, L. Goldoni, D. Maggioni, U. Petralanda, M. Prato, G. Almeida, I. Infante, and L. Manna. Simultaneous cationic and anionic ligand exchange for colloidally stable cspbbr3 nanocrystals. *ACS Energy Lett.*, 4:819, 2019.

[38] F. Krieg, S. T. Ochsenbein, S. Yakunin, S. Ten Brinck, P. Aellen, A. Sºess, B. Clerc, D. Guggisberg, O. Nazarenko, Y. Shynkarenko, S. Kumar, C.-J. Shih, I. Infante, and M. V. Kovalenko. Colloidal cspbx3 (x = cl, br, i) nanocrystals 2.0: Zwitterionic capping ligands for improved durability and stability. *ACS Energy Lett.*, 3:641, 2018.

[39] L. Protesescu, S. Yakunin, M. I. Bodnarchuk, F. Krieg, R. Caputo, C. H. Hendon, R. X. Yang, A. Walsh, and M. V. Kovalenko. Nanocrystals of cesium lead halide perovskites (cspbx3, x = cl, br, and i): Novel optoelectronic materials showing bright emission with wide color gamut. *Nano Lett.*, 15:3692, 2015.

[40] J. Butkus, P. Vashishtha, K. Chen, J. K. Gallaher, S. K. K. Prasad, D. Z. Metin, G. Laufersky, N. Gaston, J. E. Halpert, and J. M. Hodgkiss. The evolution of quantum confinement in cspbbr3 perovskite nanocrystals. *Chem. Mater.*, 29:3644, 2017.

[41] D. Rossi, X. Liu, Y. Lee, M. Khurana, J. Puthenpurayil, K. Kim, A. V. Akimov, J. Cheon, and D. H. Son. Intense dark exciton emission from strongly quantum-confined cspbbr3 nanocrystals. *Nano Lett.*, 20:7321, 2020.

[42] M. A. Becker, R. Vaxenburg, G. Nedelcu, P. C. Sercel, A. Shabaev, M. J. Mehl, J. G. Michopoulos, S. G. Lambrakos, N. Bernstein, J. L. Lyons, T. Stferle, R. F. Mahrt, M. V. Kovalenko, D. J. Norris, G. Rain, and A. L. Efros. Bright triplet excitons in caesium lead halide perovskites. *Nature*, 553:189, 2018.

[43] J. De Roo, Z. Zhou, J. Wang, L. Deblock, A. J. Crosby, J. S. Owen, and S. S. Nonnenmann. Synthesis of phosphonic acid ligands for nanocrystal surface functionalization and solution processed memristors. *Chem. Mater.*, 30:8034, 2018.

[44] S. R. Smock, T. J. Williams, and R. L. Brutchey. Quantifying the thermodynamics of ligand binding to cspbbr3 quantum dots. *Angew. Chem.*, 130:11885, 2018.

[45] J. S. Owen, J. Park, P.-E. Trudeau, and A. P. Alivisatos. Reaction chemistry and ligand exchange at cadmium-selenide nanocrystal surfaces. *J. Am. Chem. Soc.*, 130:12279, 2008.

[46] J. Y. Woo, S. Lee, S. Lee, W. D. Kim, K. Lee, K. Kim, H. J. An, D. C. Lee, and S. Jeong. Air-stable pbse nanocrystals passivated by phosphonic acids. *J. Am. Chem. Soc.*, 138:876, 2016.

[47] H. Shi, X. Zhang, X. Sun, R. Chen, and X. Zhang. Direct and indirect recombination

and thermal kinetics of excitons in colloidal all-inorganic lead halide perovskite nanocrystals. *J. Phys. Chem. C*, 123:19844, 2019.

[48] W. Wu, W. Liu, Q. Wang, Q. Han, and Q. Yang. Temperature-dependent photoluminescence of pure and mn-doped cspbcl3 nanocrystals. *J. Alloys Compd.*, 787:165, 2019.

[49] S. Bera and N. Pradhan. Perovskite nanocrystal heterostructures: Synthesis, optical properties, and applications. *ACS Energy Lett.*, 5:2858, 2020.

[50] P. V. Kamat, N. Pradhan, K. Schanze, P. S. Weiss, J. Buriak, P. Stang, T. W. Odom, and G. Hartland. Challenges and opportunities in designing perovskite nanocrystal heterostructures. *ACS Energy Lett.*, 5:2253, 2020.

[51] S. K. Balakrishnan and P. V. Kamat. Au-cspbbr3 hybrid architecture: Anchoring gold nanoparticles on cubic perovskite nanocrystals. *ACS Energy Lett.*, 2:88, 2017.

[52] X. Zhang, X. Wu, X. Liu, G. Chen, Y. Wang, J. Bao, X. Xu, X. Liu, Q. Zhang, K. Yu, W. Wei, J. Liu, J. Xu, H. Jiang, P. Wang, and X. Wang. Heterostructural cspbx3-pbs (x = cl, br, i) quantum dots with tunable vis-nir dual emission. *J. Am. Chem. Soc.*, 142:4464, 2020.

[53] W. Chen, J. Hao, W. Hu, Z. Zang, X. Tang, L. Fang, T. Niu, and M. Zhou. Enhanced stability and tunable photoluminescence in perovskite cspbx3/zns quantum dot heterostructure. *Small*, 13:1604085, 2017.

[54] V. K. Ravi, S. Saikia, S. Yadav, V. V. Nawale, and A. Nag. Cspbbr3/zns core/shell type nanocrystals for enhancing luminescence lifetime and water stability. *ACS Energy Lett.*, 5:1794, 2020.

[55] T. P. Nguyen, A. Ozturk, J. Park, W. Sohn, T. H. Lee, H. W. Jang, and S. Y. Kim. Facile synthesis of cspbbr3/pbse composite clusters. *Sci. Technol. Adv. Mater.*, 19:10, 2018.

[56] X.-D. Wang, Y.-H. Huang, J.-F. Liao, Y. Jiang, L. Zhou, X.-Y. Zhang, H.-Y. Chen, and D.-B. Kuang. In situ construction of a cs2sni6 perovskite nanocrystal/sns2 nanosheet heterojunction with boosted interfacial charge transfer. *J. Am. Chem. Soc.*, 141:13434, 2019.

[57] F. Xu, K. Meng, B. Cheng, S. Wang, J. Xu, and J. Yu. Unique s-scheme heterojunctions in self-assembled tio2/cspbbr3 hybrids for co2 photoreduction. *Nat. Commun.*, 11:1, 2020.

[58] H. Hu, L. Wu, Y. Tan, Q. Zhong, M. Chen, Y. Qiu, D. Yang, B. Sun, Q. Zhang, and Y. Yin. Interfacial synthesis of highly stable cspbx3/oxide janus nanoparticles. *J. Am. Chem. Soc.*, 140:406, 2018.

[59] H. Liu, Y. Tan, M. Cao, H. Hu, L. Wu, X. Yu, L. Wang, B. Sun, and Q. Zhang. Fabricating cspbx3-based type i and type ii heterostructures by tuning the halide composition of janus cspbx3/zro2 nanocrystals. *ACS Nano*, 13:5366, 2019.

[60] Z.-J. Li, E. Hofman, J. Li, A. H. Davis, C.-H. Tung, L.-Z. Wu, and W. Zheng. Photoelectrochemically active and environmentally stable cspbbr3/tio2 core/shell nanocrystals. *Adv. Funct. Mater.*, 28:1704288, 2018.

[61] J. Shamsi, Z. Dang, P. Ijaz, A. L. Abdelhady, G. Bertoni, I. Moreels, and L. Manna. Colloidal csx (x = cl, br, i) nanocrystals and their transformation to cspbx3 nanocrystals by cation exchange. *Chem. Mater.*, 30:79, 2018.

[62] D. Baranov, G. Caputo, L. Goldoni, Z. Dang, R. Scarfiello, L. De Trizio, A. Portone, F. Fabbri, A. Camposeo, D. Pisignano, and L. Manna. Transforming colloidal cs4pbbr6 nanocrystals with poly(maleic anhydride-alt-1-octadecene) into stable cspbbr3 perovskite emitters through intermediate heterostructures. *Chem. Sci.*, 11:3986, 2020.

[63] S. Toso, D. Baranov, and L. Manna. Hidden in plain sight: the overlooked influence of the cs+ substructure on transformations in cesium lead halide nano-crystals. *ACS Energy Lett.*, 5:3409, 2020.

[64] X. Zhang, M. Lu, Y. Zhang, H. Wu, X. Shen, W. Zhang, W. Zheng, V. L. Colvin, and W. W. Yu. Pbs capped cspbi3 nanocrystals for efficient and stable light-emitting devices using p-i-n structures. *ACS Cent. Sci.*, 4:1352, 2018.

[65] S. Wang, C. Bi, A. Portniagin, J. Yuan, J. Ning, X. Xiao, X. Zhang, Y. Y. Li, S. V. Kershaw, J. Tian, and A. L. Rogach. Cspbi3/pbse heterostructured nanocrystals for high-efficiency solar cells. *ACS Energy Lett.*, 5:2401, 2020.

[66] S. Toso, Q. A. Akkerman, B. Martn-Garca, M. Prato, J. Zito, I. Infante, Z. Dang, A. Moliterni, C. Giannini, E. Bladt, I. Lobato, J. Ramade, S. Bals, J. Buha, D. Spirito, E. Mugnaioli, M. Gemmi, and L. Manna. Nanocrystals of lead chalcohalides: A series of kinetically trapped metastable nanostructures. *J. Am. Chem. Soc.*, 142:10198, 2020.

[67] L. Peng, A. Dutta, R. Xie, W. Yang, and N. Pradhan. Dot-wire-platelet-cube: Step

growth and structural transformations in cspbbr3 perovskite nanocrystals. *ACS Energy Lett.*, 3:2014, 2018.

[68] L. Peng, S. K. Dutta, D. Mondal, B. Hudait, S. Shyamal, R. Xie, P. Mahadevan, and N. Pradhan. Arm growth and facet modulation in perovskite nanocrystals. *J. Am. Chem. Soc.*, 141:16160, 2019.

[69] L. Protesescu, S. Yakunin, M. I. Bodnarchuk, F. Krieg, R. Caputo, C. H. Hendon, R. X. Yang, A. Walsh, and M. V. Kovalenko. Nanocrystals of cesium lead halide perovskites (cspbx3, x = cl, br, and i): Novel optoelectronic materials showing bright emission with wide color gamut. *Nano Lett.*, 15:3692, 2015.

[70] M. Imran, V. Caligiuri, M. Wang, L. Goldoni, M. Prato, R. Krahne, L. De Trizio, and L. Manna. Benzoyl halides as alternative precursors for the colloidal synthesis of lead-based halide perovskite nanocrystals. *J. Am. Chem. Soc.*, 140:2656, 2018.

[71] A. Dutta, S. K. Dutta, S. Das Adhikari, and N. Pradhan. Tuning the size of cspbbr3 nanocrystals: all at one constant temperature. *ACS Energy Lett.*, 3:329, 2018.

[72] A. De Backer, K. Van den Bos, W. Van den Broek, J. Sijbers, and S. Van Aert. Statstem: an efficient approach for accurate and precise model-based quantification of atomic resolution electron microscopy images. *Ultramicroscopy*, 171:104, 2016.

[73] V. Grillo. The effect of surface strain relaxation on haadf imaging. *Ultramicroscopy*, 109:1453, 2009.

[74] K. Wu, G. Liang, D. Kong, J. Chen, Z. Chen, X. Shan, J. R. McBride, and T. Lian. Quasi-type ii cuins2/cds core/shell quantum dots. *Chem. Sci.*, 7:1238, 2016.

[75] R. J. Sutton, M. R. Filip, A. A. Haghighirad, N. Sakai, B. Wenger, F. Giustino, and H. J. Snaith. Cubic or orthorhombic? revealing the crystal structure of metastable black-phase cspbi3 by theory and experiment. *ACS Energy Lett.*, 3:1787, 2018.

[76] Danrui Ni, Shu Guo, Kelly M. Powderly, Ruidan Zhong, and Robert J. Cava. A high-pressure phase with a non-centrosymmetric crystal structure in the pbse–pbbr2 system. *Journal of Solid State Chemistry*, 280:120982, 2019.

[77] Stefano Toso, Quinten A Akkerman, Beatriz Martín-García, Mirko Prato, Juliette Zito, Ivan Infante, Zhiya Dang, Anna Moliterni, Cinzia Giannini, Eva Bladt, et al. Nanocrystals of lead chalcohalides: A series of kinetically trapped metastable nanostructures. *Journal of the American Chemical Society*, 142(22):10198–10211, 2020.

[78] Danrui Ni, Shu Guo, Zoë S Yang, Kelly M Powderly, and Robert J Cava. Pb4s3i2–a high-pressure phase in the pbs-pbi2 system. *Solid State Sciences*, 91:49–53, 2019.

[79] Muhammad Imran, Lucheng Peng, Andrea Pianetti, Valerio Pinchetti, Julien Ramade, Juliette Zito, Francesco Di Stasio, Joka Buha, Stefano Toso, Jun Song, et al. Halide perovskite–lead chalcohalide nanocrystal heterostructures. *Journal of the American Chemical Society*, 143(3):1435–1446, 2021.

[80] Stefano Toso, Dmitry Baranov, and Liberato Manna. Hidden in plain sight: The overlooked influence of the cs+ substructure on transformations in cesium lead halide nanocrystals. *ACS Energy Letters*, 5(11):3409–3414, 2020.

[81] Nilabh Dish, Rakesh Behera, A Satyaprasad, and Abhay Gautam. Epitaxial growth of copper, gold, and silver on vicinal nacl surfaces. *Applied Surface Science*, 574:151643, 2022.

[82] Dong Kyu Lee, Sungjoo Kim, Sein Oh, Jae-Young Choi, Jong-Lam Lee, and Hak Ki Yu. Water-soluble epitaxial nacl thin film for fabrication of flexible devices. *Scientific Reports*, 7(1):1–7, 2017.

[83] Q. A. Akkerman, V. D,ÄôInnocenzo, S. Accornero, A. Scarpellini, A. Petrozza, M. Prato, and L. Manna. Tuning the optical properties of cesium lead halide perovskite nanocrystals by anion exchange reactions. *J. Am. Chem. Soc.*, 137:10276, 2015.

[84] J. P. Perdew, K. Burke, and M. Ernzerhof. Generalized gradient approximation made simple. *Phys. Rev. Lett.*, 77:3865, 1996.

[85] J. Hutter, M. Iannuzzi, F. Schiffmann, and J. VandeVondele. cp2k: atomistic simulations of condensed matter systems. *Wiley Interdiscip. Rev. Comput. Mol. Sci.*, 4:15, 2014.

[86] N. Murphy, R. Wortis, and W. Atkinson. Generalized inverse participation ratio as a possible measure of localization for interacting systems. *Phys. Rev. B: Condens. Matter Mater. Phys.*, 83:184206, 2011.

[87] A. J. Houtepen, Z. Hens, J. S. Owen, and I. Infante. On the origin of surface traps in colloidal ii-vi semiconductor nanocrystals. *Chem. Mater.*, 29:752, 2017.

[88] R. Gomes, A. Hassinen, A. Szczygiel, Q. Zhao, A. Vantomme, J. C. Martins, and Z. Hens. Binding of phosphonic acids to cdse quantum dots: A solution nmr study. *J. Phys. Chem. Lett.*, 2:145, 2011.

[89] X. Huang, S. Han, W. Huang, and X. Liu. Enhancing solar cell efficiency: the search for luminescent materials as spectral converters. *Chem. Soc. Rev.*, 42:173, 2013.

[90] D. Zhou, R. Sun, W. Xu, N. Ding, D. Li, X. Chen, G. Pan, X. Bai, and H. Song. Impact of host composition, codoping, or tridoping on quantum-cutting emission of ytterbium in halide perovskite quantum dots and solar cell applications. *Nano Lett.*, 19:6904, 2019.

[91] D. Zhou, D. Liu, G. Pan, X. Chen, D. Li, W. Xu, X. Bai, and H. Song. Cerium and ytterbium codoped halide perovskite quantum dots: a novel and efficient downconverter for improving the performance of silicon solar cells. *Adv. Mater.*, 29:1704149, 2017.

[92] Y. Dong, Y.-K. Wang, F. Yuan, A. Johnston, Y. Liu, D. Ma, M.-J. Choi, B. Chen, M. Chekini, S.-W. Baek, L. K. Sagar, J. Fan, Y. Hou, M. Wu, S. Lee, B. Sun, S. Hoogland, R. Quintero-Bermudez, H. Ebe, P. Todorovic, F. Dinic, P. Li, H. T. Kung, M. I. Saidaminov, E. Kumacheva, E. Spiecker, L.-S. Liao, O. Voznyy, Z.-H. Lu, and E. H. Sargent. Bipolar-shell resurfacing for blue leds based on strongly confined perovskite quantum dots. *Nat. Nanotechnol.*, 15:668, 2020.

[93] H. Huang, R. Li, S. Jin, Z. Li, P. Huang, J. Hong, S. Du, W. Zheng, X. Chen, and D. Chen. Ytterbium-doped cspbcl3 quantum cutters for near-infrared light-emitting diodes. *ACS Appl. Mater. Interfaces*, 13:34561, 2021.

[94] Y. Zhong, Z. Ma, S. Zhu, J. Yue, M. Zhang, A. L. Antaris, J. Yuan, R. Cui, H. Wan, and Y. Zhou. Boosting the down-shifting luminescence of rare-earth nanocrystals for biological imaging beyond 1500 nm. *Nat. Commun.*, 8:737, 2017.

[95] H. Zhang, Y. Fan, P. Pei, C. Sun, L. Lu, and F. Zhang. Tm3+-sensitized nir-ii fluorescent nanocrystals for in vivo information storage and decoding. *Angew. Chem., Int. Ed.*, 58:10153, 2019.

[96] Y. Zhong, Z. Ma, F. Wang, X. Wang, Y. Yang, Y. Liu, X. Zhao, J. Li, H. Du, and M. Zhang. In vivo molecular imaging for immunotherapy using ultra-bright near-infrared-iib rare-earth nanoparticles. *Nat. Biotechnol.*, 37:1322, 2019.

[97] L. Liu, S. Wang, B. Zhao, P. Pei, Y. Fan, X. Li, and F. Zhang. Er3+ sensitized 1530 to 1180 nm second near-infrared window upconversion nanocrystals for in vivo biosensing. *Angew. Chem.*, 130:7640, 2018.

[98] X. Lei, R. Li, D. Tu, X. Shang, Y. Liu, W. You, C. Sun, F. Zhang, and X. Chen.

Intense near-infrared-ii luminescence from nacef4: Er/yb nanoprobes for in vitro bioassay and in vivo bioimaging. *Chem. Sci.*, 9:4682, 2018.

[99] H. Zhang, Z.-H. Chen, X. Liu, and F. Zhang. A mini-review on recent progress of new sensitizers for luminescence of lanthanide doped nanomaterials. *Nano Res.*, 13:1795, 2020.

[100] Y. Fan, P. Wang, Y. Lu, R. Wang, L. Zhou, X. Zheng, X. Li, J. A. Piper, and F. Zhang. Lifetime-engineered nir-ii nanoparticles unlock multiplexed in vivo imaging. *Nat. Nanotechnol.*, 13:941, 2018.

[101] J.-Y. Hu, Y. Ning, Y.-S. Meng, J. Zhang, Z.-Y. Wu, S. Gao, and J.-L. Zhang. Highly near-ir emissive ytterbium (iii) complexes with unprecedented quantum yields. *Chem. Sci.*, 8:2702, 2017.

[102] E. G. Moore, A. P. Samuel, and K. N. Raymond. From antenna to assay: lessons learned in lanthanide luminescence. *Acc. Chem. Res.*, 42:542, 2009.

[103] D. A. Chengelis, A. M. Yingling, P. D. Badger, C. M. Shade, and S. Petoud. Incorporating lanthanide cations with cadmium selenide nanocrystals: a strategy to sensitize and protect tb (iii). *J. Am. Chem. Soc.*, 127:16752, 2005.

[104] R. Martn-Rodrguez, R. Geitenbeek, and A. Meijerink. Incorporation and luminescence of yb3+ in cdse nanocrystals. *J. Am. Chem. Soc.*, 135:13668, 2013.

[105] J. K. Swabeck, S. Fischer, N. D. Bronstein, and A. P. Alivisatos. Broadband sensitization of lanthanide emission with indium phosphide quantum dots for visible to near-infrared downshifting. *J. Am. Chem. Soc.*, 140:9120, 2018.

[106] H. Bahmani Jalali, S. Sadeghi, I. Baylam, M. Han, C. W. Ow-Yang, A. Sennaroglu, and S. Nizamoglu. Exciton recycling via inp quantum dot funnels for luminescent solar concentrators. *Nano Res.*, 14:1488, 2021.

[107] D. Song, S. Chi, X. Li, C. Wang, Z. Li, and Z. Liu. Upconversion system with quantum dots as sensitizer: improved photoluminescence and pdt efficiency. *ACS Appl. Mater. Interfaces*, 11:41100, 2019.

[108] A. Jain, S. P. Ong, G. Hautier, W. Chen, W. D. Richards, S. Dacek, S. Cholia, D. Gunter, D. Skinner, G. Ceder, and K. A. Persson. Commentary: The materials project: A materials genome approach to accelerating materials innovation. *APL Mater.*, 1:011002, 2013.

[109] M. Zeng, F. Artizzu, J. Liu, S. Singh, F. Locardi, D. Mara, Z. Hens, and

R. Van Deun. Boosting the er3+ 1.5 Œºm luminescence in cspbcl3 perovskite nanocrystals for photonic devices operating at telecommunication wavelengths. *ACS Appl. Nano Mater.*, 3:4699, 2020.

[110] W. J. Mir, M. Jagadeeswararao, S. Das, and A. Nag. Colloidal mn-doped cesium lead halide perovskite nanoplatelets. *ACS Energy Lett.*, 2:537, 2017.

[111] V. Pinchetti, A. Anand, Q. A. Akkerman, D. Sciacca, M. Lorenzon, F. Meinardi, M. Fanciulli, L. Manna, and S. Brovelli. Trap-mediated two-step sensitization of manganese dopants in perovskite nanocrystals. *ACS Energy Lett.*, 4:85, 2019.

[112] H. Lee, J. Park, S. Kim, S.-C. Lee, Y.-H. Kim, and T.-W. Lee. Perovskite emitters as a platform material for down-conversion applications. *Adv. Mater. Technol.*, 5:2000091, 2020.

[113] M. F. Abdelbar, M. El-Kemary, and N. Fukata. Downshifting of highly energetic photons and energy transfer by mn-doped perovskite cspbcl3 nanocrystals in hybrid organic/silicon nanostructured solar cells. *Nano Energy*, 77:105163, 2020.

[114] M. Zeng, F. Locardi, D. Mara, Z. Hens, R. Van Deun, and F. Artizzu. Switching on near-infrared light in lanthanide-doped cspbcl3 perovskite nanocrystals. *Nanoscale*, 13:8118, 2021.

[115] Z. Fu and S. Xi. The effects of heavy metals on human metabolism. *Toxicol. Mech. Methods*, 30:167, 2020.

[116] J. Sobhanan, P. Jones, R. Kohara, S. Sugino, M. Vacha, C. Subrahmanyam, Y. Takano, F. Lacy, and V. Biju. Toxicity of nanomaterials due to photochemical degradation and the release of heavy metal ions. *Nanoscale*, 12:22049, 2020.

[117] J. Shamsi, A. S. Urban, M. Imran, L. De Trizio, and L. Manna. Metal halide perovskite nanocrystals: Synthesis, post-synthesis modifications, and their optical properties. *Chem. Rev.*, 119:3296, 2019.

[118] W. Lee, S. Hong, and S. Kim. Colloidal synthesis of lead-free silver,Äìindium double-perovskite cs2agincl6 nanocrystals and their doping with lanthanide ions. *J. Phys. Chem. C*, 123:2665, 2019.

[119] N. Chen, T. Cai, W. Li, K. Hills-Kimball, H. Yang, M. Que, Y. Nagaoka, Z. Liu, D. Yang, and A. Dong. Yb-and mn-doped lead-free double perovskite cs2agbix6 (x= cl,Äì, br,Äì) nanocrystals. *ACS Appl. Mater. Interfaces*, 11:16855, 2019.

[120] N. Ding, D. Zhou, G. Pan, W. Xu, X. Chen, D. Li, X. Zhang, J. Zhu, Y. Ji,

and H. Song. Europium-doped lead-free cs3bi2br9 perovskite quantum dots and ultrasensitive cu2+ detection. *ACS Sustainable Chem. Eng.*, 7:8397, 2019.

[121] J. Almutlaq, W. J. Mir, L. Guti©rrez-Arzaluz, J. Yin, S. Vasylevskyi, P. Maity, J. Liu, R. Naphade, O. F. Mohammed, and O. M. Bakr. Csmnbr3: Lead-free nanocrystals with high photoluminescence quantum yield and picosecond radiative lifetime. *ACS Mater. Lett.*, 3:290, 2021.

[122] L. Shao, D. Zhou, N. Ding, R. Sun, W. Xu, N. Wang, S. Xu, D. Liu, and H. Song. Broadband ultraviolet photodetectors based on cerium doped lead-free cs3mnbr5 metal halide nanocrystals. *ACS Sustainable Chem. Eng.*, 9:4980, 2021.

[123] Q. Kong, B. Yang, J. Chen, R. Zhang, S. Liu, D. Zheng, H. Zhang, Q. Liu, Y. Wang, and K. Han. Phase engineering of cesium manganese bromides nanocrystals with color-tunable emission. *Angew. Chem., Int. Ed.*, 133:19805, 2021.

[124] V. Morad, I. Cherniukh, L. Pttschacher, Y. Shynkarenko, S. Yakunin, and M. V. Kovalenko. Manganese (ii) in tetrahedral halide environment: factors governing bright green luminescence. *Chem. Mater.*, 31:10161, 2019.

[125] M. Imran, V. Caligiuri, M. Wang, L. Goldoni, M. Prato, R. Krahne, L. De Trizio, and L. Manna. Benzoyl halides as alternative precursors for the colloidal synthesis of lead-based halide perovskite nanocrystals. *J. Am. Chem. Soc.*, 140:2656, 2018.

[126] M. Imran, B. T. Mai, L. Goldoni, M. Cirignano, H. B. Jalali, F. Di Stasio, T. Pellegrino, and L. Manna. Switchable anion exchange in polymer-encapsulated apbx3 nanocrystals delivers stable all-perovskite white emitters. *ACS Energy Lett.*, 6:2844, 2021.

[127] M. De Franco, M. Cirignano, T. Cavattoni, H. B. Jalali, M. Prato, and F. Di Stasio. Facile purification protocol of cspbbr3 nanocrystals for light-emitting diodes with improved performance. *Opt. Mater.: X*, 13:100124, 2022.

[128] J. Goodyear and D. Kennedy. The crystal structure of csmnbr3. *Acta Crystallogr., Sect. B: Struct. Crystallogr. Cryst. Chem.*, 28:1640, 1972.

[129] D. Cox and F. Merkert. The preparation, crystal growth and perfection of double halides of csnicl3 type. *J. Cryst. Growth*, 13:282, 1972.

[130] M. Amit, A. Horowitz, E. Ron, and J. Makovsky. Preparation and crystal structures of some compounds of the a3 bx5 type (a= cs, tl, nh4, b= mn, fe, co, x= cl, br). *Isr. J. Chem.*, 11:749, 1973.

[131] U. Kambli and H. U. Guedel. Transfer of electronic excitation energy in the antiferromagnets rubidium trichloromanganate (ii), cesium trichloromanganate (ii), cesium tribromomanganate (ii), and rubidium tetrachloromanganate (ii). *Inorg. Chem.*, 23:3479, 1984.

[132] Y. Rodrguez-Lazcano, L. Nataf, and F. Rodrguez. Electronic structure and luminescence of [(ch3)4n]2mnx4(x = cl, br) crystals at high pressures by time-resolved spectroscopy: Pressure effects on the mn-mn exchange coupling. *Phys. Rev. B*, 80:085115, 2009.

[133] X. Bai, H. Zhong, B. Chen, C. Chen, J. Han, R. Zeng, and B. Zou. Pyridine-modulated mn ion emission properties of c10h12n2mnbr4 and c5h6nmnbr3 single crystals. *J. Phys. Chem. C*, 122:3130, 2018.

[134] J. Lin, Q. Zhang, L. Wang, X. Liu, W. Yan, T. Wu, X. Bu, and P. Feng. Atomically precise doping of monomanganese ion into coreless supertetrahedral chalcogenide nanocluster inducing unusual red shift in mn2+ emission. *J. Am. Chem. Soc.*, 136:4769, 2014.

[135] J. Orive, J. L. Mesa, R. Balda, J. n. Fern°ndez, J. s. Rodrguez Fern°ndez, T. Rojo, and M. a. I. Arriortua. Enhancement of the luminescent properties of a new red-emitting phosphor, mn2(hpo3)f2, by zn substitution. *Inorg. Chem.*, 50:12463, 2011.

[136] Y. Lv, Y. Jin, T. Sun, J. Su, C. Wang, G. Ju, L. Chen, and Y. Hu. Visible to nir down-shifting and nir to visible upconversion luminescence in ca14zn6ga10o35: Mn4+, ln3+ (ln = nd,yb,er). *Dyes Pigm*, 161:137, 2019.

[137] R. Valiente, O. Wenger, and H. U. Gºdel. New photon upconversion processes in yb3+ doped csmncl3 and rbmncl3. *Chem. Phys. Lett.*, 320:639, 2000.

[138] G. Pan, X. Bai, D. Yang, X. Chen, P. Jing, S. Qu, L. Zhang, D. Zhou, J. Zhu, and W. Xu. Doping lanthanide into perovskite nanocrystals: highly improved and expanded optical properties. *Nano lett*, 17:8005, 2017.

[139] T. J. Milstein, D. M. Kroupa, and D. R. Gamelin. Picosecond quantum cutting generates photoluminescence quantum yields over 100% in ytterbium-doped cspbcl3 nanocrystals. *Nano Lett.*, 18:3792, 2018.

[140] G. L. McPherson, Y. Y. Waguespack, T. C. Vanoy, and W. J. Rodriguez. Exciton migration in a ,Äò,Äòpseudo,Äô,Äô-one-dimensional crystal: Luminescence dynamics of doped csmnbr3. *J. Chem. Phys.*, 92:1768, 1990.

[141] V. Eremenko, V. Karachevtsev, V. Shapiro, and V. Slavin. Low-temperature

transport of magnetic excitons in the quasi-one-dimensional antiferromagnet csmncl3¬2h2o doped with cu2+ ions. *Phys. Rev. B*, 54:447, 1996.

[142] G. L. McPherson and A. Francis. Extensive energy transfer in a nearly one-dimensional crystal: The emisson spectrum of csmnbr3 doped with nd3+. *Phys. Rev. Lett.*, 41:1681, 1978.